# Ignition by Nanosecond Repetitively Pulsed Discharges

by

Raphael J. Dijoud

Submitted to the Department of Aeronautics and Astronautics
in partial fulfillment of the requirements for the degree of

Master of Science in Aeronautics and Astronautics

at the

MASSACHUSETTS INSTITUTE OF TECHNOLOGY

May 2023



Author .....
Department of Aeronautics and Astronautics
May 22, 2023

Certified by .....
Carmen Guerra-Garcia
Atlantic Richfield Career Development Professor in Energy Studies
Assistant Professor of Aeronautics and Astronautics
Thesis Supervisor

Accepted by .....
Jonathan P. How
R. C. Maclaurin Professor of Aeronautics and Astronautics
Chair, Graduate Program Committee

**Ignition by Nanosecond Repetitively Pulsed Discharges**

by

Raphael J. Dijoud

Submitted to the Department of Aeronautics and Astronautics
on May 22, 2023, in partial fulfillment of the
requirements for the degree of
Master of Science in Aeronautics and Astronautics

## Abstract

Previous works have shown that nanosecond pulsed plasmas can have strong benefits on ignition, including a reduction of ignition delay times, a decrease of minimum ignition energies, or an extension of lean ignition limits. These effects are highly dependent on experimental conditions such as temperature, mixture, pulse repetition frequency, pulse energy, or discharge size. Therefore, a model allowing for parametric explorations is needed to separate the influence of each variable on plasma-assisted ignition. This work presents the development of both (i) a zero-dimensional (0D) chemical model for plasma-assisted combustion relevant for aircraft engine applications, and (ii) a one-dimensional (1D) radial fluid model of reacting flows describing radial ignition triggered by Nanosecond Repetitively Pulsed discharges (NRP).

The models developed are used to explore the influence of various parameters in an optimization effort. Using the 0D model, the influence of initial gas temperature and energy deposited per pulse on the reduction of ignition delay time is analyzed. Various mixtures of fuel/oxygen/nitrogen are also explored, changing the equivalence ratio and dilution factor, and compared with an instantaneous pure thermal input from the discharge to quantify the chemical effect of the discharge. The 1D model is initially demonstrated in a scenario where no plasma is present, focusing on the ignition of a methane/air mixture by a high-temperature kernel. Additionally, a test case is presented, comparing different NRP ignition strategies. In this case, the total power budget of the discharge is maintained within a narrow range by adjusting the pulse repetition frequency inversely proportional to the square of the plasma region size. Different plasma kernel sizes and pulse repetition frequencies are explored, and their effect on ignition and flame propagation enhancement is discussed.

Thesis Supervisor: Carmen Guerra-Garcia
Title: Atlantic Richfield Career Development Professor in Energy Studies
Assistant Professor of Aeronautics and Astronautics

# Acknowledgments

I would like to express my heartfelt gratitude to several individuals and organizations who have played a significant role in supporting and contributing to my work.

First and foremost, I extend my deepest appreciation to my advisor, Carmen, for her unwavering support, invaluable guidance, and endless patience. Her insightful advice has been instrumental in shaping this research. I am truly grateful for her consistent understanding and encouragement throughout this journey.

I would also like to acknowledge the tremendous assistance provided by a group of dedicated undergraduate students: Nicholas Laws, Xavier Bell, Jose Betances, and Gabriella McDonald. Their contributions have been invaluable in advancing this work, and I am sincerely thankful for their involvement.

Furthermore, I am indebted to the Office of Naval Research (ONR), which generously sponsored this research through the Young Investigator Program under Award Number N00014-21-1-2571. The support of the ONR and the Jean Gaillard fellowship has been instrumental in enabling the progress of this study.

A special note of appreciation goes out to my labmates, who have made this research journey a truly enriching experience. Colin, thank you for your expertise and the time you dedicated to helping me. Lee, your calm presence has been a source of reassurance. Ben, your ambitious spirit has inspired me throughout. Lanie, thank you for your attentive listening and friendly demeanor. Sankarsh, your drive and enthusiasm have motivated me. I am also grateful to Todd, whose assistance has been invaluable during moments of despair.

I cannot express enough gratitude to my family—my parents and sisters—for their unwavering support and availability. Without them, I would not have come this far. I would also like to extend a big thanks to my friends from France, their friendship and encouragement have been a constant source of strength.

Finally, I would like to thank all my friends from MIT and beyond. To my dear friends from AeroAstro, the Triathlon and Rowing clubs, and my running, biking, and swimming buddies—Jackson, Jon, Valerie, Angela, and Alex—I am immensely grateful for your companionship and shared experiences. Dominic, thank you for helping me find clarity during the weekends. And to my roommate Mark, thank you for creating a sense of home here.

The contributions and support of all these individuals and organizations have played an integral part in the success of this work, and for that, I am truly thankful.

This master's thesis has been examined by a Committee of the
Department of Aeronautics and Astronautics as follows:

Professor Carmen Guerra-Garcia .....
Atlantic Richfield Career Development Professor in Energy Studies
Assistant Professor of Aeronautics and Astronautics
Thesis Supervisor

Jonathan P. How .....
R. C. Maclaurin Professor of Aeronautics and Astronautics
Chair, Graduate Program Committee

# Contents

# List of Figures

# List of Tables

# List of Equations

# Nomenclature

| | | |
|---|---|---|
| $\epsilon$ | energy | $J$ |
| $\epsilon_0$ | vacuum permittivity constant | $F.m^{-1}$ |
| $\Delta t_{IDT}$ | ignition delay time | $s$ |
| $\gamma$ | ratio of specific heats | n.u. |
| $\mathcal{E}$ | energy or volumetric energy | $J$ or $J.m^{-3}$ |
| $\mathcal{P}$ | power | $J.s^{-1}$ |
| $\rho$ | density | $kg.m^{-3}$ |
| $\lambda$ | thermal conductivity | $J.m^{-1}.K^{-1}.s^{-1}$ |
| $\lambda_D$ | Debye length | $m$ |
| $\mu_e$ | electron mobility | $m^2.V^{-1}.s^{-1}$ |
| $\nu$ | frequency | $s^{-1}$ |
| $\phi$ | equivalence ratio | n.u. |
| $\mathcal{N}_a$ | Avogadro constant | $mol^{-1}$ |
| $c$ | wave speed | $m.s^{-1}$ |
| $c_{p,k}$ | specific heat capacity at constant pressure of species $k$ | $J.K^{-1}.kg^{-1}$ |
| $c_{v,k}$ | specific heat capacity at constant volume of species $k$ | $J.K^{-1}.kg^{-1}$ |
| $D_k$ | diffusion coefficient of species $k$ | $m^2.s^{-1}$ |
| $e$ | specific internal energy or elementary charge | $J.kg^{-1}$ or $C$ |
| $E$ | electric field | $V.m^{-1}$ |
| $f$ | frequency | $s^{-1}$ |
| $h$ | specific enthalpy or height | $J.kg^{-1}$ or $m$ |
| $H_v$ | heat of combustion | $J.kg^{-1}$ |

| | | |
|---|---|---|
| $j_k$ | diffusion flux of species $k$ | $kg.m^{-2}.s^{-1}$ |
| $j$ | current density | $C.m^{-2}.s^{-1}$ |
| $k_B$ | Boltzmann constant | $m^2.kg.K^{-1}.s^{-2}$ |
| $m$ | mass | $kg$ |
| $M$ | molar mass | $kg.mol^{-1}$ |
| $n_k$ | species $k$ particles density | $m^{-3}$ |
| $N$ | total particles density | $m^{-3}$ |
| $p$ | pressure or momentum | $Pa$ or $kg.m.s^{-1}$ |
| $r$ | radius | $m$ |
| $r_p$ | plasma kernel radius | $m$ |
| $r_i$ | ignition kernel radius | $m$ |
| $R_g$ | specific gas constant | $J.K^{-1}.kg^{-1}$ |
| $R_r$ | reaction rate of reaction $r$ | $m^{-3}.s^{-1}$ |
| $R$ | ideal gas constant | $J.K^{-1}.mol^{-1}$ |
| $s_k$ | specific entropy of species $k$ | $J.K^{-1}.kg^{-1}$ |
| $t$ | time | $s$ |
| $T$ | gas temperature | $K$ |
| $T_e$ | electron temperature | $K$ |
| $u$ | velocity | $m.s^{-1}$ |
| $w$ | volumetric power | $J.m^{-3}.s^{-1}$ |
| $W$ | power or molecular weight | $J.s^{-1}$ or $kg$ |
| $X_k$ | mole fraction of species $k$ | n.u. |
| $Y_k$ | mass fraction of species $k$ | n.u. |

# Acronyms

| | |
|---|---|
| 0D | Zero-Dimensional |
| 1D | One-Dimensional |
| ASZ | Absorption Sponge Zone |
| FWHM | Full Width at Half-Maximum |
| IDT | Ignition Delay Time |
| LFA | Local Field Approximation |
| MIE | Minimum Ignition Energy |
| NRP | Nanosecond Repetitively Pulsed |
| ONR | Office of Naval Research |
| PAC | Plasma-Assisted Combustion |
| PAI | Plasma-Assisted Ignition |

# Chapter 1

# Introduction

## 1.1 Background on Plasma-Assisted Ignition

### 1.1.1 Brief History

Plasmas have always been used to help combustion processes. Automobiles use a thermal spark to ignite the fuel and initiate combustion since the 1910s. A thermal spark is a high-energy thermal plasma arc initiated by an externally-applied electric field. In such configurations, the plasma is only used as a thermal input (no significant kinetic effects). Thermal sparks have been studied for decades and their behavior in internal combustion engine environments is well documented [27].

The first reported exploration of plasma to enhance combustion through chemical effects took place in Oxford in 1904, by Haselfoot and Kirkby [26] (who were affiliated with Sir John Sealy Townsend, who left his name to the Townsend unit). They showed that electric discharges could be used to ignite hydrogen at low pressures, therefore extending the limits of ignition using plasma. In the 1960s, extensive work was conducted at Imperial College by Weinberg et al. to experimentally investigate the effects on combustion of "plasma jets" (i.e. plasma discharges), in an effort to enhance combustion [30, 15, 25].

Research efforts in plasma-assisted combustion really developed in the late 1990s and early 2000s, when experiments showed that plasma discharges could reduce flame instabilities and extend lean blowout limits, which is of great interest for industrial engines manufacturers. Today, the benefits of plasma assistance are largely documented, but quantitative predictions are challenging, especially because of the strong dependence on the specific conditions (discharge type, gas conditions).

### 1.1.2 Benefits of Plasma Assistance

#### Ignition Delay Time

The ignition delay time (IDT) is a widely used metric for ignition enhancement as it can be easily retrieved from zero-dimensional chemical kinetics models and can also be verified experimentally, usually using shock tubes. As soon as 2002, Bozhenkov et al. [10] proved both numerically and experimentally that, hydrogen and methane would ignite up to 3 times sooner when actuated by pulsed nanosecond discharges. Those results were obtained at high temperatures ($800 - 2000\ K$), but other works have experimentally proved similar benefits for propane at atmospheric temperature [52]. In a paper from 2008, Kosarev et al. [36] even showed that the ignition delay time of methane can be decreased by a factor 1000. These results are not limited to small hydrocarbons: Anikin et al. [5] presented in 2004 an experimental study revealing the efficiency of pulsed nanosecond discharges in quickly oxidizing larger alkanes, up to $C_6H_{14}$. Numerical work for larger hydrocarbons is more challenging but still exists. An article from 2009 [37] presented both experimental and numerical evidence that nanosecond discharges reduce the ignition delay time of various hydrocarbons ($C_nH_{2n+2}$ for $n = 2 - 5$). Overall, past experimental and numerical studies have shown that pulsed nanosecond discharges reduce ignition delay times (i) at both ambient and high temperatures, (ii) for pressures ranging from 0.4 to 2 $bars$, (iii) for all hydrocarbons tested. IDT reduction ranges from a factor 2 at worst but can reach up to a factor 1000. Experimental campaigns on real-sized engines also showed that pulsed nanosecond discharges reduce IDT for automotive gasoline [68] and pulse

detonation engines [40].

### Minimum Ignition Energy

The minimum ignition energy (MIE) is the minimum amount of energy needed to ignite a fuel/air mixture. Such values can be found tabulated for usual fuels when ignited by thermal sparks. In practice, this value depends on the gas conditions, but also on the way the energy is deposited (temporal and spatial dependence). In 2011, Tropina et al. [79] built a physical model of the effect of nanosecond repetitively pulsed (NRP) discharge on minimum ignition energy of stoichiometric methane and ethylene mixtures at ambient temperature and pressure. They noted a strong effect of the vibrational excitation of the gas and observed a decrease in MIE when they increased the pulse width. Experimental imaging and spectroscopy measurements by Singleton et al. [70] revealed an interesting case where multiple discharges lead to multiple points of ignition. Individual ignition kernels appeared where the generation of radicals by the discharge was the highest. Such findings suggest that plasma-enabled ignition could allow for more uniform inflammation in certain electrode configurations.

### Lean Limits

Since the late 2000s, the use of plasma assistance to maintain combustion below the lean flammability limit has brought up tremendous attention. Lean combustion is favorable as the flame temperature is lower, and thus the emission of toxic compounds like $NO_x$ is reduced. Pilla's experiment in 2008 [59] was one of the first to shed light on the effects of plasma on lean combustion. He found out that, investing only 0.3% of the flame power in NRP discharges was enough to stabilize a propane/air flame below its lean blowout limit. Numerous studies further develop the understanding of the effect. The conclusions were extended to other fuels like methane and ethane [7], with confirmation regarding the low amount of energy needed for the discharge compared to the flame power [16]. Kinetic modeling of the effect [6] and optimization strategies [8] were also conducted during the following decade. Although promising extensions of the lean blowout limit have been achieved, the net reductions of $NO_x$ have yet to be

confirmed, as the plasma activates new chemical pathways of $NO_x$ production.

If stabilization of flames below the lean blowoff limit has been extensively studied, only a few works explored plasma assistance to ignite such mixtures. In 2015, high-speed imaging of the ignition of a lean methane/air mixture by NRP discharges revealed that it was more effective than traditional sparks [60]. This study revealed the "jetting" phenomenon, a fluid effect induced by the discharge that tends to generate a wrinkled flame kernel that drastically enhances the first instants of propagation. A few years later, experimental imaging of ignition of lean propane/air flame by NRP discharges revealed that this "jetting" effect was likely caused by the generation of highly reactive species by the plasma and the apparition of thermal instabilities [43].

#### High-Speed Flows

Nanosecond plasma discharges have also been found to help combustion in high-speed flows (supersonic engines for instance). Plasma has been shown to improve re-circulation and flame anchoring, without necessarily inducing drag as geometrical flame holder elements would. In 2010, Do et al. published several experimental results where NRP discharges allowed for the ignition of hydrogen and ethylene in supersonic flows [17, 18].

Other benefits of plasma are summarized in the topical reviews by Starikovskaia [72] (2006), Starikovskiy and Aleksandrov [74] (2013), and Ju and Sun [33] (2015).

### 1.1.3 Efforts on Chemical Kinetics Tools and Mechanisms

In 2014, Starikovskaia wrote a topical review of the modeling efforts in the plasma-assisted combustion community [73]. Zero-dimensional models (chemical kinetics) are the most widely studied because they are convenient to handle, and can give insight into processes that happen during short timescales where higher dimensional effects can be neglected. Reaction rates are often validated against shock tube experiments, which provide uniform and repeatable conditions.

As its name suggests, the modeling of the chemistry of plasma-assisted combustion relies on the coupling of plasma and combustion chemistry. Because of its large industrial applications, combustion chemistry has been relatively well studied, at least for small fuels. The most widely used mechanism is the GRI [71], which focuses on methane combustion at high temperatures. Other combustion chemical kinetics models have been developed to better describe specific applications: HP-Mech [85, 66], USC Mech [82], Konnov mechanism, LLNL [2], UCSD [1]...

The plasma chemical models are much more diverse as they can focus on a wide range of mixtures. The most widely used plasma mechanism for air has been developed in 1992 by Kossyi et al. [38]. Since then, extensive work has been conducted to gain confidence in fuel/air mixtures, especially by Adamovich's group at Ohio State University. The importance of electronically excited states of nitrogen and oxygen has been demonstrated as they rapidly quench after the discharge and lead to the production of radicals that benefits the combustion, especially $O$ atoms. The rapid quenching of electronically excited states produced during the discharge can also lead to what has been referred to as "fast gas heating" by Popov in 2011 [62], when the energy stored in the excited state is released as thermal energy in nanosecond timescales.

The fundamental difference between combustion and plasma chemistry is that the key reactions that happen during the pulse time are triggered by collisions between heavy particles and free electrons that have been accelerated by the electric field. Those reaction rates depend on the electric temperature, rather than the much lower temperature of the background gas, and need to be computed using collisional cross-section tables that give the collision rate for a specific reaction. A typical approximation used is the Local Field Approximation (LFA) where the dependency with electron temperature is directly described by the reduced electric field, or $E/N$. Most of these tables can be found online, for instance in the LXCat database since 2012 [50]. The building of those tables began in the early 2000s, and is ideally validated against

swarm parameters [65, 47]. A review paper from Petrovic et al. in 2009 summarized the efforts in this area [57].

Cross-sections tables are then used with Boltzmann solvers, like BOLSIG+ [24], LOKI-B [76, 77], or BOLOS[1] [45]. Those Boltzmann solvers are incorporated in chemical kinetics solvers. Cantera [22] is an open-source tool widely used in the chemistry community that can model one-dimensional reacting flows. But the need to incorporate a Boltzmann solver into the plasma kinetics model forced the plasma community to develop its own tools. The chemical solver CHEMKIN was one of the first ones to incorporate plasma kinetics modeling in the mid 1990s [63]. Strongly based on this old chemical solver, ZDPlasKin [51] is today the most widely used plasma kinetics, open-source solver although multiple solvers exist.

### 1.1.4 Modeling in Higher Dimensions

Any simulation of plasma discharges in 1D (or higher dimensions) is challenging because it needs to couple the 0D detailed chemistry to 1D fluid effects. For that reason, many models were restrained to simplified plasma chemistry, and both temporal and spatial decoupling of plasma and combustion chemistry in order to keep the computational times low (for instance, considering the plasma as a source of radicals only). The most widely studied one-dimensional modeling of non-thermal plasmas remained the propagation of streamers ($ns$-timescale) [78]. Later work by Breden et al. looked at simulations of streamer propagations in fuel/air mixtures [11, 12]. Recently, Sharma at al. [67] developed a model of streamer propagation, flame ignition, and propagation by NRP discharge in a hydrogen/air mixture at high pressure. The influence of plasma gas temperature, radicals seeding, and generation of excited species was also studied.

[1] https://bolos.readthedocs.io/en/latest/index.html

## 1.2 General Concepts in Combustion

### 1.2.1 Equivalence Ratio

The equivalence ratio $\phi$ is a dimensionless parameter that represents the mixing ratio of fuel and oxidizer compared to stoichiometric conditions. Stoichiometric conditions yield $\phi = 1$, whereas $\phi < 1$ represents "lean" conditions (i.e. more oxidizer than what is needed to burn the fuel) and $\phi > 1$ "rich" conditions (i.e. more fuel than what can be burnt by the oxidizer). It can be expressed using either the mole fractions $X$ or the mass fractions $Y$ as:

$$\phi = \frac{\left(\frac{X_f}{X_{ox}}\right)}{\left(\frac{X_f}{X_{ox}}\right)_{st.}} = \frac{\left(\frac{Y_f}{Y_{ox}}\right)}{\left(\frac{Y_f}{Y_{ox}}\right)_{st.}} \tag{1.1}$$

For instance, the ratio of fuel to oxidizer mole fractions in stoichiometric conditions $(X_f/X_{ox})_{st.}$ can be retrieved by writing out the reaction balance:

$$CH_4 + 2O_2 \longrightarrow CO_2 + 2H_2O \tag{1.2}$$

The equivalence ratio for methane/air mixtures is shown in figure 1-1-a. The definition of equivalence ratio remains valid for mixtures of fuels. For example, if we define $F = 0.64C_2H_4 + 0.36CH_4$ (in moles), we can write down the following reaction balance of combustion of the fuel $F$:

$$F + 2.64O_2 \longrightarrow 1.64CO_2 + 2H_2O \tag{1.3}$$

When mixed with air, this leads to the equivalence ratio evolution plotted in figure 1-1-b.

### 1.2.2 Adiabatic Flame Temperature

The combustion of any fuel converts chemical energy (potential energy stored in chemical bonds) into thermal energy. The energy released during the combustion

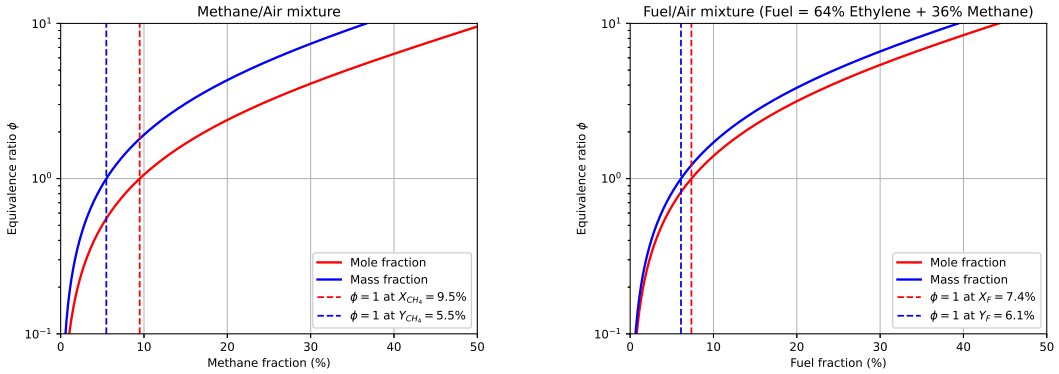


(a) Methane (b) 64% Ethylene + 36% Methane

Figure 1-1: Equivalence ratio as a function of fuel fraction in fuel/air mixtures.

of 1 $kg$ of fuel is usually referred to as heat of combustion or heating value. Such values can be found tabulated in some textbooks [41] and can be used to compute the temperature rise caused by ignition:

$$\Delta T = \frac{H_v}{c_p} Y_{f,burned} \tag{1.4}$$

Where $H_v$ refers to the heat of combustion[2] and the mass fraction of fuel burned $Y_{f,burned}$ depends on the burning conditions (lean or rich):

$$Y_{f,burned} = \begin{cases} Y_f & \text{if } \phi \leq 1 \\ Y_{ox} \left( \frac{Y_f}{Y_{ox}} \right)_{st.} & \text{if } \phi > 1 \end{cases} \tag{1.5}$$

### 1.2.3 Ignition Delay Time

The ignition delay time (IDT) is the time it takes for a given mixture to ignite. A mixture will ignite only if the conditions allow it, including (i) the equivalence ratio is within the ignition range and (ii) the temperature is above the auto-ignition temperature. At a given pressure and equivalence ratio, the auto-ignition temperature is a theoretical threshold temperature above which the ignition delay time is finite.

[2]It is important to note that the heating value $H_v$ depends on the temperature and physical state of the fuel before combustion.

If the conditions are met and ignition does occur, the ignition delay time can be determined as the instant when the temperature gradient is the sharpest:

$$\Delta t_{IDT} = \text{argmax}_t \ \frac{\partial T}{\partial t}(t) \tag{1.6}$$

This method works well in traditional combustion reactors, but adding plasma might need to add some filtering on the temperature profile in order to remove spikes in temperature rise originating from the discharges.

## 1.3 General Concepts in Plasma Discharges

### 1.3.1 Definition of Plasma

#### Ionized Gas

A plasma is a gas where a significant amount of free electrons and ions exist. Free electrons are usually produced by ionizations of "heavy particles" (i.e. atoms and molecules) which become ions. The ionization fraction $\alpha$ describes the proportion of electrons in a gaseous mixture, and the fraction of positive charge carriers (ions) is approximately the same:

$$\alpha = \frac{n_e}{N} \tag{1.7}$$

Air in atmospheric conditions typically has a free electron density of $10^2 - 10^3\ cm^{-3}$, i.e. an ionization fraction $\alpha \sim 10^{-16}$. This ionization fraction is very low as free electrons quickly recombine with ions. Complete or full ionization refers to conditions where $\alpha = 1$. Flames are sometimes referred to as plasma, as they can sometimes maintain a significant ionization fraction (depending on fuel, conditions, etc). Works have reported that free electrons in flames can vary from densities up to $10^{10}\ cm^{-3}$ [48] or even $10^{16}\ cm^{-3}$ [33]. But not all ionized gases are plasmas. Indeed, ionization fraction or electron density alone is not enough to qualify a mixture as plasma.

**Debye Length**

What makes plasma different from a simple gas is that the presence of charged particles induces "collective effects", especially in the presence of an electric field. For instance, a particular aspect of plasmas is that they spontaneously shield any electric field and that their bulk remains "quasi-neutral". The distance an externally-applied electric field can penetrate into a collection of charged particles is called the Debye length, which can be expressed as[3]:

$$\lambda_D = \sqrt{\frac{\epsilon_0 k_B T_e}{n_e e^2}} \tag{1.8}$$

The Debye length is a good estimation of the scale at which plasma effects come into play. For that reason, the Debye length is often used in the definition of plasma: the characteristic length scale of the plasma needs to be much larger than the Debye length.

### 1.3.2 Non-Thermal Plasma

Non-thermal or non-equilibrium plasma is a type of plasma where the free electrons and the other particles (called "heavy" particles) are not in thermal equilibrium. This non-equilibrium case means that the ionized mixture is described by the temperature of the heavy species $T$ (often called "gas temperature"), but also by the temperature of the electrons $T_e$. Non-thermal plasmas also present chemical nonequilibrium, and the energy distribution functions outside of equilibrium (non-Maxwellian), particularly the electrons.

For non-ionized gases, the gas remains in thermal equilibrium as collisions between particles homogenize the translational energies of the heavy particles. In a plasma, if the heavy particles often remain in thermal equilibrium, elastic collisions between an electron and a heavy particle will not necessarily lead to a homogenization of their

[3]The formula given for the Debye length is valid for quasi-neutral, "cold" plasma where the contribution of ions to shielding is neglected.

temperature. Because electrons are so much lighter than other particles in the gas, they can have a homogeneous electron temperature by equilibrating through elastic electron-electron collisions, but this temperature can be significantly different (usually larger) than the gas temperature.

A gas can be turned into a non-thermal plasma when it is under the application of a high electric field of short duration. If the electric field is high enough (depending on the gas and conditions), free electrons naturally present in the gas will be accelerated enough to cause ionizations by colliding with heavy particles, leading to even more electrons (electron avalanche). This cascade of ionizations will drastically increase the electron density $n_e$, thus reducing the Debye length. Eventually, the externally-applied electric field will be shielded by a large amount of charged particles, preventing further ionizations. By keeping the duration of the electric field short, on the order of nanoseconds, the non-thermal nature of the discharge is maintained.

Earliest studies of plasmas have found that the reduced electric field $E/N$ is a more relevant metric to quantify the electric field as seen by the gas. It is often expressed in Townsend ($1\ Td = 10^{-17}\ V \cdot cm^2$).

### 1.3.3 Thermal and Kinetic Effects

The presence of free electrons in a plasma lead to the emergence of new chemical reactions. As seen earlier, electrons accelerated by the electric field can lead to ionizations. But depending on the mixture and the electric field, part of the energy retrieved from the field will also lead to excitations (rotational, vibrational, electronic) or dissociations (for molecules). Eventually, the energy communicated from the electric field to the gas by the intermediary of the electrons can be divided into parts: (i) thermal energy and (ii) chemical energy.

The thermal energy part is all the part of the energy inputted which, at a given instant, has been transformed into a rise of the temperature of the mixture. Al-

though very inefficient (but occasionally observed, like in thermal sparks [46]), the temperature rise of the heavy species can be originated from direct elastic collisions with electrons. A more common pathway to release thermal energy is the natural quenching of excited states after the electron-impact excitation reactions during the application of the high voltage. Energetic excited states quench very fast ("fast gas heating" [62], with timescales of nanoseconds), while others like vibrational excitation take longer (micro-seconds).

Part of the inputted energy can also lead to an increase in the chemical energy of the gas, either: (i) by storing energy in excited states or (ii) by dissociating stable molecules. For instance, accelerated electrons colliding with an oxygen molecule ($O_2$) can lead to an electronic excitation, which will quickly undergo a dissociative quenching, leading to the generation of two oxygen radicals ($O$, possibly excited). Chemical effects are often more desired as they can improve the combustion process in a way pure thermal input cannot [39]. Some plasma-enabled chemical pathways have been proven to be highly beneficial for combustion efficiency (like $O$-radical seeding), as it allows the bypass of otherwise slow and energy-consuming chain initiation reactions.

## 1.4 This Work

### 1.4.1 Motivation

Nanosecond repetitively pulsed plasma discharges have been shown to have tremendous benefits on ignition. Past experiments, some backed by 0D numerical simulations, found important reductions in ignition delay time and minimum ignition energy, as well as an extension of ignition limits for a wide range of fuels and conditions. High-speed imaging of the ignition phase has shown peculiar fluid behaviors ("jetting" phenomenon) that are triggered by pulsed plasma discharges and are key to explaining how the plasma improves ignition.

Understanding the phenomenon of *inflammation*, i.e. the creation of the ignition kernel and emergence of a propagating flame front, is challenging as it needs modeling of plasma-combustion kinetics in at least one spatial dimension. Previous modeling of NRP discharges in high dimensions (1D and above) often focuses on the streamer propagation phase and does not deal with ignition kernel development. Models describing inflammation by NRP discharges and including detailed plasma and combustion chemistry are scarce and often need extensive computational resources.

To formulate a coherent understanding of the inflammation phase, we need to be able to build a numerical model that allows for parametric sweeping in order to decouple the influence of the multiple variables at play (temperature, mixture, pulse energy, actuation frequency, discharge geometry, etc). This thesis develops a model that accommodates three different timescales, while not being highly resource-consuming: (i) the plasma discharge timescale (sub-$ns$), (ii) the combustion timescale (sub-$\mu s$), and (iii) the fluid mechanics timescale (sub-$ms$). It can assimilate arbitrarily complex combustion and plasma chemistry in a one-dimensional fluid code depicting radial ignition. The effects of plasma on combustion metrics such as flame speed, ignition kernel size, or minimum ignition energy can then be studied.

### 1.4.2 Outline

In chapter 2, we describe thoroughly the models that have been developed for this work. We start with the development of a zero-dimensional model coupling combustion and plasma chemical kinetics (see section 2.1). We also gather combustion and plasma kinetics relevant to aircraft applications (especially afterburners) through the selection of a surrogate fuel (see section 2.3). The 0D code is incorporated in a one-dimensional radial solver to study the radial ignition and flame propagation mechanisms arising from a plasma discharge. The fluid equations used and numerical implementations are summarized in section 2.4.

Chapter 3 gathers the analysis of the various results obtained. We first study the predictions from the 0D code with the kinetics mechanism developed in this work and compare it to results found in the literature (see section 3.1). We then run parametric sweeps to understand the effect of temperature and pulse energy on ignition delay time (see section 3.2). We also present in a ternary plot format the effect of equivalence ratio and dilution on ignition compared to pure thermal input from the discharges (see section 3.3). We then move to results from the 1D model. Section 3.4 presents a baseline 1D result without plasma, where ignition is triggered by a high-temperature kernel. This test case is then compared with cases where ignition is initiated by NRP discharges applied in a region close to the center (see section 3.5). Two cases are compared: (i) a large plasma kernel actuated at low frequency (section 3.5.2) and (ii) a small plasma kernel actuated at high frequency (section 3.5.3). The influence of plasma kernel size and pulse repetition frequency on ignition and flame propagation is discussed in section 3.6.

Finally, chapter 4 summarizes the contributions presented in this work. The main observations regarding the optimization of ignition by NRP discharges are gathered. Limits and recommendations for future work are discussed.

# Chapter 2

# Numerical Model for Plasma-Assisted Ignition

This chapter describes the zero-dimensional model combining combustion and plasma chemistry developed as part of this thesis. Plasma and combustion chemical kinetics are selected for conditions relevant to aircraft engine applications. The 0D code is then incorporated in a one-dimensional fluid solver in radial coordinates to incorporate transport effects in the ignition assessment. The focus of the model is to have a good physical representation (including complex chemistry, transport, and pressure wave generation) and numerical efficiency (to allow for parametrically sweeping a large parameter space).

## 2.1 Zero-Dimensional Combustion and Plasma Kinetics Solver

### 2.1.1 Code Structure

The code developed combines two open-source zero-dimensional chemical kinetics solvers into one unified structure. The first code is ZDPlasKin [51], a plasma kinetics solver that uses BOLSIG+ [24] to solve for the electron distribution function. The second is Cantera [22], a broad chemical solver that can be used for combustion.

### BOLSIG+

BOLSIG+ is a numerical solver of the Boltzmann equation (BE) developed in the mid-2000s at the Laplace laboratory, France [24]. BOLSIG+ solves the Boltzmann equation for electrons in order to compute the energy distribution function, and deduce the collision rates with the heavy particles.

$$\frac{\partial f}{\partial t} + \frac{\vec{p}}{m_e} \cdot \nabla f + \vec{F} \cdot \frac{\partial f}{\partial \vec{p}} = \left( \frac{\partial f}{\partial t} \right)_{coll} \tag{2.1}$$

Where $\vec{F}$ is the force field acting on electrons (electric force) and $\vec{p} = m_e \vec{v}$ is the momentum.

### ZDPlasKin

ZDPlasKin (Zero-Dimensional PLASma KINetics) is a zero-dimensional chemical kinetics solver developed a few years after BOLSIG+, by the same group. The solver [51] allows to solve for low temperature plasma chemistry, with electron energy distribution functions that diverge from the Maxwellian solution, by solving for the Boltzmann Equation along with the species continuity equations. It allows to independently track the electron and bulk gas translational temperatures. More precisely, it uses BOLSIG+ to predict the collision rates and other thermodynamic properties that involve electrons, and use it to solve for a chemical kinetics mechanism. The system of equations solved by ZDPlasKin is the following:

$$\forall k, \frac{dn_k}{dt} = -\sum_r a_{r,k} R_r \tag{2.2}$$

$$\frac{n_g}{\gamma - 1} \frac{dT_g}{dt} = \sum_r \epsilon_r R_r + n_e \mathcal{P}_{elast} \tag{2.3}$$

Where $R_r$ refers to the reaction rate of reaction $r$. It can be inputted directly by the user (as an Arrhenius rate for example), or be retrieved from BOLSIG+ computations for electron collisions. $\mathcal{P}_{elast}$ is the power coming from electron-neutral

elastic collisions. Each reaction balance is inputted by the user as:

$$\forall r, \sum_k a_{r,k} S_k - \epsilon_r = 0 \tag{2.4}$$

Where $S_k$ refers to the name of species $k$. For instance, a charge-exchange reaction between $N_2^+$ and $O_2$ would be:

$$1 \times N_2^+ + 1 \times O_2 + (-1) \times O_2^+ + (-1) \times N_2 - (3.54eV) = 0$$

The energy released $\epsilon_r$ (see equation 2.4) is not accounted for if the gas heating equation (equation 2.3) is not activated. Otherwise, it must be manually inputted by the user[1].

#### Cantera

Cantera [23] is a code that offers an intuitive thermo-chemical structure to study chemical kinetics and reacting flows that are mostly described by a single temperature and Arrhenius type reactions. It can be used to model one-dimensional reacting flows like flames, but also for zero-dimensional kinetic studies. The model uses thermodynamic data files and chemical kinetic mechanisms (such as GRI 3.0 [71] for combustion) to solve in a versatile environment with multiple options regarding assumptions and initial conditions. In our work, Cantera has been mainly used to benefit from the thermodynamic data files and structure, and to solve for combustion reaction mechanisms.

### 2.1.2 Validation

We used a test case to validate the code, with and without plasma. The test cases have been taken from the literature, from the work from Kosarev et al. [36] published in *Combustion and Flame* in 2008. They proposed a simple plasma mechanism (only

[1]However, in the case of electron collisions reactions, the energy released $\epsilon_r$ (see equation 2.4) is already accounted for by BOLSIG+. Generally, the term $\epsilon_r$ must be specified only if the energy released/consumed goes to/comes from the gas temperature.

22 reactions) to describe the combustion of methane in argon-diluted mixtures ([36] table 2). They also used the GRI 3.0 mechanism [71] for the combustion. The gas is initially composed of stoichiometric methane-oxygen diluted at 90% in argon (in moles). The initial conditions are at 1450 $K$ and 1.2 $bars$, with $10^3$ $cm^{-3}$ as an initial electron density. The pulse shape has been digitalized from the article ([36] fig.3a) and extrapolated up to 440 $Td$ at $t = 0$. Results are shown on figures 2-1 (comparison of species during the pulse), 2-2 (comparison for autoignition), and 2-3 (comparison for ignition after a single discharge).

Overall, we can note a very good agreement between the results from the literature and the predictions from our code. The auto-ignition case (see figure 2-2) presents an excellent agreement as only the combustion code is used (no plasma), which is entirely dealt with through the Cantera framework [22]. The cases with plasma (see figures 2-1 and 2-3) show overall good agreement but small differences can be observed. For instance, the recombination rate of ions and electrons is slightly smaller in our predictions (see figure 2-1.a-b). Differences can also be observed in the reaction rates regarding excitation (especially $Ar$ and $O_2$ excitations, see figures 2-1e-f). This could explain part of the discrepancies that we observe at the combustion timescale ($\sim$ 1 $ms$) in the case where a single pulse is applied. Indeed, our work predicts an ignition delay time around 10 times larger than what is presented in Kosarev's paper [36] (see figure 2-3), increasing from 200 $\mu s$ up to 2 $ms$. Large differences can also be seen in both mole fractions and reaction rates (see figures 2-3.a-d). But these differences originate only from the pulse computations, as the auto-ignition case has revealed that the combustion alone matches perfectly the results from Kosarev's paper (see figure 2-2). It can be deduced that the small differences we observe during the pulse timescale ( see figure 2-1) lead to visible consequences on the combustion timescale (such as on ignition delay time). Since the reaction rates and mole fractions of the plasma species are largely dependent on the pulse shape and amplitude, as well as the collision cross sections used, the differences observed between our model and the literature validation case likely come from those sources. E.g., the pulse had to

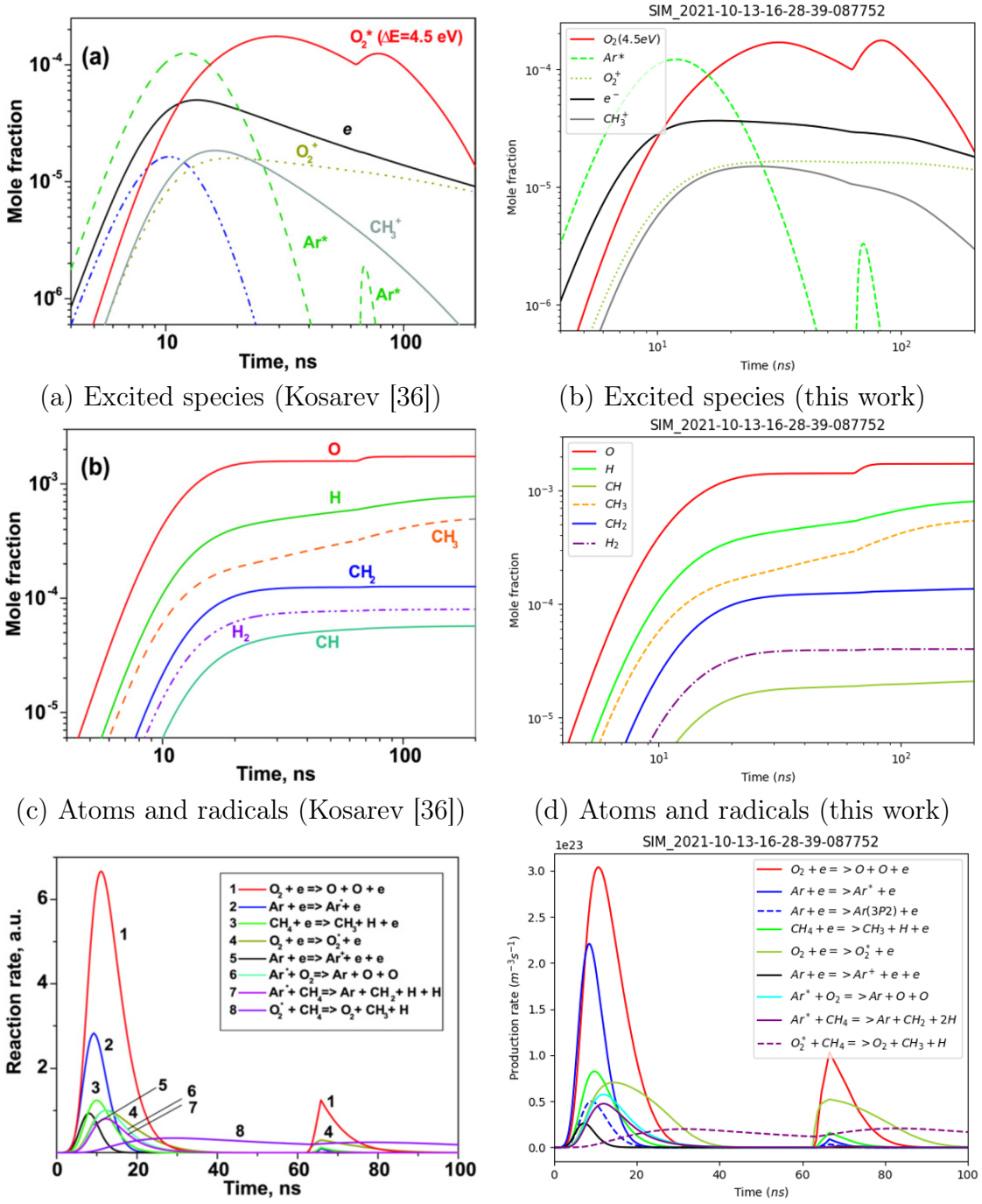


(a) Excited species (Kosarev [36])

(b) Excited species (this work)

(c) Atoms and radicals (Kosarev [36])

(d) Atoms and radicals (this work)

(e) Reaction rates (Kosarev [36])

(f) Reaction rates (this work)

Figure 2-1: Comparison of the 0D code with a test case from the literature: timescale of the pulse.

be re-created from a figure that did not report the initial value, and so extrapolation to 440 $Td$ was used.

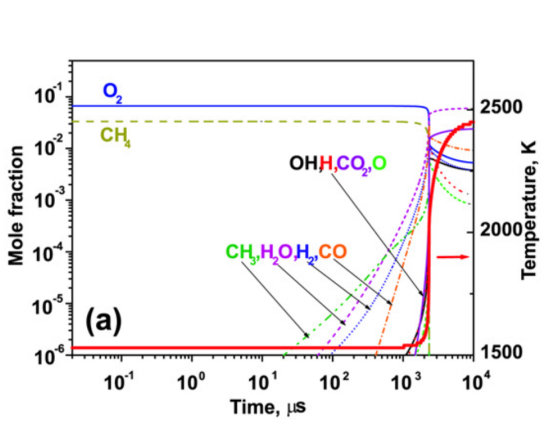


(a) Main species (Kosarev [36])

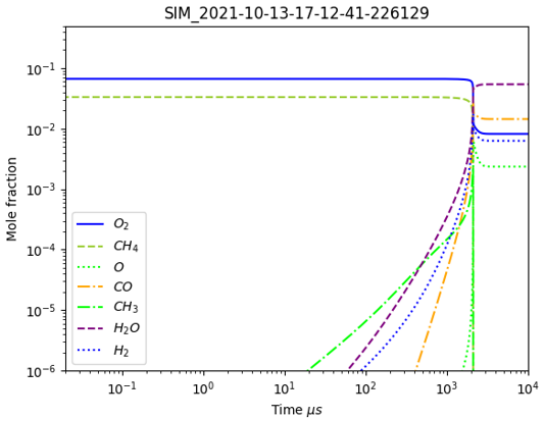


(b) Main species (this work)

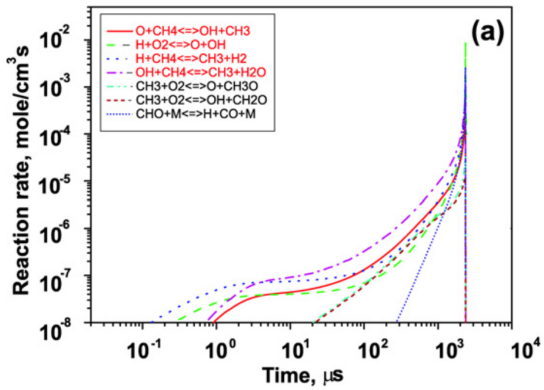


(c) Reaction rates (Kosarev [36])

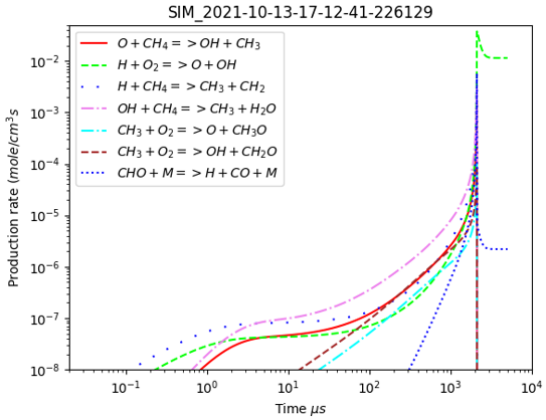


(d) Reaction rates (this work)

Figure 2-2: Comparison of the 0D code with a test case from the literature: auto-ignition.

In conclusion, our code shows good agreement with the predictions from Kosarev et al. [36] during the pulse, and for auto-ignition. Small differences in recombination rates were observed during the pulse's timescale which have a significant influence on overall ignition delay time.

## 2.2 Energy Considerations

The energy deposited by a single pulse can be directly linked with the current density and electric field as:

$$\mathcal{E}_{pulse} = \int \vec{j} \cdot \vec{E} dt = e \int \mu_e n_e E^2 dt = e \int \mu_e n_e N^2 \left(\frac{E}{N}\right)^2 dt \tag{2.5}$$

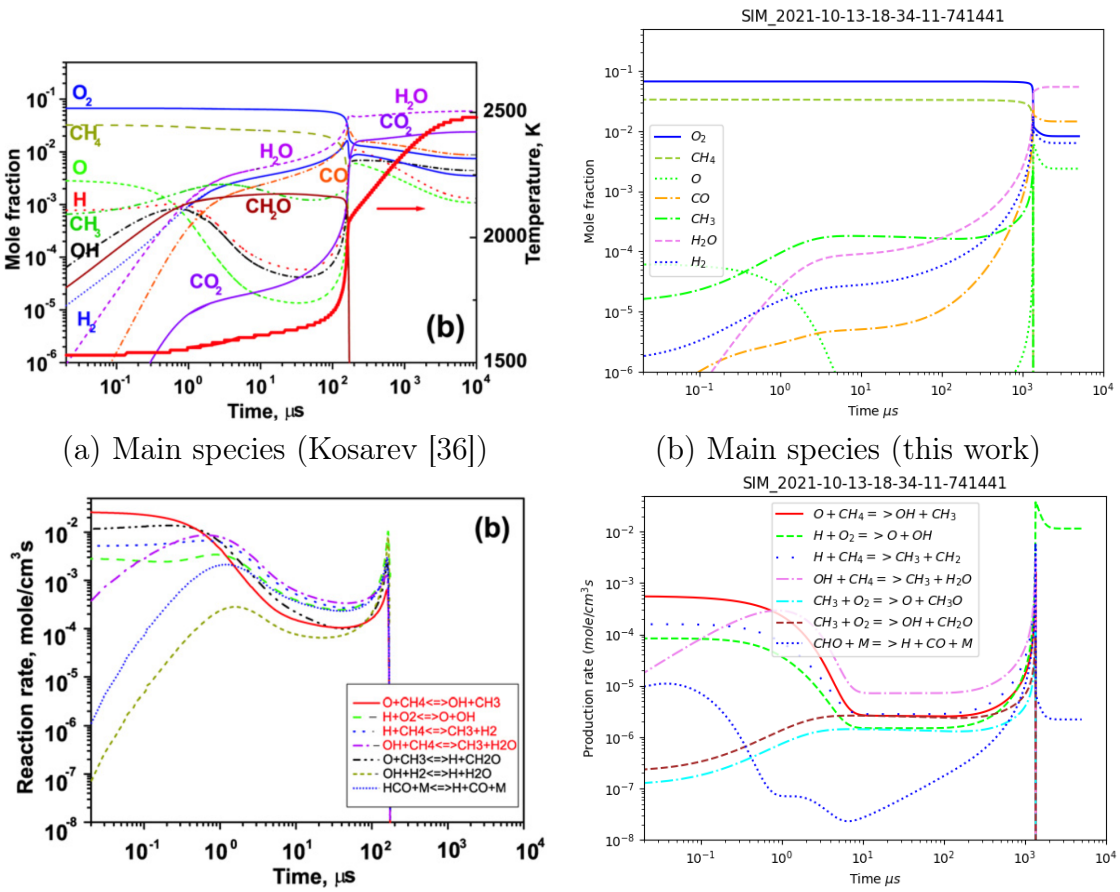


(a) Main species (Kosarev [36])

(b) Main species (this work)

(c) Reaction rates (Kosarev [36])

(d) Reaction rates (this work)

Figure 2-3: Comparison of the 0D code with a test case from the literature: ignition by a single discharge.

Where only the electrons are assumed to contribute to the current, and where $\mu_e$ refers to the electron mobility ($\vec{u}_e = \mu_e \vec{E}$). In general, the pulse applied (i.e. the $\left(\frac{E}{N}\right)(t)$ function) is either Gaussian in shape or comes from experimental measurements. This leads to an energy deposited per pulse $\mathcal{E}_{pulse}$ that can evolve on a wide range depending on the mixture, frequency, etc. Indeed, the energy deposited per pulse $\mathcal{E}_{pulse}$ depends primarily on the electron density $n_e$, which in turn depends on the mixture, the pulse repetition frequency, and the area under the curve of the reduced electric field. We can make the approximation:

$$\mathcal{E}_{pulse} \approx e\left(\bar{\mu}_e \bar{N}\right) \bar{N} \int n_e \left(\frac{E}{N}\right)^2 dt \tag{2.6}$$

The term $\mu_e N$ depends only on the reduced electric field. Since the pulse shape is usually fixed, the variation in electron mobility is second order compared to direct dependencies with $(E/N)^2$. The total density $N$ also changes only slightly during the pulse, as it is not affected by ionization. However, the electron density $n_e$ can take values anywhere from $10^3\ cm^{-3}$ at rest, up to $10^{19}\ cm^{-3}$ at full ionization, so it has a huge impact on the energy deposited. The averaged value of the electron density during the pulse $\bar{n}_e$ can be a good approximation as the electron density evolves monotonically during the pulse, on a range much smaller (but still can reach a few orders of magnitude).

We want to have better control over the energy deposited per pulse $\mathcal{E}_{pulse}$, especially to limit it as simulations have shown that it can sometimes reach very large, unrealistic values. These challenges arise as we will use the model to sweep a large parameter space and are using fixed $E/N(t)$ waveforms. These phenomena occur close to full ionization conditions (the electron density is very large). In reality, a large electron density will lead to a decrease in the reduced electric field through shielding effects. This will in turn reduce the ionization rate, lead to a decrease in electron density, and hence create a self-limiting process of what energy a pulse can deposit. This shielding effect is incorporated as a corrected reduced electric field $\left(\frac{\tilde{E}}{N}\right)$:

$$\left(\frac{\tilde{E}}{N}\right) = \left(\frac{E}{N}\right)\left(1 - \frac{n_e}{n_{e,shielding}}\right) \tag{2.7}$$

Where $n_{e,shielding}$ refers to the electron density that leads to a complete shielding of the electric field. We used another method, more direct, where the reduced electric field is cut off down to $0\ Td$ when the electron density reaches a threshold value (about $n_{e,threshold} = 10^{15}\ cm^{-3}$). For the case of a square waveform, the energy per pulse would then be:

$$\mathcal{E}_{pulse} \approx e\bar{\mu}_e \bar{N}^2 \bar{n}_e \left(\frac{E}{N}\right)^2_{max} \Delta t \tag{2.8}$$

## 2.3 Surrogate Fuel

### 2.3.1 Motivation

The fuel typically used in aircraft technology is kerosene, a liquid compound composed of various hydrocarbons. Kerosene includes alkanes whose chemical formulas range from $C_{10}H_{22}$ up to $C_{14}H_{30}$. During the combustion process, such hydrocarbons dissociate in many intermediate products including into smaller hydrocarbon chains. Consequently, any meaningful combustion mechanism for kerosene would need to include not only $C10 - C14$ hydrocarbons, but also all the relevant products, i.e. $C1 - C9$ chains. Tracking all these different species drastically increase the complexity of the model, as it increases the number of unknowns and the number of reactions scales exponentially.

To simplify the combustion kinetics, the combustion community usually limits the chemistry to simpler fuels, such as methane ($CH_4$) or propane ($C_3H_8$). In the plasma community, simplifying the chemistry to shorter compounds is even more needed. Indeed, plasma kinetics are more challenging to validate experimentally and most plasma-combustion works are limited to air (possibly with argon, nitrogen, or helium dilution) with fuels: hydrogen or methane. Higher-order hydrocarbons are not studied as dissociations and ionizations during the pulsing lead to a large number of species and the reaction rates for these mechanisms have not been validated.

The idea of a surrogate fuel is to use a different fuel in the development phase than what will be actually used in the industrial application. The goal is to make the numerical simulations manageable and physically trustworthy, without sacrificing too much in relevance regarding how the actual fuel will behave. To this end, the selected surrogate fuel must have similar combustion metrics as the actual fuel, including ignition delay time, auto-ignition temperature, lean and rich ignition and flammability limits, laminar flame speed, or reaction pathways. All or part of these metrics are looked at when selecting a surrogate fuel.

In their conference article from 2008, Pellett et al. [55] proposed a surrogate hydrocarbon fuel for scramjet fuel composed of 36% methane ($CH_4$) and 64% ethylene ($C_2H_4$). This mixture has been selected for our plasma and combustion studies.

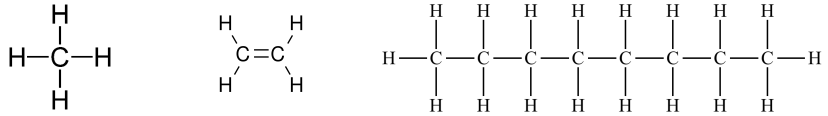

(a) Methane (b) Ethylene (c) Octane

Figure 2-4: Chemical formulas for (a) methane, (b) ethylene, and (c) octane.

### 2.3.2 Combustion Kinetics

As one of the simplest fuels, methane combustion mechanisms have been widely studied and verified against experimental data. However, combustion mechanisms are often validated for a specific range of gas pressures and temperatures, as well as limits in dilution and equivalence ratio. They are typically good to predict one or several specific global combustion parameters (e.g., flame speed, ignition delay time, etc). Multiple combustion mechanisms are listed in a paper by Simmie [69]. The main mechanisms used for methane combustion are summarized in table 2.1 (size of the mechanism refers to the number of species tracked in the chemical kinetics).

| Name | $T\ (K)$ | $p\ (atm)$ | $\phi$ | Size | Application focus | Ref. |
|---|---|---|---|---|---|---|
| GRI 3.0 | $1000-2500$ | $0.01-10$ | $0.1-5$ | 53 | Methane | [71] |
| HP-Mech | $<800$ | $1-20$ | $0.6-1.5$ | 93 | High-pressure | [14] |
| RAMEC | $1000-1500$ | $40-260$ | $<6$ | 38 | Methane | [56] |
| USC II | $1000-2500$ | $0.01-10$ | $0.1-5$ | 111 | $H_2/CO/C1-C3$ | [82] |

Table 2.1: Comparison of some combustion kinetic mechanisms used by the combustion community.

Because we are looking at conditions relevant to the afterburner environment (see table 2.2), we selected chemical mechanisms that describe combustion in atmospheric pressure, and high-temperature gas conditions. HP-mech [14] and RAMEC [56] are not selected for this reason. Note however that HP-Mech [14] is particularly interesting at low-temperature conditions and it is considered specially useful when consider-

ing low-temperature chemistry (of much interest for plasma-combustion applications in general).

| Inlet Condition | Main Combustor | Afterburner |
|---|---|---|
| Temperature ($K$) | $625 - 925$ | $925 - 1325$ |
| Pressure ($atm$) | $10 - 30$ | $0.5 - 6$ |
| Velocity ($m \cdot s^{-1}$) | $30 - 60$ | $150 - 250$ |
| Oxygen (% vol.) | 21 | $12 - 17$ |

Table 2.2: Flow conditions in combustion environments for relevant aircraft engines [44].

Secondly, the surrogate fuel is mainly composed of ethylene so we want a chemical mechanism that describes well ethylene combustion. Various kinetic mechanisms are compared in an article by Xu and Konnov [84] regarding ethylene combustion. The mechanisms studied are Konnov's mechanism [35], the USC Mech II [82], the LLNL mechanism [2], and the San Diego mechanism (UCSD) [1]. Several parameters including ignition delay time and laminar burning speed are looked at to determine which mechanism is the most accurate for ethylene combustion. In 0D simulations, the ignition delay time is an important parameter that can be easily retrieved. USC Mech II seems to be the most accurate at predicting ignition delay time for ethylene on a wide range of temperatures, for these reasons, USC Mech II has been selected for all simulations involving the combustion of the surrogate fuel.

### 2.3.3 Plasma Kinetics

The plasma kinetics must include the surrogate fuel (methane, ethylene), but also air species such as excited states of nitrogen ($N_2^*$). The methane part of the plasma mechanism was taken from the work of Aleksandrov et al. [3] (see appendix A). If there exists some plasma kinetics mechanisms describing methane, models describing ethylene are scarce even at atmospheric conditions. In a review paper on kinetic mechanisms by Starikovskaia [73], various kinetic mechanisms are presented depending on the experimental conditions used for their validation. We can notice that the

only experimental data involving ethylene as fuel in plasma-assisted combustion experiments is available at low pressure and somewhat low temperature (below 500 $K$). This does not perfectly match the conditions of interest for our studies relevant to aircraft combustion (see table 2.2). In 2013, Yin et al. compared performances of existing kinetic mechanisms (plasma and combustion) for different fuels including ethylene [86]. Other measurements of concentrations above a flat flame burner for ethylene stochiometric and lean conditions can be found in the literature [42], but without modeling. Ombrello et al. managed to measure quenching rates of excited oxygen with ethylene molecules [49], but no reactions involving electron collisions with ethylene or ethylene dissociation were recommended. Lefkowitz was the first one to develop in 2016 in his Ph.D. thesis a plasma mechanism for ethylene [32], including electron-collision dissociative rates for ethylene (see appendix A). Lacking experimental data, those rates were deduced from the work of Janev and Reiter in 2003 [31]. In their paper, a large amount of electron-collision cross-sections are presented for "large" hydrocarbon molecules (namely $C_{2,3}H_y$) based on experimental data and scaling relationships. The formulas to compute the cross-sections describing the inelastic collision rates (ionization and dissociation) of free electrons and ethylene molecules is given in Janev and Reiter page 796 [31]:

$$\sigma_{ion}(E) = 274.0 \cdot 10^{-20} \cdot \frac{1}{E}\left(1 - \frac{E_{th}}{E}\right)^3 \ln\left(e + 0.09E\right) \ [m^2] \tag{2.9}$$

$$\sigma_{diss}(E) = 71.2 \cdot 10^{-20} \cdot \frac{1}{E}\left(1 - \frac{E_{th}}{E}\right)^3 \ln\left(e + 0.15E\right) \ [m^2] \tag{2.10}$$

Where the energy threshold $E_{th}$ is given in Janev and Reiter pages 792 and 795 [31]. The resulting cross-sections for ethylene are given in figure 2-5 for different products, compared with $N_2$ and $CH_4$ electron-collision dissociation cross-sections.

Overall, figure 2-5 shows that both ionization and dissociation cross-sections are significantly higher for ethylene than other species in the model. The computed rates will likely lead to a greater influence of the plasma on ethylene combustion.

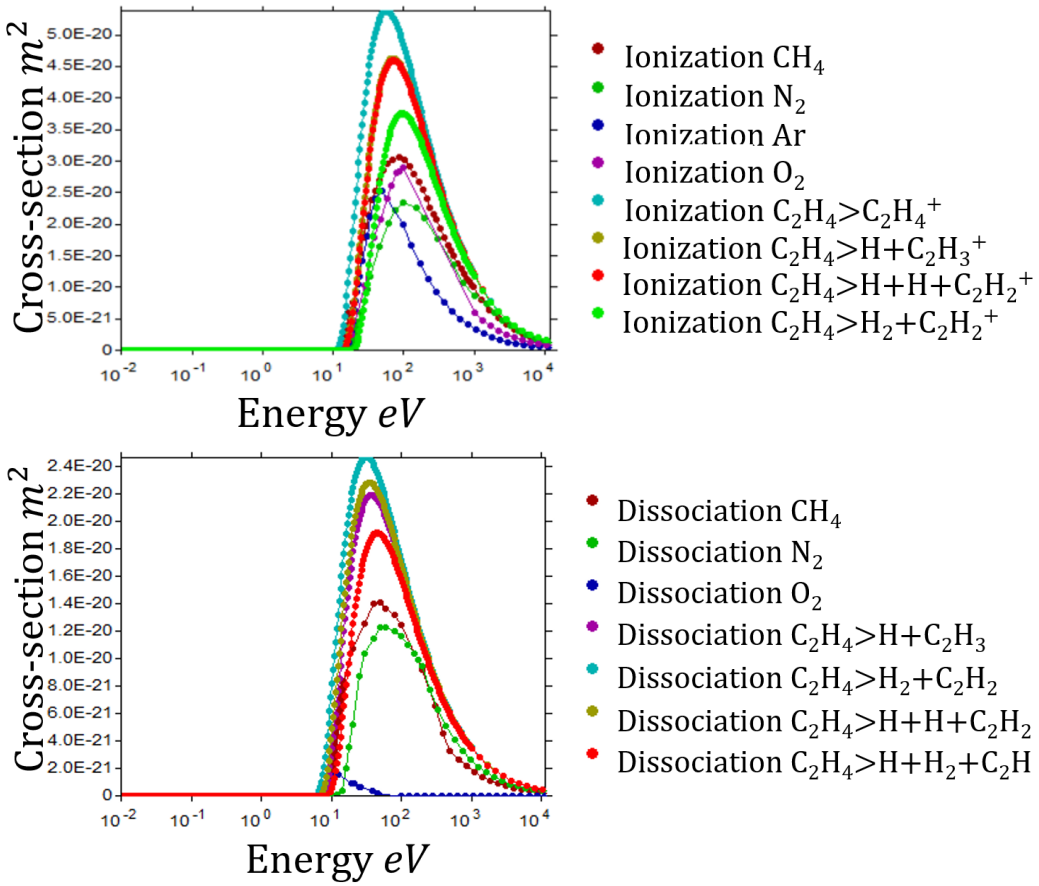


Figure 2-5: Comparison of electron-impact reaction cross-sections used in the plasma kinetics.

## 2.4 One-Dimensionsal Radial Fluid Model

### 2.4.1 Code Structure

The one-dimensional code combines the zero-dimensional chemical model (as described in section 2.1 into a one-dimensional grid. In addition to being affected by the local chemistry in a cell, the species can also be subjected to fluxes and move from one cell to the other, represented by a 1D fluid model with reacting flow, in cylindrical coordinates. A schematic of the overall code structure is given in figure 2-6. The focus of this thesis is the 1D inflammation by plasma micro-discharge submodel.

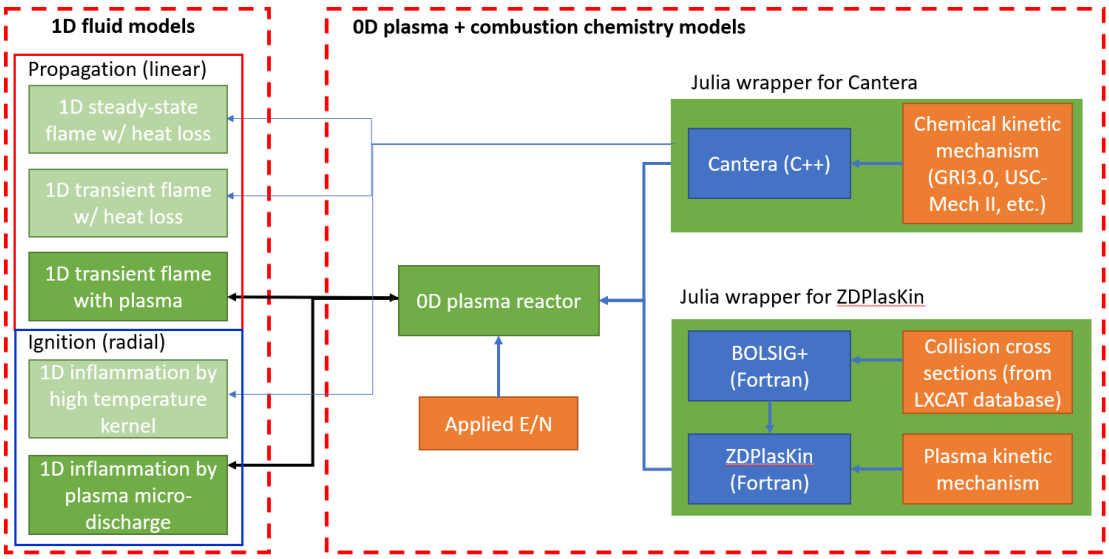


Figure 2-6: General structure of the 1D code with reacting flow and plasma chemistry.

### 2.4.2 Physical Quantities and Unknowns

The one-dimensional fluid-chemical model couples the zero-dimensional chemical solver described in the previous section with a one-dimensional fluid code. The fluid part solves a system of conservation equations at each timestep, to solve for the unknowns. In our case, the time and space-dependent unknowns we solve for are:

- the gas density $\rho$
- the gas radial velocity $u$
- for every species $k$, the mass fraction $Y_k$
- the internal energy $e$

From these physical quantities, all other quantities can be deduced. Some physical quantities are computed using the NASA-7 polynomials embedded in the Cantera code. For each species $k$, those polynomials approximate the molar heat capacity $\tilde{c}_{p,k}$, the molar enthalpy $\tilde{h}_k$, and the molar entropy $\tilde{s}_k$ thanks to 7 coefficients $\left(a_i^{(k)}\right)_{1\leq i\leq 7}$

that can be found in thermodynamic tables for a specific temperature range:

$$\begin{aligned}
\tilde{c}_{p,k} &= R\left(a_1^{(k)} + a_2^{(k)}T + a_3^{(k)}T^2 + a_4^{(k)}T^3 + a_5^{(k)}T^4\right) \\
\tilde{h}_k &= R\left(a_1^{(k)}T + \tfrac{a_2^{(k)}}{2}T^2 + \tfrac{a_3^{(k)}}{3}T^3 + \tfrac{a_4^{(k)}}{4}T^4 + \tfrac{a_5^{(k)}}{5}T^5 + a_6^{(k)}\right) \\
\tilde{s}_k &= R\left(a_1^{(k)}\ln T + a_2^{(k)}T + \tfrac{a_3^{(k)}}{2}T^2 + \tfrac{a_4^{(k)}}{3}T^3 + \tfrac{a_5^{(k)}}{4}T^4 + a_7^{(k)}\right)
\end{aligned} \tag{2.11}$$

Other approximations exist, such as NASA-9 (with 9 coefficients instead of 7), but have not been used in this work. The values of the coefficients $\left(a_i^{(k)}\right)_{1\leq i\leq 7}$ are usually given in the input files for combustion mechanisms (such as GRI3.0 [71] or USC Mech II [82]).

### 2.4.3 Conservation Equations

#### Conservation of Mass

The first conservation equation is used to determine the unknown density $\rho(r,t)$. In fluid mechanics, this law is also known as the continuity equation:

$$\frac{\partial \rho}{\partial t} = -\frac{1}{r}\frac{\partial\left(r\rho u\right)}{\partial r} \tag{2.12}$$

No approximations have been made to formulate this conservation equation (other than $u$ is much smaller than the speed of light), and it can be deduced from a simple mass balance on a single cell.

#### Conservation of Momentum

The equation for conservation of momentum is obtained neglecting viscosity ($\mu = 0$), and thus turbulence. In addition to the momentum flux term similar to the mass flux term in equation 2.12, the momentum conservation equation also incorporates the contribution from pressure gradients:

$$\frac{\partial(\rho u)}{\partial t} = -\frac{1}{r}\frac{\partial\left(r\rho u^2\right)}{\partial r} - \frac{\partial p}{\partial r} \tag{2.13}$$

We encountered numerical instabilities in the solving of this equation, caused by the pressure gradient term. Numerical corrections were needed to ensure proper convergence of the solution, using the work from Bartholomew et al. [9].

### Conservation of Species

The conservation of species is incorporated in our code since we track every species separately. Although all species are assumed to share the same $\rho$, $u$, and $T$ values, the local composition of the gas described by the mass fractions $Y_k(r,t)$ generally depends on both space and time. The resulting equation is similar to the continuity equation 2.12 in form, but includes two additional phenomena that intervene during the mass balance of species $k$, namely:

- the contribution from species diffusion. Gradients in the concentration of a species will lead to transport of that species in an effort to homogenize the mixture.

- the contribution from chemical reactions. A particular species may be consumed or generated from chemical reactions like dissociation or combustion.

The equation of conservation of species $k$ ends up taking the following form:

$$\frac{\partial(\rho Y_k)}{\partial t} = -\frac{1}{r}\frac{\partial\left(r\rho u Y_k + r j_k\right)}{\partial r} + \sum_i \dot{\omega}_{i,k} \tag{2.14}$$

Where $j_k$ is the diffusion flux of species $k$ (positive if species $k$ diffuses radially out), and $\dot{\omega}_{i,k}$ is the production rate of species $k$ though reaction $i$ (can be negative if species $k$ is a reactant). More details on the diffusive term can be found in section 2.4.4.

### Conservation of Energy

The conservation of energy also incorporates diffusion effects, from both thermal and species diffusion. An additional term is added to take into account the work of pressure forces within the domain. There again, viscous dissipation is neglected. The

energy inputted from the discharge is also included in the full expression as $w_{input}$:

$$\frac{\partial(\rho e)}{\partial t} = -\frac{1}{r}\frac{\partial\left(r\rho ue - r\lambda\frac{\partial T}{\partial r} + r\sum_k j_k h_k\right)}{\partial r} - p\frac{\partial u}{\partial r} + w_{input} \tag{2.15}$$

More detailed development and explanation of the conservation equations can be found in the textbook by Kee and Coltrin [34].

### 2.4.4 Species Diffusion

The species diffusion intervenes in both the species and energy conservation equations (see equations 2.14 and 2.15). In both equations, the diffusion flux of species $k$, $j_k(r,t)$, is determined using a mixture-averaged approximation of the diffusion coefficient noted $\bar{D_k}$. The diffusion is captured using the systems of equations given by the Cantera framework for one-dimensional reacting flow:

$$\begin{aligned} j_k^* &= -\rho\frac{W_k}{W}\bar{D}_k\frac{\partial X_k}{\partial r} \\ j_k &= j_k^* - Y_k\sum_m j_m^* \end{aligned} \tag{2.16}$$

### 2.4.5 Energy Balance

The internal energy $e$ that appears in the energy conservation equation (see equation 2.15) can be developed as:

$$e = e_{kinetic} + e_{thermal} + e_{chemical} + e_{plasma} \tag{2.17}$$

So the internal energy term $e$ includes 4 different forms of energy:

- the kinetic energy $e_{kinetic}$ defined as:

$$e_{kinetic} = \frac{1}{2}u^2 \tag{2.18}$$

The kinetic energy is the only component of the internal energy that emerges from the 1D effects. In our code, it is neglected compared to the other forms of energy as the speed of the gas $u$ is much smaller than the speed of sound.

- the thermal energy, also known as translational energy $e_{thermal}$:

$$e_{thermal} = \bar{c}_v T \tag{2.19}$$

- the chemical energy $e_{chemical}$, which includes enthalpy of formation

- the "plasma energy", or the energy stored in excited states and ions $e_{plasma}$:

$$e_{plasma} = e_{rot} + e_{vib} + e_{elec} + e_{ions} \tag{2.20}$$

Where $e_{rot}$ has been neglected in our mechanism as rotational-translational equilibrium is assumed, and the other forms of energy can be formulated under the form:

$$e_{vib} = \frac{N}{\rho} \sum_k X_k \epsilon_k \tag{2.21}$$

With $\epsilon_k$ is the energy stored in the excited state $k$.

The specific enthalpy is linked with the specific internal energy through:

$$h = e + \frac{p}{\rho} \tag{2.22}$$

By integrating the energy conservation equation (see equation 2.15) over a control volume $r < r_m$, we deduce the following instantaneous power balance:

$$W_{input} = \underbrace{2\pi \int_0^{r_m} \left( \frac{\partial e}{\partial t} + p \frac{\partial u}{\partial r} \right) r dr}_{\text{internal fluid}} + \underbrace{2\pi r_m \left[\rho u e\right]_{r_m}}_{\text{out flow}} + \underbrace{2\pi r_m \left[ \sum_k j_k h_k - \lambda \frac{\partial T}{\partial r} \right]_{r_m}}_{\text{out diffusion}} \tag{2.23}$$

Which holds true if no energy is inputted outside of the control volume. In that case, the input power $W_{input}$ can be retrieved using:

$$W_{input}(t) = 2\pi \int_0^{r_m} w_{input}(r,t) r dr \tag{2.24}$$

### 2.4.6 Boundary Conditions and Sponge Layer

#### Centerline

The axisymmetric boundary condition at the centerline ($r = 0$) is a zero-flux condition, and enforces zero advection and diffusion:

$$u(r=0,t) = 0,\ \frac{\partial T}{\partial r}(r=0,t) = 0,\ \text{and for every species } k\text{: } j_k(r=0,t) = 0 \tag{2.25}$$

#### Sponge Layer

The other boundary is an open boundary, i.e., a boundary that allows for the free outflow of species and waves. In our numerical implementation, we enforced no particular open boundary conditions but instead added an Absorbing Sponge Zone (ASZ) [87] to absorb reflections that occurred at the boundary. This was required to handle strong pressure waves that occurred at much shorter timescales than the flame propagation process to be tracked. In this manner, smaller computational domains could be used. This numerical technique consists of adding a layer at the edge of the computational domain where the model equations (equations 2.12, 2.13, 2.15) are extended to include an additional term of the form:

$$\frac{\partial \chi}{\partial t} = f(\chi, t, r) - \sigma \left(r - r_0\right)^2 (\chi - \chi_0) \tag{2.26}$$

Where $r_0$ is the distance at which the sponge layer begins, and $\chi_0$ is the asymptotic term to which the sponge layer converges. For the results presented, we use $\chi_0 = \chi(t = 0, r = r_{\max})$. The value of the coefficient $\sigma$ determines the degree of absorption. It is chosen depending on the expected incoming perturbations, to ensure full absorption

before it reaches the boundary, and scales with:

$$\sigma \sim \frac{c}{(r_{\max} - r_0)^3} \tag{2.27}$$

Where $c$ is the speed of propagation of the perturbation. If several perturbations are expected, the largest propagating speed should be used, or the sound speed. The coefficient must be carefully selected, as a too-large coefficient will cause unwanted reflections within the sponge layer.

### 2.4.7 Summary of Assumptions

- Local kinetic energy is much smaller than the local thermal energy.
- Excited species and ions created by the plasma do not diffuse.
- Flow is inviscid.
- Thermodynamic properties of any species at a given temperature can be approximated using the NASA-7 polynomials.
- Plasma chemistry is evolving much more rapidly than combustion chemistry.
- Combustion chemistry evolves much more rapidly than fluid variations.
- Rotational-translational equilibrium is assumed.

## 2.5 Chapter Summary

This chapter describes the various models and methods used in this work. First, we introduce a zero-dimensional chemical model developed in this work. This 0D model is then validated against a test case from the literature. Plasma and combustion kinetics are gathered to depict plasma-assisted combustion by NRP discharges using a "surrogate fuel", meant to represent more closely fuels used in aviation. Finally, we describe the characteristics of a one-dimensional model of radial ignition by NRP discharges (cylindrical coordinates) developed in this work.

# Chapter 3

# Numerical Results for Plasma-Assisted Ignition

In this section, results from the zero-dimensional and one-dimensional solvers presented in chapter 2 are presented and analyzed. Predictions from the combustion and plasma kinetics developed to describe plasma-assisted combustion of the surrogate fuel are compared with other mechanisms from the literature. The influence of temperature and gas composition on the benefits of plasma assistance for zero-dimensional ignition is studied. We also present and discuss results obtained for one-dimensional radial ignition and flame propagation from a hot kernel and from a plasma kernel of various sizes and actuated at different pulse repetition frequencies.

## 3.1 Validation of Surrogate Fuel Mechanism

### 3.1.1 Differences in Kinetics

In his Ph.D. dissertation of 2011 [19], Ashim Dutta compares predictions of various combustion mechanisms for the combustion of ethylene, with and without plasma assistance. In Dutta's work [19], the plasma kinetics used is a combination of nonequilibrium air plasma chemistry taken from Kossyi et al. [38] and a reaction set for hydrogen and hydrocarbon fuel dissociation processes in the plasma based on experiments from

Uddi et al. [81]. These reactions involving ethylene are not included in our plasma mechanism (see appendix A). However, we include electron-impact dissociations and ionizations of ethylene which are not incorporated in Dutta's work [19]. In Dutta's thesis, results are compared using either GRI3.0 [71] or UCSD [1] for the fuel/air combustion mechanism. Since we use USC Mech II [82] for the combustion mechanism, both the plasma kinetics and the combustion kinetics used by Dutta [19] are different from what we developed in this work, making it a good point of comparison.

### 3.1.2 Thermal Ignition

The first comparison case is the thermal ignition of a stoichiometric ethylene-air mixture at atmospheric pressure and from an initial temperature of 1100 $K$ (above auto-ignition temperature for ethylene). Results from Dutta [19] using either GRI3.0 [71] or USCD [1] as combustion mechanisms are compared with predictions from our coupled plasma and combustion kinetics model on figure 3-1.

We can note that predictions using the USC Mech II (this work) fall within the expected range of uncertainty of combustion models for ethylene ignition. Overall, the ignition delay time by the three mechanisms is of the same order of magnitude, ranging from 2 $ms$ up to 9 $ms$, with the case of USC Mech II (this work) falling between the predictions of the UCSD and GRI3.0 mechanisms. It is important to note that, despite being the most widely accepted combustion mechanism for methane ($CH_4$), the development of GRI3.0 [71] has not been focusing on the combustion of larger hydrocarbons like ethylene ($C_2H_4$). Therefore, discrepancies in ignition delay time can be partially explained by the fact that the GRI3.0 does not provide reliable predictions for ethylene combustion. In conclusion, predictions from Dutta's mechanism [19] using UCSD [1] remain fairly close to USC Mech II [82], falling within the range of uncertainties in ethylene ignition delay time predictions described by Xu and Konnov [84].

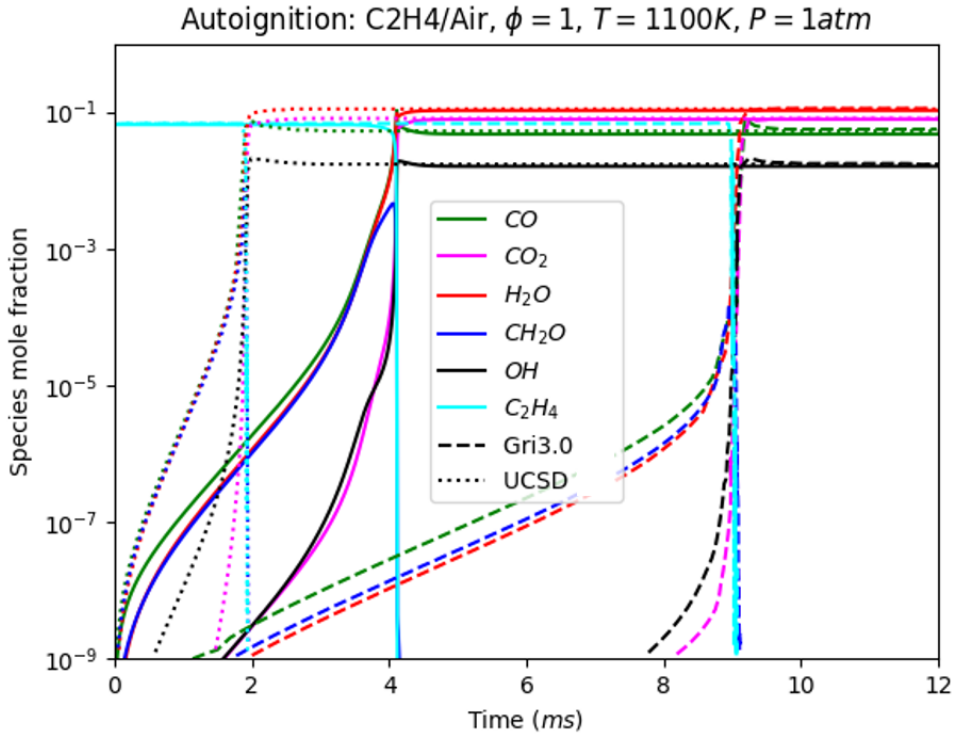


(a) Main species: data from [19] (dashed and dotted) and USC Mech II [82] (solid-line)

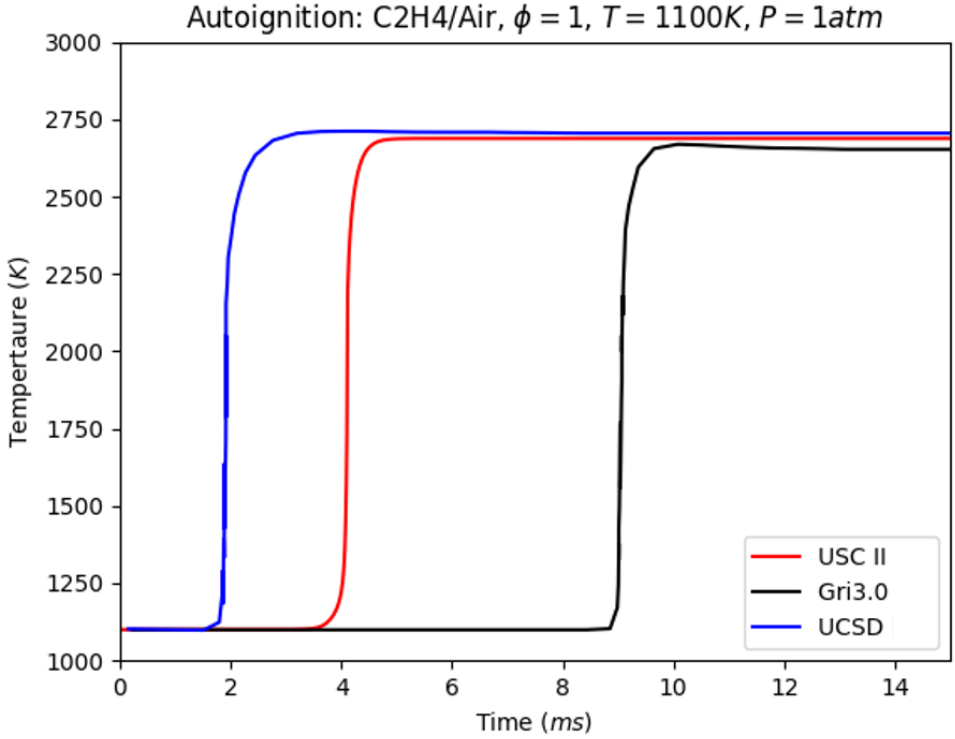


(b) Temperature: data from [19] (black and blue) and USC Mech II [82] (red)

Figure 3-1: Validation of surrogate fuel mechanism: thermal ignition.

### 3.1.3 Ignition by a Single Nanosecond Pulse Discharge

As seen in section 2.1.2, a single pulse test case comparison can often help explain discrepancies observed with multiple pulses. In his thesis [19], Dutta also presents predictions of the evolution of the mole fractions of the main species after a single pulse applied at $t = 0$. The pulse energy is 0.5 $mJ/cm^3$ and the pulse peaks at 250 $Td$. We used the electron cutoff method described in section 2.2 to ensure a matching of the energy deposited. Initially, the mixture is composed of a stoichiometric mixture of ethylene-air at 700 $K$ at atmospheric pressure. There again, Dutta compares predictions using either GRI3.0 [71] and UCSD [1] as combustion mechanisms [19]. Results are shown in figure 3-2: dashed and dotted lines are results from Dutta [19], solid lines are predictions from this work.

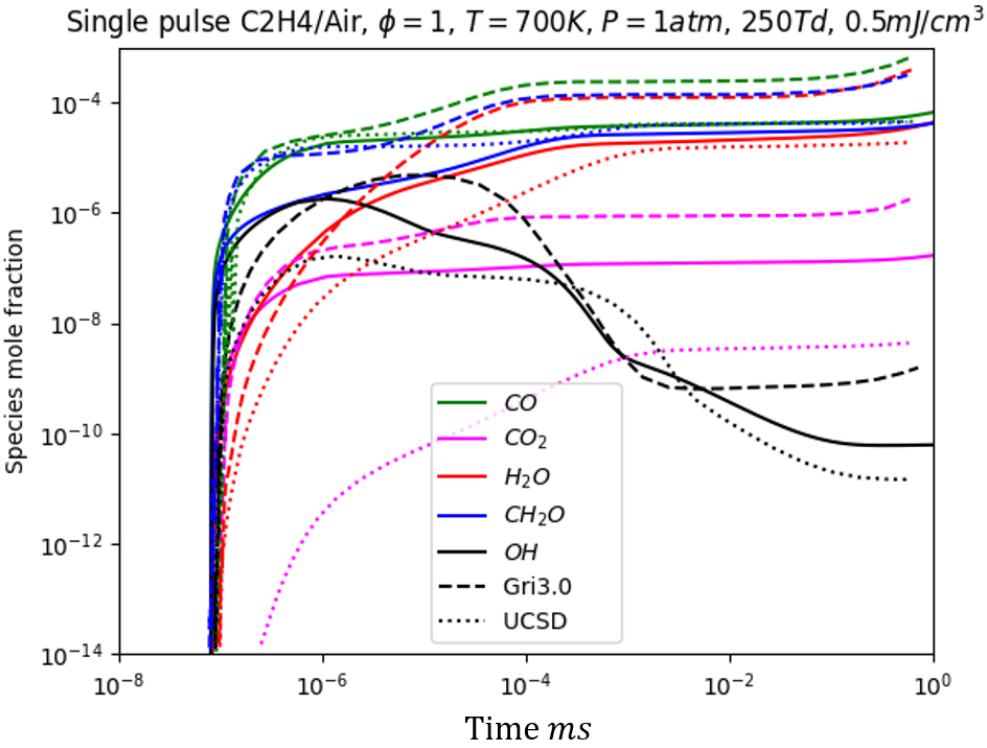


Figure 3-2: Validation of plasma mechanism: single pulse.

Results from figure 3-2 show good agreement between predictions from Dutta's model [19] (dashed and dotted lines) and the plasma-combustion kinetics developed in this work (solid line). The kinetics model developed in this work falls within the range

of uncertainties delimited by the GRI3.0 [71] and UCSD [1] for most species. Using conclusions from section 3.1.2, we can conclude that both the plasma kinetics and the combustion mechanisms selected for the surrogate fuel predict combustion dynamics in good agreement with the literature. Further study of the plasma mechanism is conducted in the following section.

### 3.1.4 Ignition by NRP Discharges

After comparing results for thermal ignition (section 3.1.2) and ignition enabled by a single pulse (section 3.1.3), we now compare predictions for multiple pulses at a 40 $kHz$ repetition frequency. Conditions (mixture, pressure, and temperature) and pulse shape and energy are the same as the ones depicted in section 3.1.3. Results are shown in figure 3-3.

Results shown in figure 3-3 reveal large differences in predictions between the data from Dutta's thesis [19] and this work. Despite having a good agreement for thermal ignition (see section 3.1.2) and single pulse (see section 3.1.3) cases, this work predicts a significantly smaller ignition delay time than Dutta's model [19] predicts using both GRI3.0 [71] or UCSD [1]. These differences are likely caused by the fact Dutta implemented a heat loss term for plasma simulations that participates in the ignition delay as well as in the decrease of gas temperature after ignition (see figure 3-3-b), but does not have any significant effect at the timescale of a single pulse (see section 3.1.3).

## 3.2 Influence of Temperature

Gas conditions have a critical influence on how the energy is deposited and therefore on the effects of the discharge. If the mixture is fixed, gas pressure and temperature also have an important effect. In our study, the gas temperature is a key parameter because it drives many reactions necessary to the combustion process. Plasma-assisted combustion chemical studies often focus on gas at ambient temperature. However, as shown in table 2.2, plasma assistance could also be used in high-temperature environ-

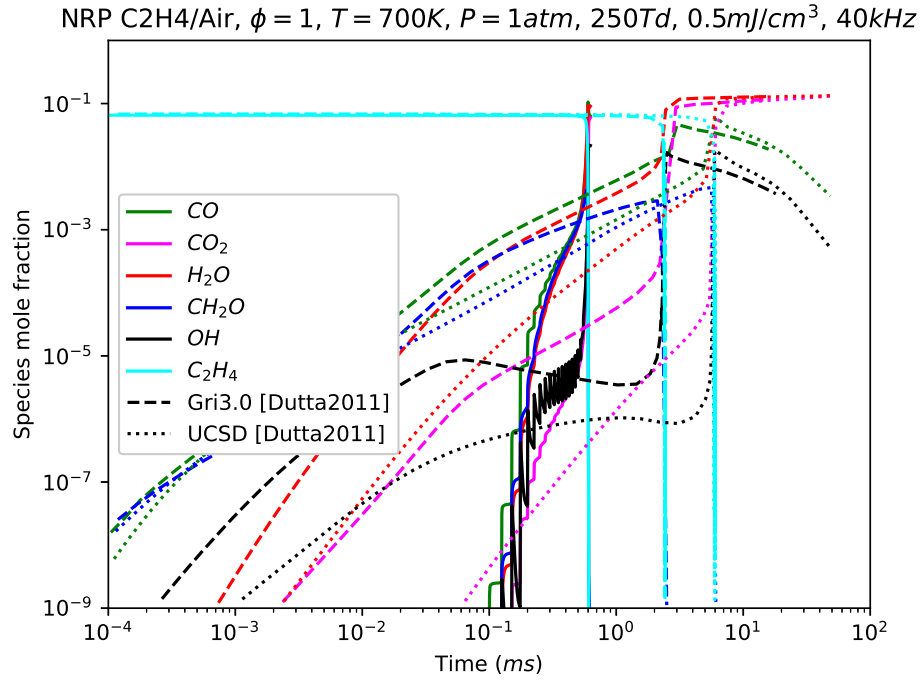


(a) Main species: data from [19] (dashed and dotted) and this work (solid-line)

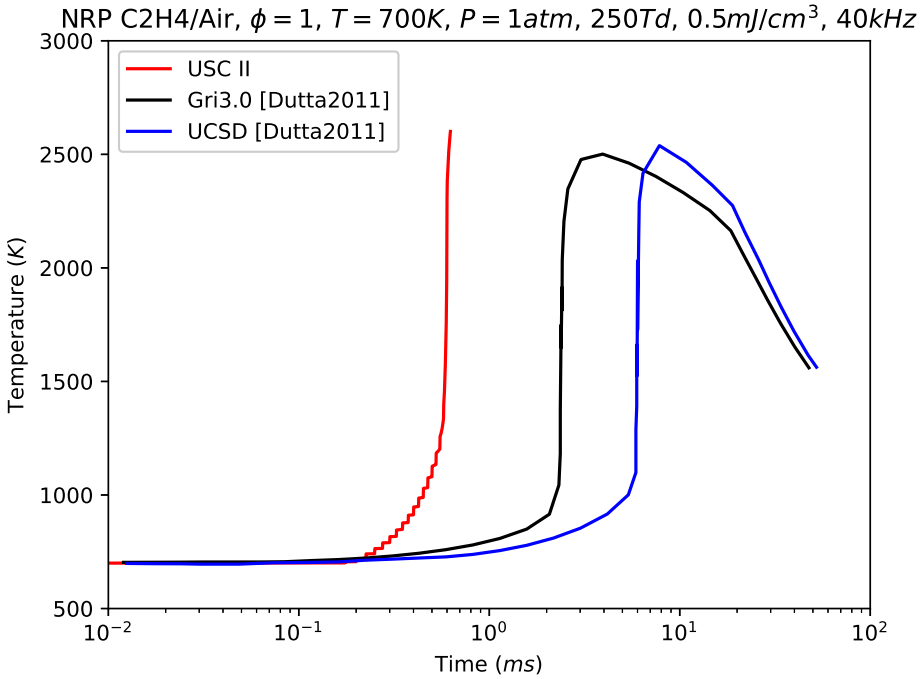


(b) Temperature: data from [19] (black and blue) and this work (red)

Figure 3-3: Validation of plasma mechanism: multiple pulses.

ments, up to 1300 $K$. Therefore, it becomes paramount to quantify the consequences of high-temperature initial conditions on the admitted benefits of plasma assistance.

We conducted several 0D simulations using the kinetics described in section 2.3 for our surrogate fuel (36% methane + 64% ethylene). The gas is initially composed of surrogate fuel and air mixed at an equivalence ratio of $\Phi = 0.66$ and at atmospheric pressure. The pulse repetition frequency and peak reduced electric field are kept identical between simulations (40 $kHz$ and 180 $Td$ respectively). However, we change the pulse width (gaussian shape) to modify the amount of energy deposited. We also vary the initial gas temperature from 800 $K$ up to 1200 $K$. For each simulation, we change the initial gas temperature and the average energy deposited per pulse to plot trends in ignition delay time. The case where the average energy deposited per pulse is 0 corresponds to thermal ignition (no plasma). Results are shown in figure 3-4.

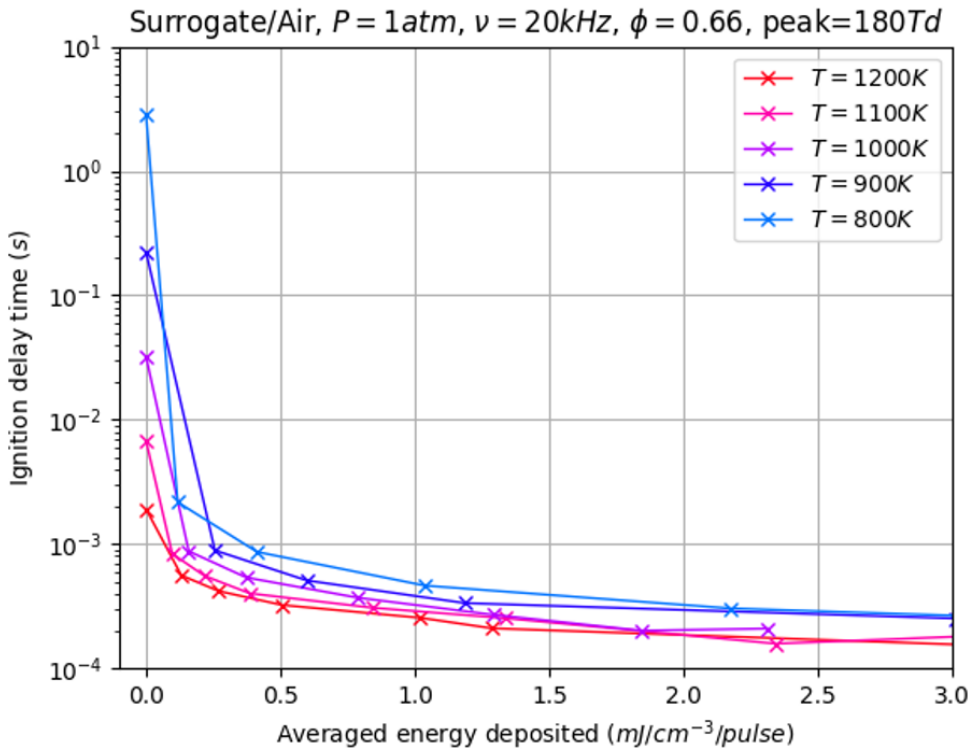


Figure 3-4: Influence of temperature and pulse energy on plasma benefits.

Predicted ignition delay times with varying initial temperature and average energy per pulse are shown in figure 3-4. First of all, we can note that the auto-ignition delay time (no average energy deposited) decreases from 3 $s$ down to 2 $ms$ when the gas temperature is increased, which is to be expected. We can also note the energy deposited by the plasma has a huge influence on ignition at low energies ($< 500\ \mu J/cm^3/pulse$). From there, further increasing the energy deposited becomes less and less beneficial, for all temperatures. Looking at the influence of temperature, results show that increasing the temperature reduces the benefits of plasma assistance on ignition delay reduction. It is important to note however that we pulsed through ignition, so if the average energy deposited per pulse can be adapted independently changing the pulse shape, the total energy deposited also depends strongly on the ignition delay time. The results can be interpreted as an indication that, at high temperatures, the high-temperature environment is sufficient for the traditional combustion chain initiation reactions to be active and the relative benefits of the additional radical-seeding reactions from the plasma are decreased. In conclusion, for similar gas and pulse conditions, the relative benefits of plasma assistance tend to decrease at high temperatures. Increasing the average energy deposited per pulse has little effect, but increasing the pulse repetition frequency may help further increase the ignition delay time.

## 3.3 Influence of Equivalence Ratio and Dilution

### 3.3.1 Conditions

We conducted several simulations using the zero-dimensional model described in section 2.1. The gas is initially composed of a mixture at 1000 $K$ and 1 $atm$ of nitrogen, oxygen, and surrogate fuel (see section 2.3) in varying proportions depending on the test case. Gas composition strongly affects the energy deposited per pulse as it determines the ionization rate and thus the electron density. In order to ensure comparable values of the energy deposited per pulse over the domain of mixtures, we

used the electron cutoff method (see section 2.2). The plasma is pulsed at 20 $kHz$ at a 180 $Td$ peak, with a maximum of 50 $ns$ duration. The reduced field is cut off when the electron density reaches $10^{14}$ $cm^{-3}$. The resulting averaged energy deposited per pulse over the range of mixtures is plotted in figure 3-5-a. The gas composition at a point within the triangle domain can be retrieved by doing the ratio of the distances to the 3 vertices representing nitrogen ($N_2$), oxygen ($O_2$), and surrogate fuel. We can see in figure 3-5-a that the energy per pulse is somewhat similar between cases. As seen in figure 3-5-b however, the total energy deposited until ignition varies on a range from 15 $mJ \cdot cm^{-3}$ up to 350 $mJ \cdot cm^{-3}$ depending on the ignition delay observed.

### 3.3.2 Comparison with Pure Thermal Effect

For each configuration, plasma discharges are applied through ignition. We can then plot the ignition delay time for each mixture, as shown in figure 3-6-a. We can see that the mixture has an effect on ignition delay time, which can range from 50 $\mu s$ to 430 $\mu s$ for the conditions presented. However, the ignition delay time alone is not sufficient to pinpoint what mixture is most susceptible to plasma assistance. Indeed, as shown in figure 3-5, even if the energy per pulse is kept somewhat constant between cases, the total energy deposited by the plasma depends on ignition delay time and therefore is intimately linked with results shown in figure 3-6-a. To be able to compare cases, we run a baseline set of auto-ignition simulations (no plasma) where the plasma input energy is assimilated to an initial temperature rise. Note that this is not a fair comparison of thermal versus non-thermal effects as the rate of energy delivery is different in both cases. E.g. for the thermal energy the energy input is instantaneous and set as an initial condition. For each mixture case, the initial energy for the auto-ignition computation is raised from $T_0 = 1000$ $K$ to a temperature $T_1$ based on the energy that the plasma deposited during the plasma-assisted ignition simulation $\mathcal{E}_{tot}$ through:

$$T_1 = T_0 + \frac{RT_0}{p_0 M_0 c_p} \mathcal{E}_{tot} \tag{3.1}$$

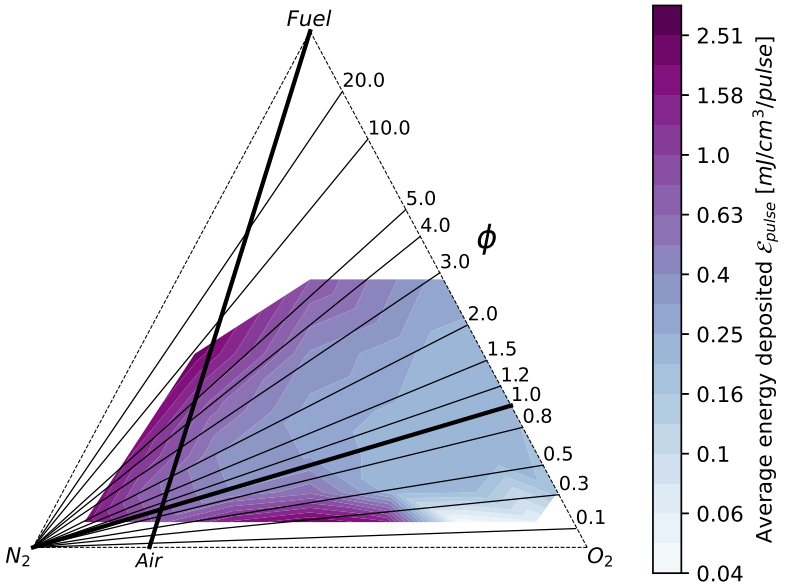


(a) Averaged energy deposited per pulse

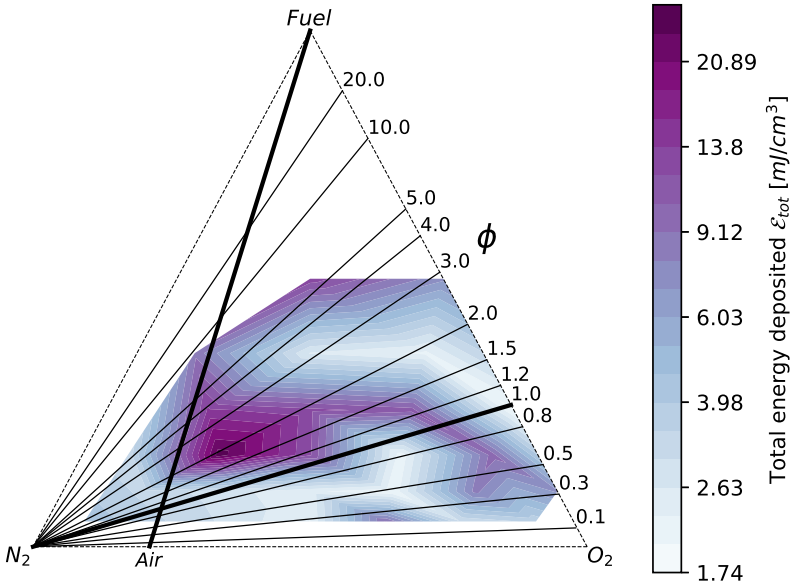


(b) Total energy deposited until ignition

Figure 3-5: Ternary results for the surrogate fuel: energy deposited.

Where $M_0$ refers to the molar mass of the initial mixture and the specific heat at constant pressure $c_p$ is considered constant. The resulting auto-ignition delay time obtained with this new initial temperature condition is shown in figure 3-6-b.

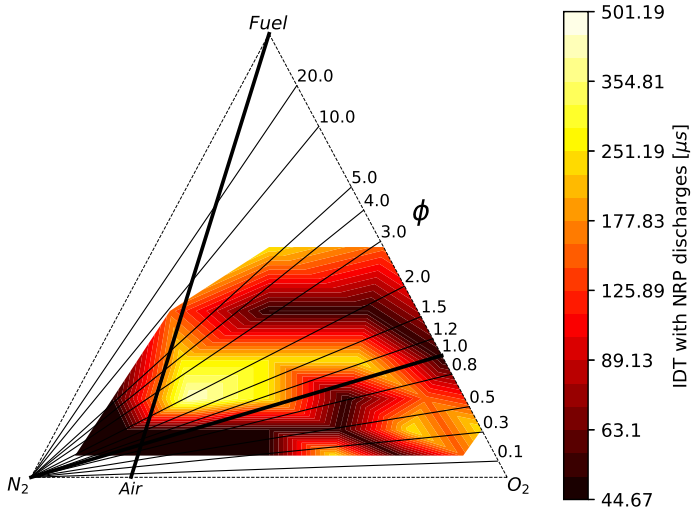


(a) Ignition delay time with NRP discharges

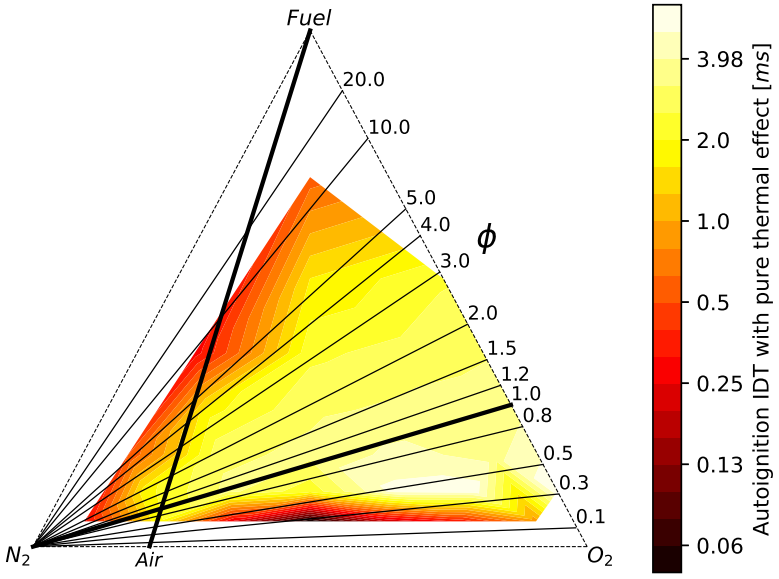


(b) Ignition delay time with pure thermal effect

Figure 3-6: Ternary results for the surrogate fuel: ignition delay times.

The plasma-deposited energy can be divided into two forms: (i) thermal energy and (ii) chemical energy. Thermal energy is the part of the energy deposited that ends up raising the gas temperature. Chemical energy is the part of the electrical energy that leads to dissociations and the creation of unstable, more energetic chemical species. Figure 3-6-b shows what would be the ignition delay time if all the deposited energy turned into thermal energy at the initial time. More precisely, it assumes all the energy deposited by the pulse is instantly delivered as a temperature rise. Figure 3-6-a shows the complete picture, where both thermal and chemical effects of the plasma are considered.

We can see in figure 3-6 that, for most mixtures, the ignition delay time with plasma actuation remains lower than what would give an instantaneous pure thermal effect. This observation means the chemical effects of the plasma are more effective than what a pure thermal effect would give for the same energy. However, for some mixtures, chemical effects are not always beneficial. A ratio of the ignition delay times with pure thermal effect to ignition delay time with NRP discharges is given in figure 3-7.

Ternary results plotted in figure 3-7 show that gas composition has a strong influence on what proportion of the energy deposited by the plasma goes into thermal end chemical effects, but also how the chemical energy deposited affects the ignition phase. The generation of oxygen radicals from the dissociation of $O_2$ molecules is known to be a chemical pathway that greatly enhances ignition. But other targets of energy deposition from the plasma into the chemical energy can be less beneficial for ignition, at least less beneficial than a pure thermal input.

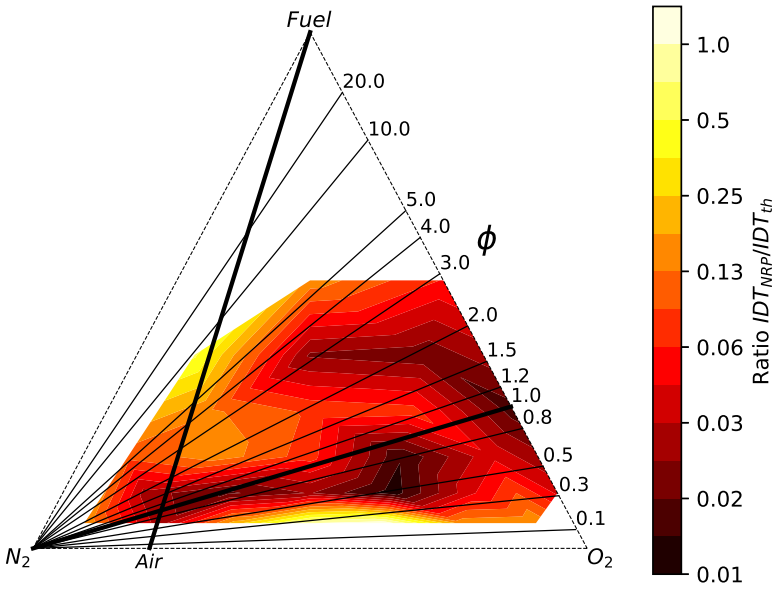


Figure 3-7: Ternary results for the surrogate fuel: benefits of plasma chemical effects on ignition.

## 3.4 Radial Ignition by a Hot Kernel

### 3.4.1 Conditions

In this section, we look at the one-dimensional radial ignition of a stoichiometric methane-air mixture by a high-temperature kernel. At $t = 0$, the gas is at rest (no radial velocity, $u = 0$) at uniform pressure of $1atm$ and uniform composition. We force a radial temperature profile so that $T = 2000\ K$ for $r < 1\ mm$ and $T = 1000\ K$ elsewhere. Auto-ignition temperature of stoichiometric methane/air is about $840\ K$ [21], although experiments have shown that such mixtures can auto-ignite at temperatures as low as $600\ K$ [64]. Both the hot and cold regions in our simulation test case are thus above the auto-ignition temperature for methane. This particular temperature profile ensures ignition happens close to the centerline and propagates out. Figure 3-8 shows zero-dimensional predictions of auto-ignition delay times in both regions from starting conditions. Results show that the 0D ignition delay time

of the mixture in the hot kernel is around 40 $\mu s$, and 1 $s$ in the 1000 $K$ region. These zero-dimensional results help us to bound the ignition delay time of the one-dimensional problem.

### 3.4.2 Note on Kinetics

For the following one-dimensional simulations (presented in sections 3.4 and 3.5), the test cases are limited to methane/air mixtures. Therefore, we did not use the combustion and plasma kinetics described in section 2.3 for the surrogate fuel (detailed in appendix A). Such a decision has been made to ensure short computational time by reducing the size of the mechanism used. The plasma kinetics are taken from Bak et al. [6] and have previously been used for modeling methane-air flame propagation coupled with NRP discharges [54]. More details regarding the plasma kinetics are given in Pavan's thesis [53] (appendix B). Since only methane is used as fuel, we opted for the GRI3.0 [71] mechanism as combustion kinetics since it performs well for methane (see section 2.3).

### 3.4.3 1D Results and Analysis

Results of one-dimensional radial auto-ignition by a hot kernel are shown in figures 3-9 and 3-10. The color gradient represents the time evolution. The black line shows the initial conditions.

In one-dimensional systems, finding an exact value of the ignition delay time becomes difficult because ignition seems to appear progressively in different locations simultaneously in a region called the ignition kernel. However, a rough approximation of the ignition delay time can be derived. In this test case, ignition seems to occur in about 40 $\mu s$, which is in accordance with the zero-dimensional preliminary results of auto-ignition shown in figure 3-8. The fact that the delay for ignition in the hot kernel is very close to the zero-dimensional ignition delay time prediction at 2000 $K$ reveals that the kernel is sufficiently large and ignition sufficiently fast so as to neglect

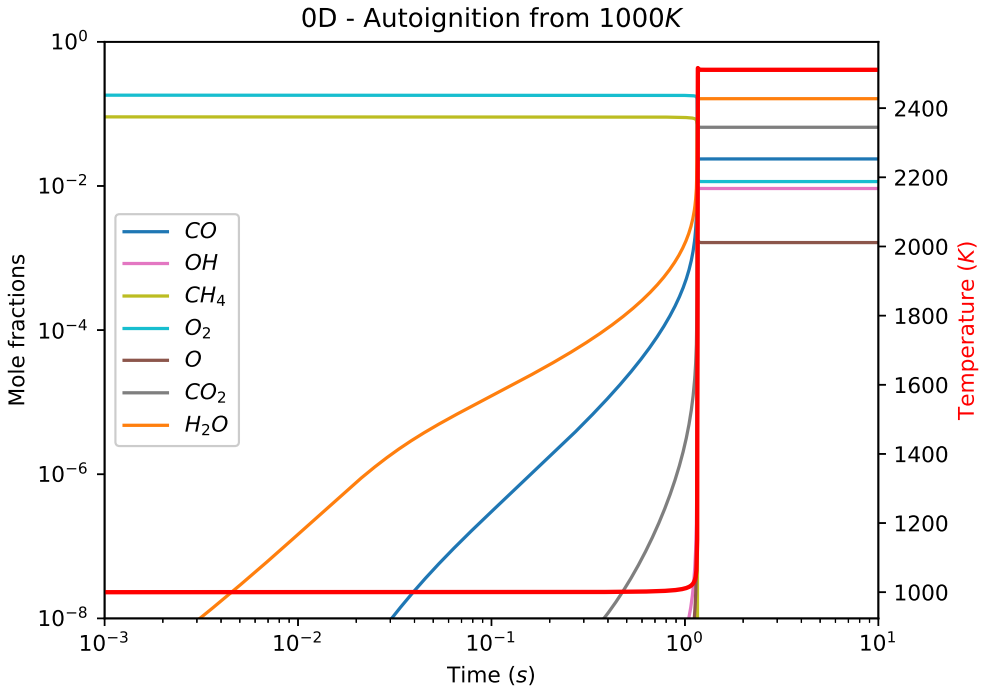


(a) Zero-dimensional auto-ignition outside of the hot kernel region

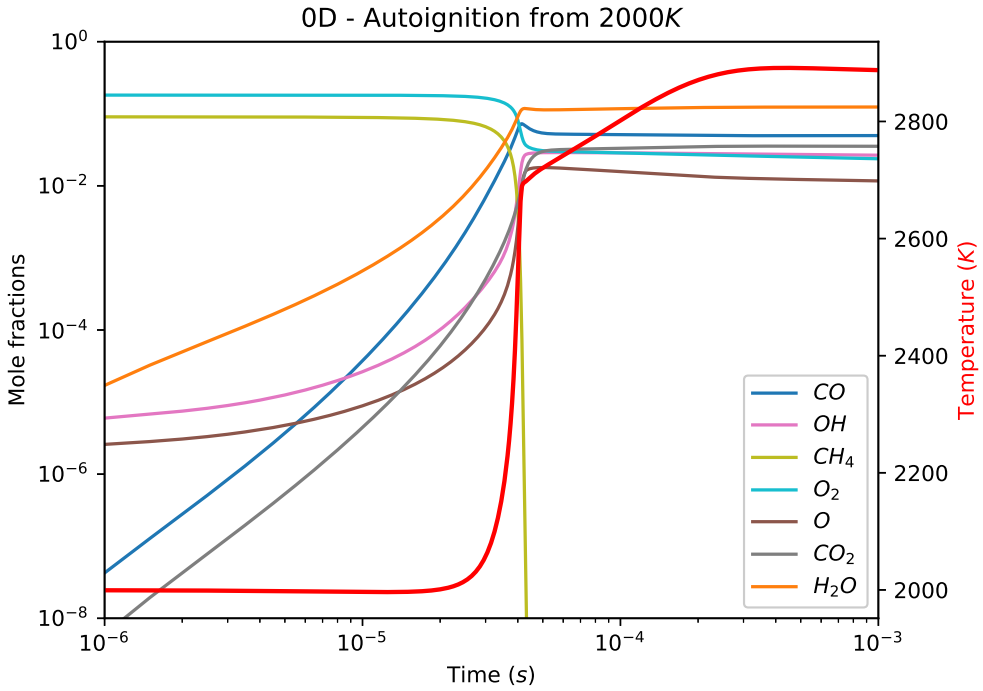


(b) Zero-dimensional auto-ignition in the hot kernel region

Figure 3-8: 0D auto-ignition for 1000 $K$ and 2000 $K$.

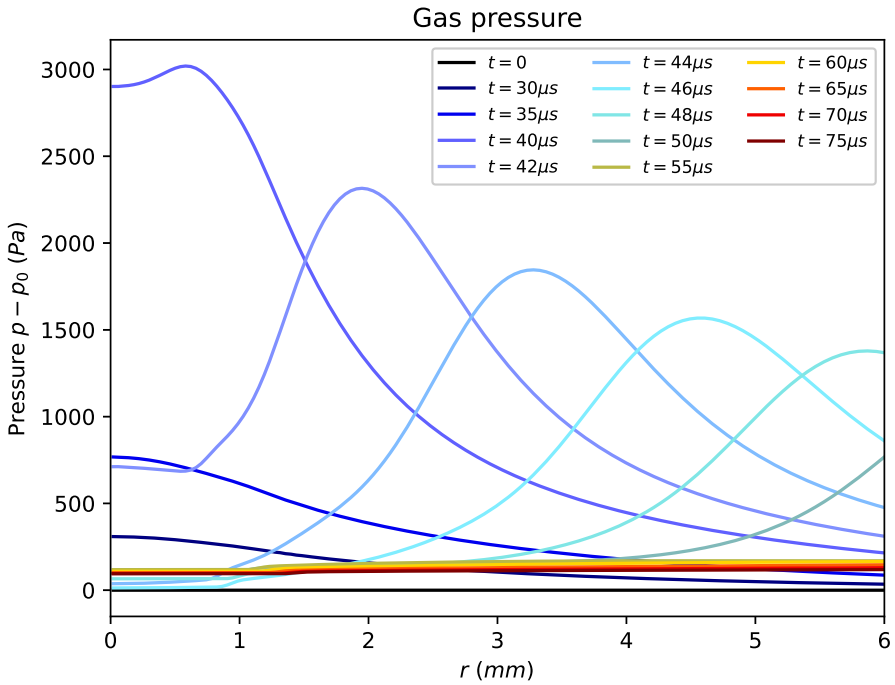


(a) Gas pressure

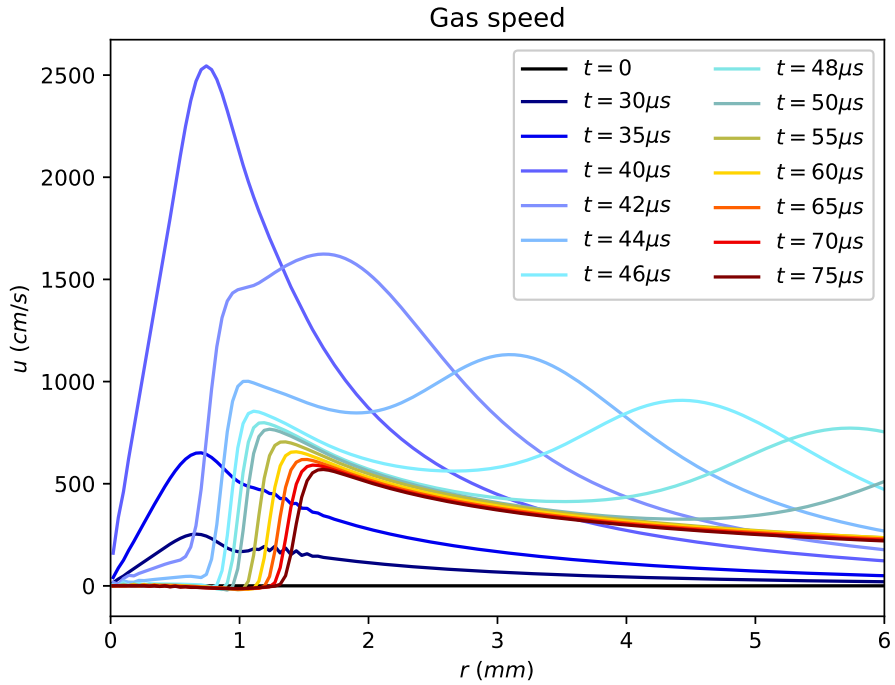


(b) Gas radial velocity

Figure 3-9: 1D hot kernel ignition: pressure and velocity.

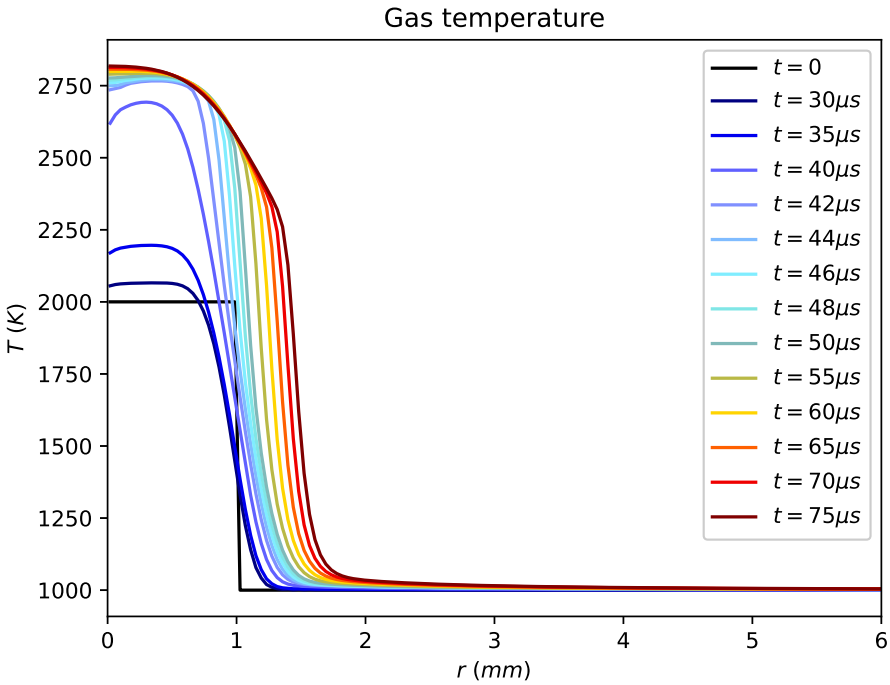


(a) Gas temperature

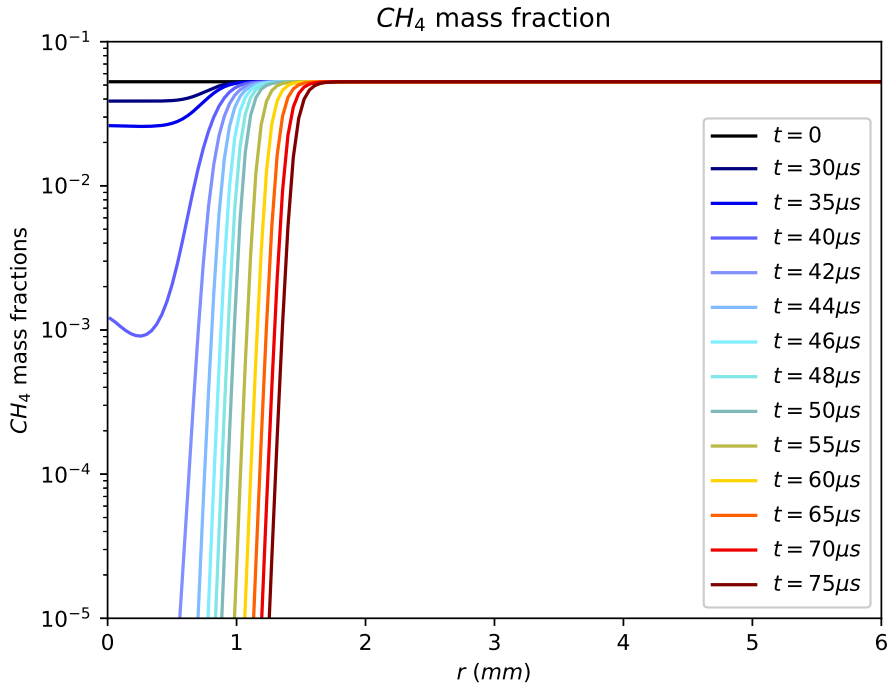


(b) Methane mass fraction

Figure 3-10: 1D hot kernel ignition: temperature and methane mass fraction.

diffusion effects (species and thermal).

At ignition, both gas pressure and gas velocity reach a maximum in a location distant from the centerline that we can interpret as the ignition kernel radius (see figure 3-9). This region of high pressure (3% of the atmospheric pressure) is caused by an abrupt consumption of the fuel in the ignition kernel, which leads to a sharp increase in temperature (see figure 3-10). This creates a pressure front which leads to the apparition of a large pressure wave. This pressure wave propagates radially out at the local speed of sounds until leaving the domain (see figure 3-9). Because of the radial configuration, the amplitude of the pressure wave decreases as it propagates out as its front area increases.

The flame front is distinct from the pressure wavefront as it is driven by chemistry and separates two regions of different gas compositions. Therefore, the flame front can be located using spatial gradients in species concentrations, like methane (see figure 3-10). In the simulation results shown in figures 3-9 and 3-10, the flame front seems to fully form quickly after ignition at $r \approx 0.6mm$. Therefore, the flame front forms initially within the hot kernel, which means the hot kernel does not ignite uniformly: the region close to the centerline at $r < 0.6mm$ ignites first, probably because it is less affected by thermal and species diffusion effects that happen on the edge of the hot kernel.

If a pressure wave propagation velocity mainly depends on the temperature (for ideal gas $c_{sound} = \sqrt{\gamma R_g T}$), the flame speed also strongly depends on gas composition. In regions where the methane and oxygen molecules are already partially dissociated, the flame front propagation speed is increased. The results shown on figures 3-9 and 3-10 show similar conclusions. Indeed, the flame front propagating radially out progressively slows down as it leaves the hot kernel region where the gas has been pre-treated for combustion by the high temperature. If the flame front propagates very fast just after ignition when it is coupled with the pressure wave, it slows down to about 10 $m \cdot s^{-1}$. This order of magnitude is in good agreement with predictions from

the literature: Wang et al. [83] present a formula for a wide pressure and temperature range from which flame speed at 1000 $K$ should be around 6 $m \cdot s^{-1}$, but at 2000 $K$ it increases to 188 $m \cdot s^{-1}$.

Running the simulations for longer timescales and large computational domains, we would expect the pressure wave to propagate at the same speed but its amplitude would decrease and eventually die out in dissipation. However, the flame front is expected to not dissipate and asymptotically reach a steady-state propagation speed equal to the laminar flame speed in these particular conditions. It is important to note that the gas bulk radial velocity (plotted in figure 3-9-b) is distinct from the pressure wave velocity (sound speed) and the flame propagation velocity. If the gas bulk velocity peaks at 25 $m \cdot s^{-1}$ at the edge of the ignition kernel, it quickly decays and remains lower than the flame speed.

## 3.5 Radial Ignition by NRP Discharges

### 3.5.1 Conditions

After studying radial ignition and flame propagation when the mixture is auto-ignited from a hot kernel (see section 3.4), we want to study the case where ignition is triggered by Nanosecond Repetitively Pulsed (NRP) plasma discharges. The conditions are similar to the one depicted in the previous section (see hot kernel conditions in section 3.4.1), except the gas temperature is set uniform at 1000 $K$ (no high-temperature region). According to zero-dimensional simulations, the auto-ignition delay time for the initial mixture is on the order of 1 $s$ (see figure 3-8-a). As will be seen in the next section, the kinetic effects of the plasma greatly accelerate ignition.

For the simulations presented in this section, gas heating is not taken into account during the plasma chemistry modeling (gas temperature is considered constant and equation 2.3 is not activated), which means plasma has only kinetic effects. the plasma model has since been extended to also include thermal effects (both fast, $ns$-timescale

heating from electronic relaxation; and slow, $ms$-timescale heating from vibrational relaxation), and results will be presented in a forthcoming publication. The plasma discharges are applied spatially in a region where $r < r_p$ where $r_p$ refers to the size of the plasma kernel. The reduced electric field is inputted as uniform in that region. However, the reduced electric field depends on time, following a Gaussian evolution:

$$\frac{E}{N}(r,t) = \begin{cases} (E/N)_{max} \exp\left[-\frac{1}{2}\left((t - t_{peak})/\Delta t_\sigma\right)^2\right] & \text{if } r \leq r_p \\ 0 & \text{elsewhere} \end{cases} \tag{3.2}$$

Where $\Delta t_\sigma = \Delta t_{pulse}/2\sqrt{2\ln 2}$ and $t_{peak} = 5\Delta t_\sigma$, $\Delta t_{pulse}$ being the full width at half maximum of the pulse. We used $(E/N)_{max} = 180\ Td$ and $\Delta t_{pulse} = 20\ ns$.

For a given mixture, reduced electric field, and set of electron-collision cross sections, we can predict where the electric energy inputted is deposited using the BOLSIG+ solver [24]. For the initial conditions depicted (stoichiometric methane/air mixture at 1000 $K$ and 1 $atm$, and $10^3\ cm^{-3}$ electron density), the energy deposition rate in the different pathways is plotted for the given pulse shape on figure 3-11. We can see that a vast majority of the electrical energy of the discharge is deposited into excited states of nitrogen and oxygen (which are the main species), especially in vibrationally and electronically excited states. Those deposition pathways are subject to change as the mixture and conditions evolve during and between the pulses.

### 3.5.2 Large Plasma Kernel Actuated at Low Frequency

We conducted a first simulation with a large plasma kernel size of $r_p = 3.54\ mm$ and low frequency $f = 10\ kHz$. Predictions of gas temperature, gas speed, methane mass fraction, and carbon monoxide mass fraction are given in figures 3-12-a, 3-12-b, 3-13-c, and 3-13-d respectively. The color gradient of the lines represents time evolution. The vertical dashed black line delimits the plasma kernel region.

Results show that ignition occurs after about 5.8 $ms$, which is significantly faster than the auto-ignition delay time given by zero-dimensional simulations (1 $s$, see

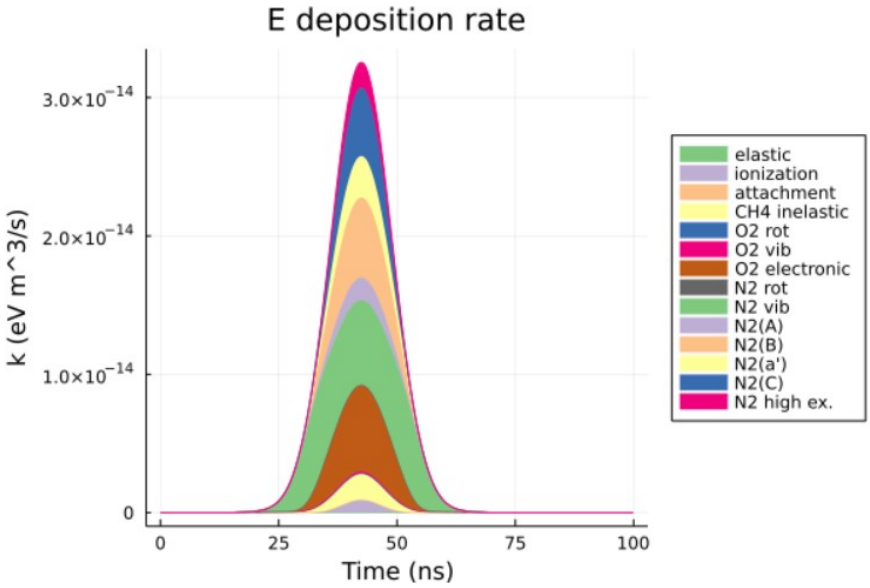


Figure 3-11: Energy deposition pathways along the pulse shape.

figure 3-8-a), which highlights the significant kinetic effects the plasma can have on ignition enhancement. Contrary to the test case of ignition by the high-temperature kernel (see section 3.4), we do not have the generation of a large pressure wave at ignition. Much smaller pressure waves are generated at each pulse (less than 0.01% of the gas pressure in amplitude) caused by the plasma chemistry provoking a fast change in gas density (possibly as a result of heat release by rapid pyrolysis of the fuel during the application, as the direct heat release by plasma is not accounted for in this simulation). The amplitude of these pressure waves depends on both the plasma kernel size and the pulse repetition frequency. At ignition, another pressure wave is generated, but it does not match the amplitude of the one seen in the ignition by the hot kernel (which was around 3% of the gas pressure in amplitude).

The time and length scales of energy deposition are thought to play an important role in the generation of pressure waves. Shorter, more spatially concentrated energy deposition will lead to the generation of a larger pressure wave at ignition. In the case of the ignition by a hot kernel (see section 3.4), the conditions can be interpreted as if energy is deposited instantly as a thermal input at $t = 0$, which leads to a large pressure wave at ignition. In the large plasma kernel configuration, conditions can be

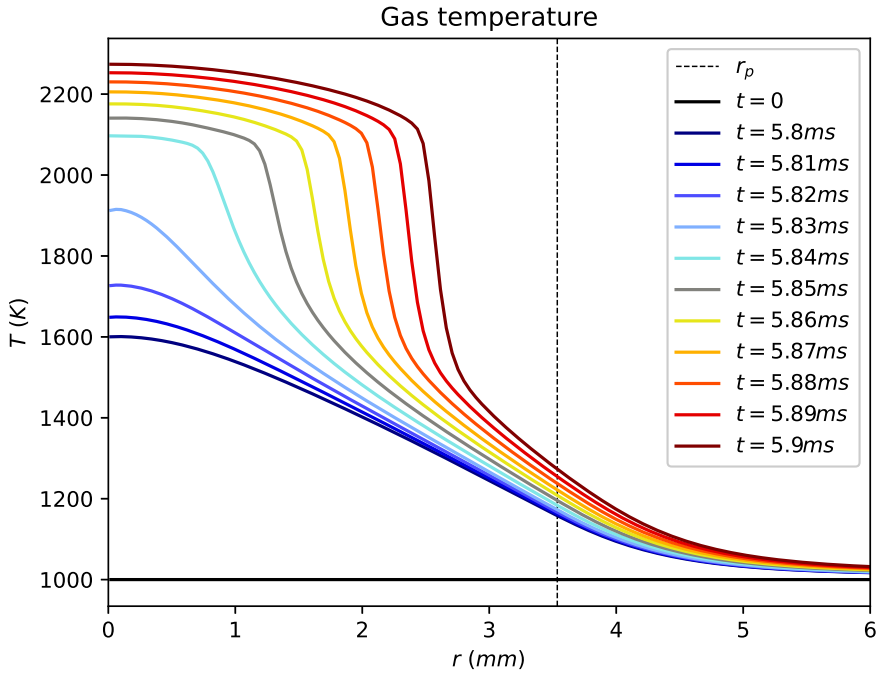


(a) Gas temperature

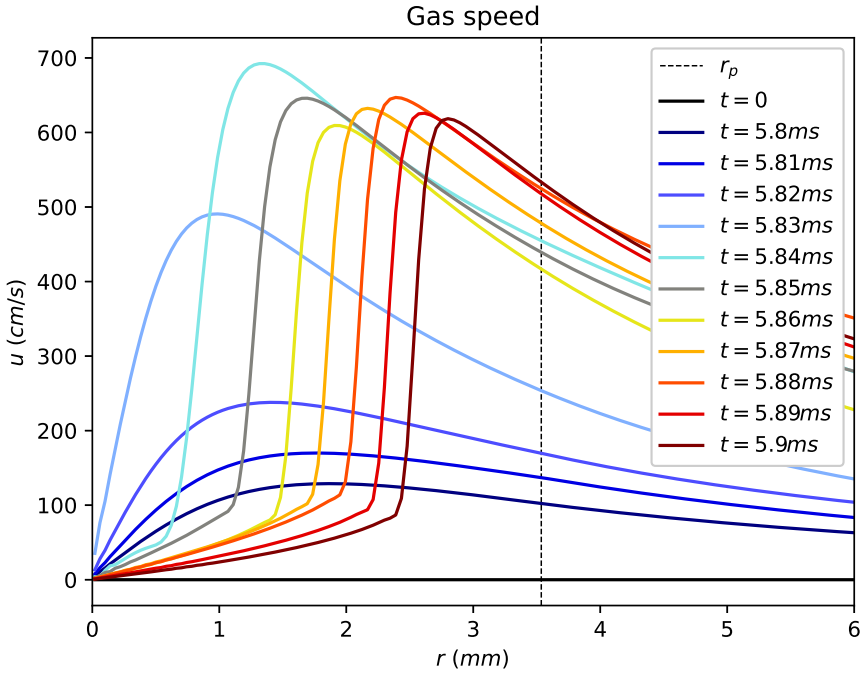


(b) Gas radial velocity

Figure 3-12: 1D ignition by a large plasma kernel actuated at low frequency: pressure and velocity.

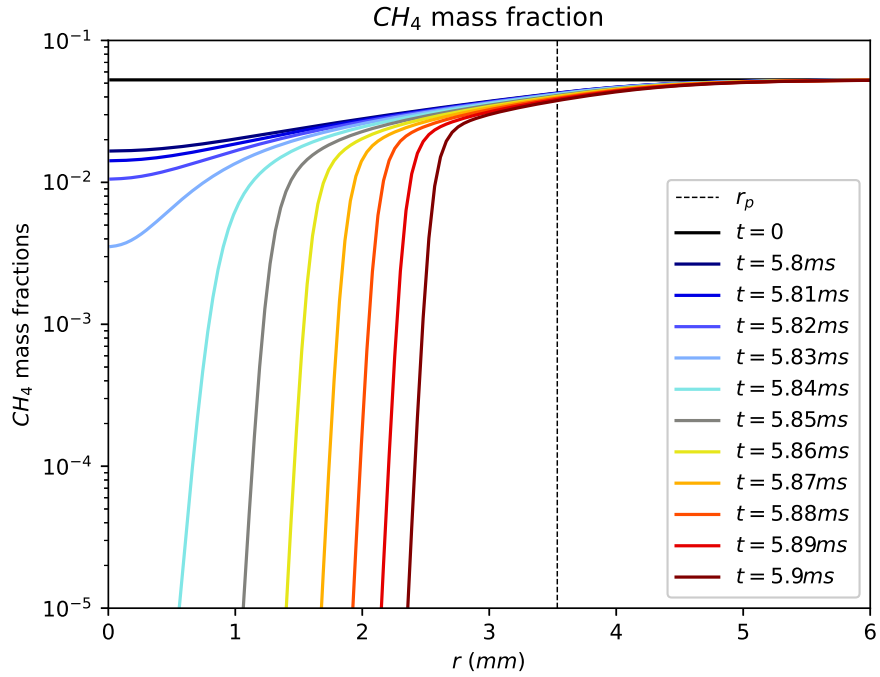


(a) Methane mass fraction

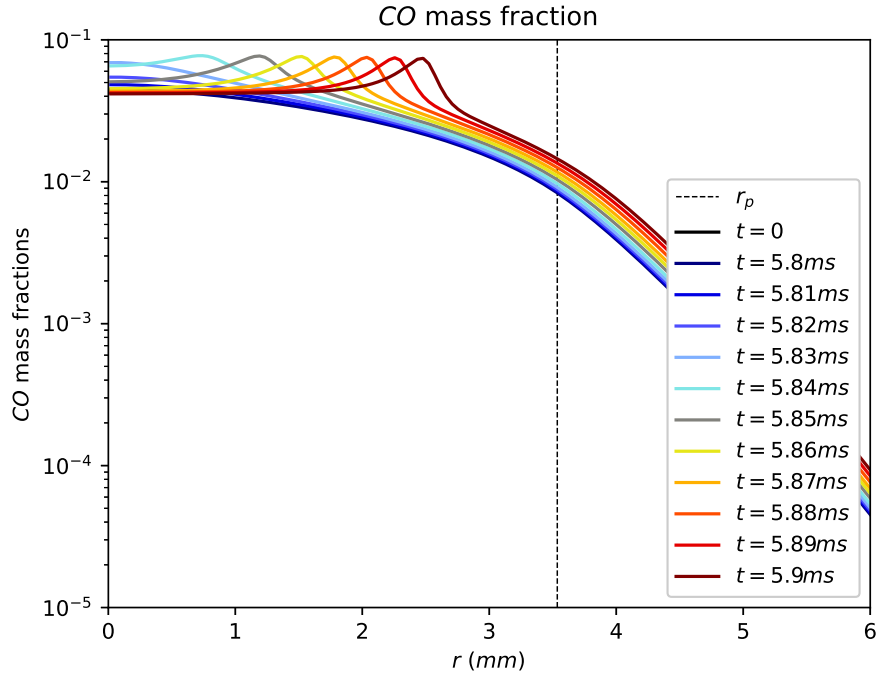


(b) Carbon monoxide mass fraction

Figure 3-13: 1D ignition by large plasma kernel actuated at low frequency: methane and carbon monoxide mass fractions.

interpreted as if the energy is inputted on a much longer timescale (a little at each pulse), on a larger lengthscale as well (with its 3.54 $mm$ in radius, the plasma kernel is larger than the hot kernel region which was 1 $mm$ in radius). This naturally leads to a much smaller pressure wave at ignition.

The gas temperature and methane mass fraction plots shown in figures 3-12-a and 3-13-a can help us locate the flame front and have an appreciation of the ignition kernel. It is clear from the results that the ignition kernel is significantly smaller than the plasma kernel. If it remains difficult to give an exact value of the ignition kernel size, we can safely say that it remains below 1.5 $mm$, i.e. less than half the plasma kernel size. If the plasma had been applied uniformly ($r_p = \infty$), then ignition would have happened everywhere simultaneously (uniform conditions, similar to zero-dimensional computations). Therefore, this difference between ignition kernel size and plasma kernel size can only be caused by one-dimensional effects, and is not driven by chemistry. Several 1D effects could participate in the apparition of a localized ignition kernel close to the centerline, including:

- the diffusion of species close to the edge of the plasma kernel. The diffusion effects are greater where the concentration gradients are the sharpest, i.e. at the border between the plasma-actuated region and the rest of the domain. Species generated by the plasma will be particularly affected, such as radicals, which play an important role in the speeding of ignition. In that region, consumed methane and oxygen are also replenished as gas out of the plasma kernel is diffusing in, further worsening the effect. Figure 3-13 confirms the importance of that effect, as gradients in methane and carbon monoxide concentration can be observed within the plasma kernel before ignition happens.

- the thermal diffusion on the edge of the plasma kernel. Similarly to species diffusion, part of the energy deposited by the plasma that eventually converts to the thermal energy of the gas is lost through diffusion. Figure 3-12-a shows that at ignition, the gas just outside of the plasma kernel has been heated up 200 $K$ (partly by combustion initiation, but mostly by heat conduction as

methane is not significantly consumed in this region), revealing that thermal diffusion also plays an important role in the forming of the ignition kernel.

- the pressure waves generated by the discharges. Although small in amplitude, these small perturbations in pressure also lead to an increase in the radial velocity of the gas particles as the wave propagates out. Regions closer to the centerline are less affected: in particular, the centerline ($r = 0$) remains with no radial velocity. Regions on the edge of the plasma kernel are the most affected and are subjected to a natural outflow of plasma-generated species such as radicals through this effect. However, we should note that pressure waves have probably a much less effect than species or thermal diffusion. In addition, part of the energy that would otherwise appear as a temperature increase or species dissociation is now expended in work (1D effect).

### 3.5.3 Small Plasma Kernel Actuated at High Frequency

The second simulation presented here involves a smaller plasma kernel size of $r_p = 0.79\ mm$ and higher frequency $f = 200\ kHz$. Predictions of gas temperature, gas speed, methane mass fraction, and carbon monoxide mass fraction are given in figures 3-14-a, 3-14-b, 3-15-c, and 3-15-d respectively. There again, the vertical dashed black line delimits the plasma kernel region.

First of all, we can note that the ignition delay time is not only much smaller than the auto-ignition case (see figure 3-8-a), but also significantly smaller than the case with a larger plasma kernel size and lower pulse repetition frequency. Indeed, if a large plasma kernel size and low pulse repetition frequency had given an ignition delay time close to 5.8 $ms$, this new test case gives an ignition delay closer to 220 $\mu s$. This difference is especially surprising as the power is kept similar between both simulations, therefore, until ignition, the large plasma kernel actually receives more energy from the plasma. A possible explanation for this effect is that higher pulse repetition frequency leads to higher energy deposited per pulse, as electrons have less

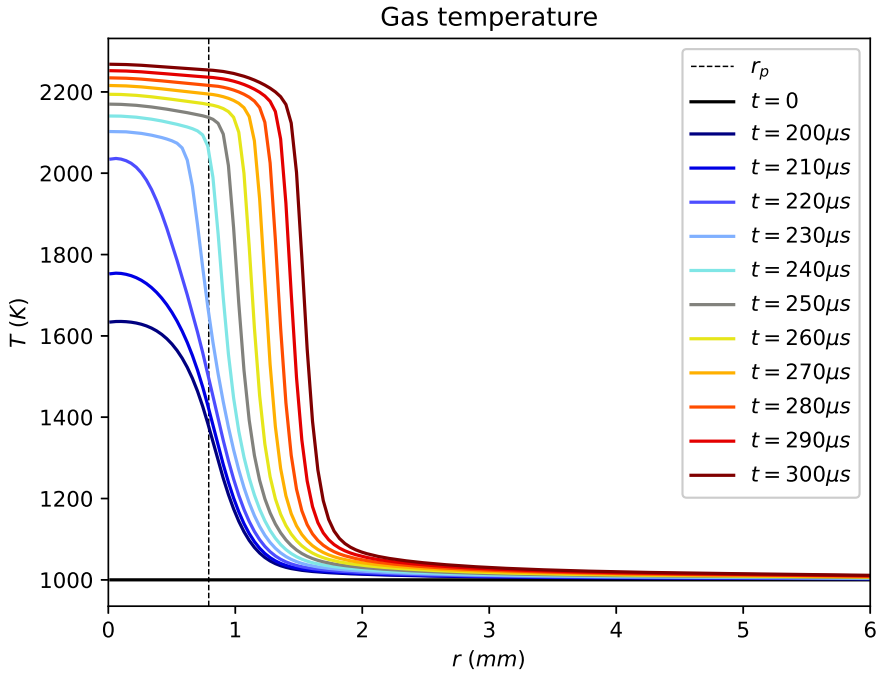


(a) Gas temperature

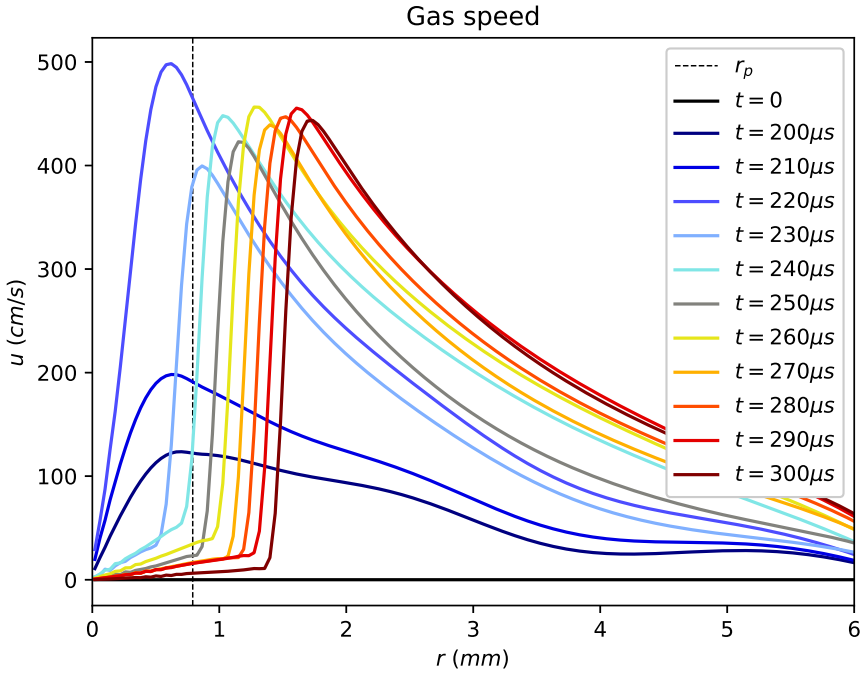


(b) Gas radial velocity

Figure 3-14: 1D ignition by a large plasma kernel actuated at low frequency: pressure and velocity.

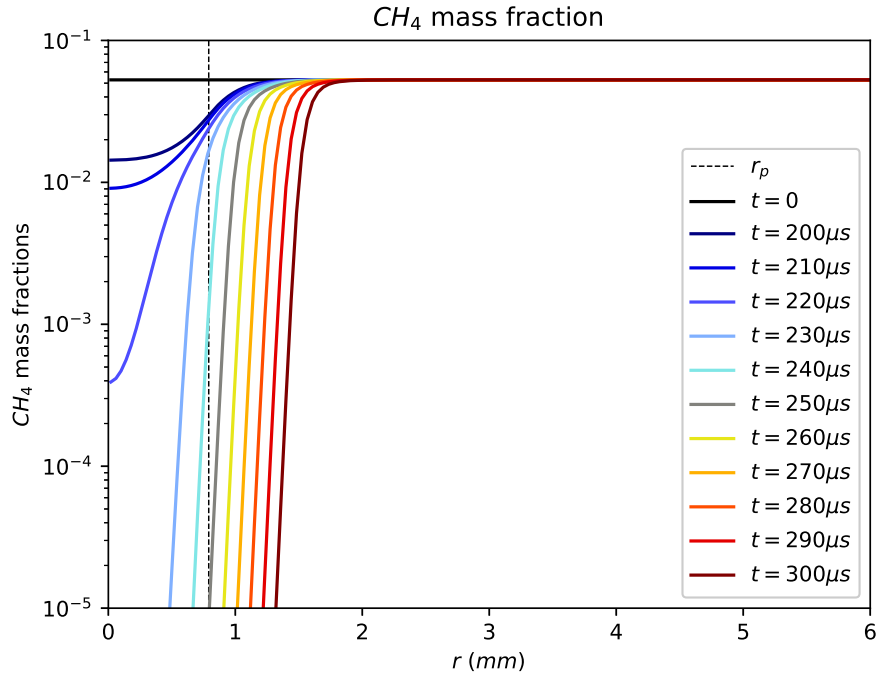


(a) Methane mass fraction

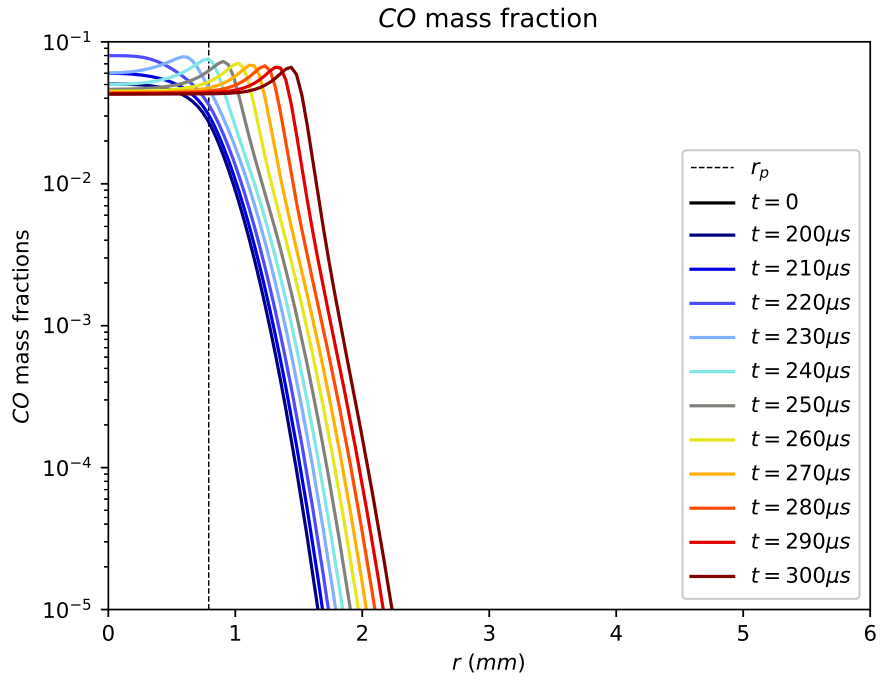


(b) Carbon monoxide mass fraction

Figure 3-15: 1D ignition by large plasma kernel actuated at low frequency: methane and carbon monoxide mass fractions.

time to recombine between pulses (see section 3.6.1 and figure 3-16).

The ignition kernel is, in this new test case, of a size similar to the plasma kernel size. This configuration is very different from what was observed in the case of the large plasma kernel configuration, where the ignition kernel was less than half its size. The gas temperature profile (see figure 3-14-a) suggests the ignition kernel radius $r_i$ is still smaller than the radius of the plasma kernel $r_p$, but this time the ratio $r_i/r_p > 0.6$. We suggested earlier that the difference between $r_i$ and $r_p$ is mainly driven by diffusion and pressure waves. In our case, pressure waves generated by the plasma are subjected to (i) a decrease in amplitude because the volume actuated is smaller, and (ii) an increase in amplitude because the energy deposited per pulse is larger. Overall, the pressure waves are unlikely causing alone this drastic change in the dynamics of ignition kernel formation.

The dynamics of species diffusion are also affected by the size of the plasma kernel. Using Fick's law of species diffusion to get the rough dependence of the diffusion flux to the size of the plasma kernel $r_p$ and the ignition delay time $\Delta t_{IDT}$, we have:

$$\frac{m_{diff}}{2\pi r_p h} \sim j_k \Delta t_{IDT} \sim D_k \frac{\partial X_k}{\partial r} \Delta t_{IDT} \sim D_k \Delta X_k \frac{\Delta t_{IDT}}{r_p} \tag{3.3}$$

Where $m_{diff}$ is the approximate mass lost from the plasma kernel to diffusion for a given species (oxygen radicals for instance). If we assume that the mole fraction difference between the centerline and the outer domain at ignition $\Delta X_k$ does not depend on the test case, then the amount of mass lost to diffusion can be directly expressed as:

$$\frac{m_{diff}}{2\pi r_p h} \propto \frac{\Delta t_{IDT}}{r_p} \tag{3.4}$$

Comparing the values of ignition delay time and plasma kernel size between the two simulations presented, we can conclude that diffusion fluxes are roughly 5 times more important for the large plasma kernel and low frequency configuration. In addition, the interface area between the plasma-actuated region and the rest of the domain is

also larger ($2\pi r_p h$) which further increases the loss of species caused by diffusion.

In conclusion, the small plasma kernel actuated at a high frequency leads to smaller losses caused by species diffusion. The ratio of the ignition kernel to the plasma-actuated kernel greatly $r_i/r_p$ increases, suggesting plasma kernel size can be optimized for efficiency, as it is discussed in section 3.6.2.

## 3.6 Influence of Plasma Kernel Size and Pulse Frequency

### 3.6.1 Constant Power Budget

We conducted several simulations with different values of the plasma kernel size $r_p$ and the pulse repetition frequency $f$ so as to keep the electrical power similar between simulations. Indeed, the total energy deposited by the plasma per unit length until ignition $\mathcal{E}_{tot}$ can be expressed as:

$$\mathcal{E}_{tot} = \pi r_p^2 f \Delta t_{IDT} \bar{\mathcal{E}}_{pulse} = \bar{\mathcal{P}} \Delta t_{IDT} \tag{3.5}$$

Where $\Delta t_{IDT}$ is the ignition delay time, $\bar{\mathcal{E}}_{pulse}$ the averaged volumetric energy deposited per pulse, and $\bar{\mathcal{P}}$ the averaged power deposited. We varied the plasma kernel size $r_p$ and the pulse repetition frequency $f$ so that the product $r_p^2 f$ is kept constant equal to 125 $m^2 \cdot s^{-1}$ between simulations, so the deposited power $\mathcal{P}$ depends only on the energy deposited per pulse $\mathcal{E}_{pulse}$ (approximated as constant). The test cases are summarized in table 3.1.

The volumetric energy deposited during a single pulse can be approximated using equation 2.8, which in our case can be further simplified:

$$\mathcal{E}_{pulse} \sim e \bar{n}_e N (\mu_e N) \left( \frac{\bar{E}}{N} \right)^2 \Delta t_{pulse} \propto \bar{n}_e N \tag{3.6}$$

Both the reduced electric field $E/N$ and the pulse width $\Delta t_{pulse}$ are determined by the

| Plasma kernel size $r_p$ $(mm)$ | Pulse repetition frequency $f$ $(kHz)$ |
|---|---|
| 0.79 | 200 |
| 1.00 | 125 |
| 1.25 | 80 |
| 1.58 | 50 |
| 2.24 | 25 |
| 3.54 | 10 |

Table 3.1: Plasma kernel and frequency test cases for ignition by NRP discharges.

pulse shape which is kept constant for all pulses and simulations. The product $(\mu_e N)$ only depends on $E/N$ too, therefore the energy deposited per pulse is mainly driven by the electron density $n_e$ as we observe only slight variations of the total density $N$ due to the plasma. The average energy deposited per pulse as approximated by equation 3.6 for the test case of table 3.1 is given on figure 3-16.

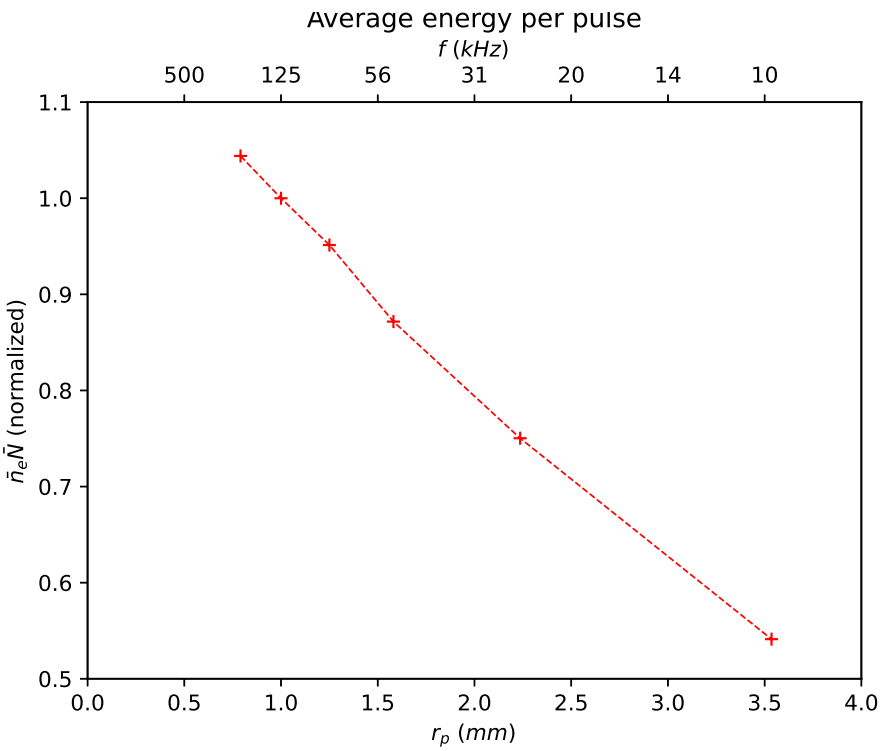


Figure 3-16: Averaged energy deposited per pulse as a function of plasma kernel size and pulse repetition frequency.

The averaged volumetric energy deposited per pulse $\bar{\mathcal{E}}_{pulse}$ evolution as we modify the plasma kernel size $r_p$ and the pulse repetition frequency $f$ is shown on figure 3-16. The energy deposited has been computed using the approximation from equation 3.6, and has been normalized as exact energy deposition values are not meaningful since we neglect gas heating effects. The goal is to compare simulations with each other. We can see in figure 3-16 that the energy per pulse changes slightly between simulations. The energy is larger at higher pulse repetition frequencies as free electrons have less time to recombine between pulses so the averaged electron density $\bar{n}_e$ remains high.

### 3.6.2 Ignition and Propagation Enhancement

The electric energy is deposited in the entire region of the plasma kernel, where $r < r_p$. If for a very small plasma kernel, the ignition kernel might grow larger than the plasma kernel, we observed that, for the cases studied, it remains contained within the plasma actuated zone: $r_i < r_p$. We can therefore define the part of the energy deposited in the ignition kernel, $\mathcal{E}_{ign}$, as a function of the total energy deposited by the plasma until ignition $\mathcal{E}_{tot}$ (see equation 3.5):

$$\mathcal{E}_{ign} = \left(\frac{r_i}{r_p}\right)^2 \mathcal{E}_{tot} \tag{3.7}$$

The fraction of the energy deposited into the ignition kernel, $\mathcal{E}_{ign}/\mathcal{E}_{tot}$, is partly used to speed up the ignition phase. The remaining energy fraction, $1 - \mathcal{E}_{ign}/\mathcal{E}_{tot}$, which is deposited outside of the ignition kernel, participates in the enhancement of the propagation phase by pre-cracking the fuel. This will lead to a larger flame speed in that region. This can also be an interesting contribution of the plasma, as it will accelerate the rate of fuel consumption in the whole volume to be ignited. The two proportions are plotted in figure 3-17 for different configurations of plasma kernel sizes and corresponding pulse repetition frequencies.

Analyzing the results shown in figure 3-17, we can note that a larger and larger proportion of the energy deposited goes into the enhancement of the propagation

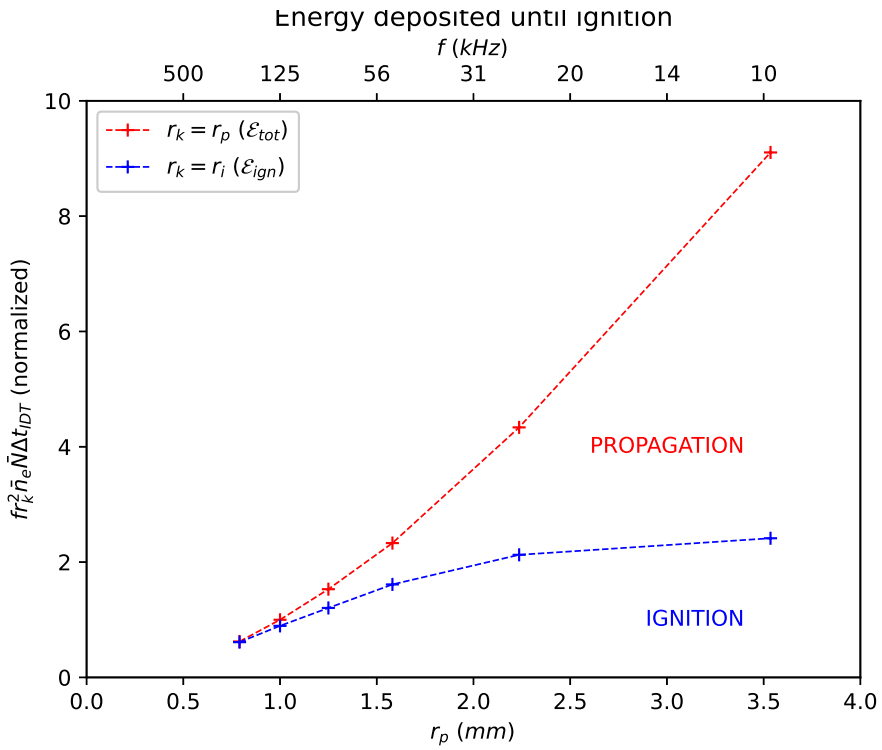


Figure 3-17: Total energy deposited as a function of plasma kernel size and pulse repetition frequency.

phase as the size of the plasma kernel is increased and the pulse repetition frequency is decreased. For a plasma kernel radius of $r_p = 3.5\ mm$ and a pulse repetition frequency $f = 10\ kHz$, almost 3/4 of the energy deposited does not benefit the ignition phase. However, it will benefit the overall rate of fuel consumption by possibly increasing the flame speed. As discussed earlier, larger plasma kernel sizes and lower pulse repetition frequencies lead to larger species diffusion effects which tend to spread the radicals over the domain. Those larger diffusion effects are in part worsened by the fact that the energy deposited per pulse is also affected by the pulse repetition frequency (see figure 3-16). This behavior is detrimental to ignition, but greatly enhances the flame propagation phase. On the contrary, for a plasma kernel radius of $r_p = 0.8\ mm$ and a pulse repetition frequency $f = 200\ kHz$, all of the energy deposited by the plasma goes into the ignition kernel. This study suggests that smaller plasma kernels actuated at higher frequencies are beneficial for speeding up the ignition phase, but not so much to enhance the propagation phase where large plasma kernels are preferred. The two

effects can be beneficial for overall speed up of the combustion process.

## 3.7 Chapter Summary

This chapter gathers zero-dimensional and one-dimensional simulation results for plasma-assisted ignition. Higher gas temperature is found to reduce the benefits of plasma assistance. Gas composition is shown to have a strong influence on how the plasma energy is deposited and how efficiently this energy helps the ignition phase. One-dimensional results of radial ignition demonstrate that diffusion effects determine the size of the ignition kernel. Modifying the size of the plasma-actuated kernel and the pulse frequency, a trade-off can be found to optimize ignition or propagation.

# Chapter 4

# Conclusions

## 4.1 Summary of Contributions

This work focused on numerical modeling of ignition of fuel/air mixtures at 1 $atm$ and high temperature (1000 $K$) by nanosecond repetitively pulsed discharges. In chapter 1, we summarized prior experimental and numerical efforts in the literature that quantified the benefits of plasma assistance and provided the fundamental understanding of the effects of NRP discharges on combustion, especially on *inflammation* (i.e. on the generation of the ignition kernel and development of a flame front). Previous works have revealed the clear benefits of NRP discharges in reducing ignition delay time, decreasing the minimum ignition energy, or extending lean limits. We acknowledge the numerous modeling efforts by the community, especially on zero-dimensional models and PAC chemical kinetics.

However, earlier models of plasma-assisted ignition often focus on specific conditions, and do not use parametric sweeping in order to de-couple the multiple variables at play (conditions, discharge geometry, actuation frequency, etc). The models developed in this work, detailed in chapter 2, are designed to allow for the exploration of a wide range of initial conditions and actuation strategies. First, a zero-dimensional model coupling plasma and combustion chemical solvers is assembled. This model is shown to give predictions in good agreement with test cases from the literature.

Then, this model is incorporated into a one-dimensional radial model, where 1D inviscid fluid equations (Euler equations) are included in cylindrical coordinates. In addition, combustion and plasma chemical mechanisms are selected to depict real-life combustion engine applications. To that end, we selected a "surrogate fuel" and validated the kinetics against test cases from the literature. Results from both 0D and 1D models are presented and analyzed in chapter 3.

Different parametric sweeps are conducted using the zero-dimensional chemical code developed and the surrogate fuel kinetics. First, the influence of initial gas temperature and averaged pulse energy on ignition delay time is studied (see section 3.2). Overall, results suggest that, at a given pulse energy, NRP discharges are more beneficial at low temperatures. At a given gas temperature, results show that IDT reduction quickly reaches a plateau when the pulse energy increases. Secondly, the influence of gas composition (equivalence ratio and dilution factor) is studied through "ternary plots" (see section 3.3). Results show that plasma is more beneficial than an instantaneous pure thermal input for almost all the mixtures studied. However, large variations can be observed over the exploration domain, suggesting that the gas mixture can affect the benefits of plasma assistance.

The one-dimensional fluid-chemical model for radial ignition by NRP discharges is exercised on two types of simulations. First, we looked at thermal ignition (no plasma) from a high-temperature kernel around the centerline (see section 3.4). Time and space-dependent results show the generation of a large pressure wave at ignition which progressively dissipates before propagating out of the domain. We also observed the emergence of a flame front that slows down when it exits the high-temperature kernel but eventually stabilizes around the local laminar flame speed as it propagates radially out. Secondly, we studied cases where ignition was triggered by NRP discharges (see section 3.5). Various configurations are studied, where the plasma kernel size and pulse repetition frequency are jointly modified so as to keep a constant deposited power budget between simulation cases. Results show that large plasma

kernels actuated at lower frequencies are more subjected to diffusion effects, which degrades the benefits of plasma assistance on the ignition phase but improves the flame propagation phase (see section 3.6).

Finally, chapter 4 provides some possibilities for future work that would help gain confidence in and/or further explain the presented results. Recent updates to the model have included improvements regarding energy tracking and energy deposition pathways analysis. Future studies could focus on running simulations of ignition by NRP discharge in the case of a fixed energy budget (instead of a fixed power budget), in order to decouple plasma kernel size and frequency and better characterize the effects of the plasma on ignition and propagation. Experimental validation of the 1D code could also be highly beneficial as it would build confidence in the model predictions, and possibly shed light on needed adjustments. A proposed experimental setup is introduced that allows for relevant measurements that can be compared to the model predictions.

## 4.2 Recommendations for Future Work

### 4.2.1 Energy Deposition Pathways

The most important aspect of the work presented here requiring improvements is energy tracking. Simulation results presented in this work do not accurately track the energy deposited by the plasma, i.e. gas heating from elastic collisions and quenching of excited states. To be more precise, the gas heating equation from the ZDPlasKin solver (equation 2.3) has not been taken into account in the results presented. Recent updates in the model have already solved this issue. The updated model is now able to accurately track energy deposition by the plasma, as well as provide a breakdown of what processes the energy is deposited into (excited states, temperature rise, pressure waves, diffusion losses, etc). Further studies with the updated model are recommended to provide more details regarding the effects of each energy pathway on both the ignition and the flame propagation phases.

### 4.2.2 Decoupling between Plasma Size and Frequency

The results presented in chapter 3 regarding the one-dimensional radial ignition triggered by NRP discharges were conducted for various cases of plasma kernel radii $r_p$ and pulse repetition frequencies $f$ so that the product $fr_p^2$ remained constant between simulations (constant power budget). This allows a qualitative comparison of different simulation cases where the plasma geometry drastically changes. However, the induced coupling between the plasma kernel size and the actuation frequency also becomes an important shortcoming during the analysis because it prevents us from clearly differentiating between the effects of the plasma kernel size on the one hand from the influence of the pulse repetition frequency on the other hand. Future simulations could focus on keeping a constant energy budget instead, by for instance keeping the same frequency between simulations and adjusting the number of pulses depending on the plasma kernel size. The two sets of simulation results would allow us to have a better picture of spatial (discharge size) and time effects (actuation frequency) and formulate a more precise optimization strategy for ignition and propagation enhancement.

### 4.2.3 Experimental Validation

This work is focused on numerical efforts, from the building of the 0D and 1D models described in chapter 2 to the analysis of the results in chapter 3. However, experimental investigations would also benefit this work and provide more insights and confidence regarding the final conclusions. In order to be able to compare experimental results with model predictions, some modifications in the model might need to be included (for instance, a heat loss term). The experiment should be representative of the radial ignition configuration implemented in the model. In addition, the experiment should allow for direct visual access to the radial propagation of the flame front to be able to take measurements. Measurements could include: (i) flame speed (through high-speed imaging), (ii) pulse energy (using high-voltage and current probes), (iii) densities of some key species on the centerline (like $OH$ or $O$ using

spectroscopy), (iv) imaging of ignition kernel shape and formation. An example of a possible experimental setup is given in figure 4-1.

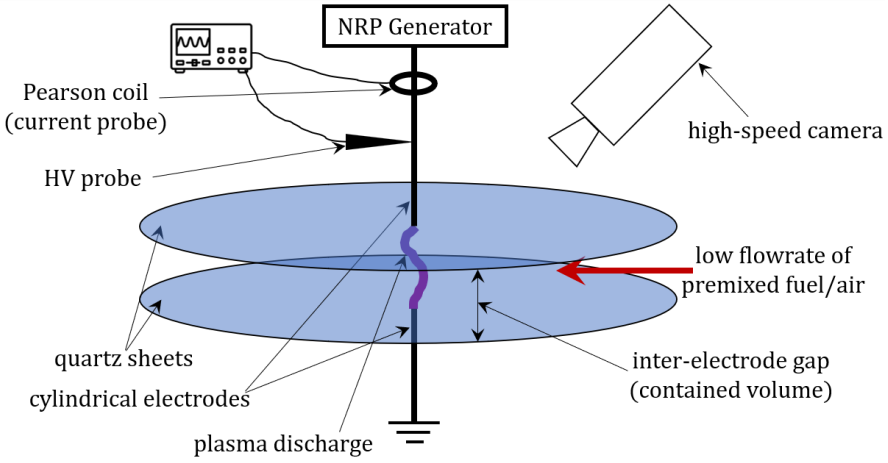


Figure 4-1: Proposed experiment design for validation of 1D radial model of ignition by NRP discharges.

# Appendix A

# Plasma Kinetics for Surrogate Fuel

| Main species | Related species |
|---|---|
| $Ar$ | $Ar^+$, $Ar^*$ |
| $N_2$ | $N_2^+$, $N_2(v)$, $N_2\,(A^3\Sigma_u^+)$, $N_2\,(B^3\Pi_g)$ , $N_2\,(B'^3\Sigma_u^-)$, $N_2\,(C^3\Pi_u)$, $N_2\,(W^3\Delta_u)$, $N_2\,(a^1\Pi_g)$, $N_2\,(a'^1\Sigma_u^-)$, $N_2\,(w^1\Delta_u)$, $N$ |
| $O_2$ | $O_2^+$, $O_2\left(b^1\Sigma_g^+\right)$, $O_2\,(a^1\Delta_g)$, $O_2^*$, $O$ |
| $H_2$ | $H$ |
| $CH_4$ | $CH_4^+$, $CH_3$, $CH_3^+$, $CH_2$, $CH_2^+$, $CH$, $C_2$, $C$ |
| $C_2H_4$ | $C_2H_4^+$, $C_2H_3$, $C_2H_3^+$, $C_2H_2$, $C_2H_2^+$, $C_2H$ |

Table A.1: Plasma kinetics for surrogate fuel: species included.

| Nb | Reaction | Cross-section | Source |
|---|---|---|---|
| E1 | $e + CH_4 \rightarrow e + CH_4$ (elastic) | [61] | |
| E2 | $e + N_2 \rightarrow e + N_2$ (elastic) | [29] | |
| E3 | $e + O_2 \rightarrow e + O_2$ (elastic) | [28] | |

Table A.2: Plasma kinetics for surrogate fuel: elastic electron-impact reactions.

| Nb | Reaction | Cross-section | Source |
|---|---|---|---|
| B1 | $e + O_2 \rightarrow e + 2O$ | [28] | [3] |
| B2 | $e + CH_4 \rightarrow e + CH_3 + H$ | [4] | [3] |
| B3 | $e + N_2 \rightarrow e + 2N$ | [29] | [3] |
| B18 | $e + C_2H_4 \rightarrow e + C_2H_3 + H$ | [31] | [32] |
| B19 | $e + C_2H_4 \rightarrow e + C_2H_2 + H_2$ | [31] | [32] |
| B20 | $e + C_2H_4 \rightarrow e + C_2H_2 + 2H$ | [31] | [32] |
| B21 | $e + C_2H_4 \rightarrow e + C_2H + H_2 + H$ | [31] | [32] |

Table A.3: Plasma kinetics for surrogate fuel: electron-impact dissociations.

| Nb | Reaction | Cross-section | Source |
|---|---|---|---|
| B4 | $e + O_2 \rightarrow e + O_2^*$ | [28] | [3] |
| B5 | $e + Ar \rightarrow e + Ar^*$ | [75] | [3] |
| B6 | $e + N_2 \rightarrow e + N_2(A^3\Sigma_u^+)$ | [58] | [3] |
| B7 | $e + N_2 \rightarrow e + N_2(B^3\Pi_g)$ | [58] | [3] |
| B8 | $e + N_2 \rightarrow e + N_2(B'^3\Sigma_u^-)$ | [58] | [3] |
| B9 | $e + N_2 \rightarrow e + N_2(W^3\Delta_u)$ | [58] | [3] |
| B10 | $e + N_2 \rightarrow e + N_2(a^1\Pi_g)$ | [58] | [3] |
| B11 | $e + N_2 \rightarrow e + N_2(a'^1\Sigma_u^-)$ | [58] | [3] |
| B12 | $e + N_2 \rightarrow e + N_2(w^1\Delta_u)$ | [58] | [3] |
| B13 | $e + N_2 \rightarrow e + N_2(C^3\Pi_u)$ | [58] | [3] |

Table A.4: Plasma kinetics for surrogate fuel: electron-impact excitations.

| Nb | Reaction | Cross-section | Source |
|---|---|---|---|
| B14 | $e + Ar \rightarrow 2e + Ar^+$ | | [32] |
| B15 | $e + O_2 \rightarrow 2e + O_2^+$ | [28] | [32] |
| B16 | $e + CH_4 \rightarrow 2e + CH_4^+$ | [61] | [32] |
| B17 | $e + N_2 \rightarrow 2e + N_2^+$ | [58] | [32] |
| B22 | $e + C_2H_4 \rightarrow 2e + C_2H_4^+$ | [31] | [32] |
| B23 | $e + C_2H_4 \rightarrow 2e + C_2H_3^+ + H$ | [31] | [32] |
| B24 | $e + C_2H_4 \rightarrow 2e + C_2H_2^+ + 2H$ | [31] | [32] |
| B25 | $e + C_2H_4 \rightarrow 2e + C_2H_2^+ + H_2$ | [31] | [32] |

Table A.5: Plasma kinetics for surrogate fuel: electron-impact ionizations.

| Nb | Reaction | Rate coefficient $(cm^3/s)$ | $\epsilon_r$ [20] $(eV)$ | Source |
|---|---|---|---|---|
| R8 | $N_2(A^3\Sigma_u^+) + O_2 \rightarrow N_2 + 2O$ | $1.7 \cdot 10^{-12}$ | | [3] |
| R9 | $N_2(A^3\Sigma_u^+) + O_2 \rightarrow N_2 + O_2(b^1\Sigma_g^+)$ | $7.5 \cdot 10^{-13}$ | | [3] |
| R10 | $2N_2(A^3\Sigma_u^+) \rightarrow N_2 + N_2(B^3\Pi_g)$ | $7.7 \cdot 10^{-11}$ | 5.02 | [3] |
| R11 | $2N_2(A^3\Sigma_u^+) \rightarrow N_2 + N_2(C^3\Pi_u)$ | $1.6 \cdot 10^{-10}$ | 1.28 | [3] |
| R12 | $N_2(A^3\Sigma_u^+) + N_2(v) \rightarrow N_2 + N_2(B^3\Pi_g)$ | $1.0 \cdot 10^{-10} e^{-\frac{1500}{T_g}}$ | 0.8 | [3] |
| R13 | $N_2(A^3\Sigma_u^+) + O \rightarrow N_2 + O$ | $3.0 \cdot 10^{-11}$ | 6.17 | [3] |
| R14 | $N_2(B^3\Pi_g) + O_2 \rightarrow N_2 + 2O$ | $3.0 \cdot 10^{-10}$ | | [3] |
| R15 | $N_2(B^3\Pi_g) + N_2 \rightarrow N_2(A^3\Sigma_u^+) + N_2$ | $1.0 \cdot 10^{-11}$ | 1.15 | [3] |
| R16 | $N_2(a'^1\Sigma_u^-) + O_2 \rightarrow N_2 + 2O$ | $2.8 \cdot 10^{-11}$ | | [3] |
| R17 | $N_2(a'^1\Sigma_u^-) + N_2 \rightarrow 2N_2$ | $2.0 \cdot 10^{-13}$ | 8.39 | [3] |
| R18 | $N_2(C^3\Pi_u) + O_2 \rightarrow N_2 + 2O$ | $3.0 \cdot 10^{-10}$ | | [3] |
| R19 | $N_2(C^3\Pi_u) + N_2 \rightarrow N_2(a'^1\Sigma_u^-) + N_2$ | $1.0 \cdot 10^{-11}$ | 2.67 | [3] |
| R20 | $N_2(C^3\Pi_u) \rightarrow N_2(B^3\Pi_g)$ | $3.0 \cdot 10^{-7}$ | 2.9 | [3] |
| R21 | $N_2(A^3\Sigma_u^+) + CH_4 \rightarrow N_2 + CH_4$ | $3.0 \cdot 10^{-15}$ | 6.17 | [3] |
| R22 | $N_2(B^3\Pi_g) + CH_4 \rightarrow N_2(A^3\Sigma_u^+) + CH_4$ | $2.85 \cdot 10^{-10}$ | 1.15 | [3] |
| R23 | $N_2(B^3\Pi_g) + CH_4 \rightarrow N_2 + CH_3 + H$ | $1.5 \cdot 10^{-11}$ | | [3] |
| R24 | $N_2(a'^1\Sigma_u^-) + CH_4 \rightarrow N_2 + CH_3 + H$ | $3.0 \cdot 10^{-10}$ | | [3] |
| R25 | $N_2(C^3\Pi_u) + CH_4 \rightarrow N_2 + CH_3 + H$ | $3.0 \cdot 10^{-10}$ | | [3] |

Table A.6: Plasma kinetics for surrogate fuel: quenching reactions for $N_2$.

| Nb | Reaction | Rate coefficient $(cm^3/s)$ | $\epsilon_r$ [20] $(eV)$ | Source |
|---|---|---|---|---|
| R26 | $O_2^* + CH_4 \rightarrow O_2 + CH_3 + H$ | $3.0 \cdot 10^{-15}$ | | [3] |
| R27 | $O_2^* + O_2 \rightarrow O_2(a^1\Delta_g) + O_2$ | $1.86 \cdot 10^{-13}$ | | [3] |
| R28 | $O_2^* + O_2 \rightarrow O_2(b^1\Sigma_g^+) + O_2$ | $8.1 \cdot 10^{-14}$ | | [3] |
| R29 | $O_2^* + O_2 \rightarrow 2O_2$ | $2.3 \cdot 10^{-14}$ | | [3] |
| R30 | $O_2^* + O \rightarrow O_2 + O$ | $5.0 \cdot 10^{-12}$ | | [3] |
| R31 | $O_2^* + O \rightarrow O_2(a^1\Delta_g) + O$ | $2.7 \cdot 10^{-12}$ | | [3] |
| R32 | $O_2^* + O \rightarrow O_2(b^1\Sigma_g^+) + O$ | $1.35 \cdot 10^{-12}$ | | [3] |

Table A.7: Plasma kinetics for surrogate fuel: quenching reactions for $O_2$.

| Nb | Reaction | Rate coefficient $(cm^3/s)$ | $\epsilon_r$ [20] $(eV)$ | Source |
|---|---|---|---|---|
| R1 | $Ar^* + O_2 \rightarrow Ar + 2O$ | $2.0 \cdot 10^{-10}$ | | [3] |
| R2 | $Ar^* + CH_4 \rightarrow Ar + CH_2 + 2H$ | $3.3 \cdot 10^{-10}$ | | [3] |
| R3 | $Ar^* + CH_4 \rightarrow Ar + CH + H_2 + H$ | $5.8 \cdot 10^{-11}$ | | [3] |
| R4 | $Ar^* + CH_4 \rightarrow Ar + CH_3 + H$ | $5.8 \cdot 10^{-11}$ | | [3] |
| R5 | $Ar^* + CH_4 \rightarrow Ar + CH_2 + H_2$ | $5.8 \cdot 10^{-11}$ | | [3] |
| R6 | $Ar^* + N_2 \rightarrow Ar + N_2(C^3\Pi_u)$ | $1.5 \cdot 10^{-11}$ | | [3] |
| R7 | $Ar^* + N_2 \rightarrow Ar + N_2(B^3\Pi_g)$ | $1.5 \cdot 10^{-11}$ | | [3] |
| R45 | $Ar^* + C_2H_4 \rightarrow Ar + C_2H_2 + 2H$ | $4.39 \cdot 10^{-10}$ | | [32] |
| R46 | $Ar^* + C_2H_4 \rightarrow Ar + C_2H_2 + H_2$ | $4.88 \cdot 10^{-11}$ | | [32] |
| R47 | $Ar^* + C_2H_4 \rightarrow Ar + 2CH_2$ | $4.88 \cdot 10^{-11}$ | | [32] |
| R48 | $Ar^* + C_2H_4 \rightarrow Ar + C_2H_3 + H$ | $4.88 \cdot 10^{-11}$ | | [32] |

Table A.8: Plasma kinetics for surrogate fuel: quenching reactions for $Ar$.

| Nb | Reaction | Rate coefficient $(cm^3/s)$ | $\epsilon_r$ [20] $(eV)$ | Source |
|---|---|---|---|---|
| R33 | $Ar^+ + N_2 \rightarrow Ar + N_2^+$ | $5.0 \cdot 10^{-11}$ | | [3] |
| R34 | $Ar^+ + CH_4 \rightarrow Ar + CH_3^+ + H$ | $1.1 \cdot 10^{-9}$ | | [3] |
| R35 | $Ar^+ + CH_4 \rightarrow Ar + CH_2^+ + H_2$ | $2.3 \cdot 10^{-10}$ | | [3] |
| R36 | $Ar^+ + O_2 \rightarrow Ar + O_2^+$ | $1.0 \cdot 10^{-10}$ | | [3] |
| R37 | $N_2^+ + CH_4 \rightarrow N_2 + CH_3^+ + H$ | $1.3 \cdot 10^{-9}$ | | [3] |
| R38 | $N_2^+ + O_2 \rightarrow N_2 + O_2^+$ | $1.04 \cdot 10^{-9} T_g^{-0.5}$ | | [3] |
| R39 | $CH_4^+ + O_2 \rightarrow CH_4 + O_2^+$ | $5.0 \cdot 10^{-10}$ | | [3] |
| R60 | $Ar^+ + C_2H_4 \rightarrow Ar + C_2H_4^+$ | $4.4 \cdot 10^{-11}$ | | [32]<[80] |
| R61 | $Ar^+ + C_2H_4 \rightarrow Ar + C_2H_3^+ + H$ | $8.36 \cdot 10^{-10}$ | | [32]<[80] |
| R62 | $Ar^+ + C_2H_4 \rightarrow Ar + C_2H_2^+ + 2H$ | $2.2 \cdot 10^{-10}$ | | [32]<[80] |

Table A.9: Plasma kinetics for surrogate fuel: charge-exchange reactions.

| Nb | Reaction | Rate coefficient $(cm^3/s)$ | $\epsilon_r$ $(eV)$ | Source |
|---|---|---|---|---|
| R40 | $e + O_2^+ \rightarrow 2O$ | $6.0 \cdot 10^{-5} T_g^{-1}$ | | [3] |
| R41 | $e + CH_4^+ \rightarrow CH_3 + H$ | $2.94 \cdot 10^{-6} T_g^{-0.5}$ | | [3] |
| R42 | $e + CH_4^+ \rightarrow CH_2 + 2H$ | $2.94 \cdot 10^{-6} T_g^{-0.5}$ | | [3] |
| R43 | $e + CH_3^+ \rightarrow CH_2 + H$ | $6.06 \cdot 10^{-6} T_g^{-0.5}$ | | [3] |
| R44 | $e + CH_2^+ \rightarrow CH + H$ | $4.33 \cdot 10^{-6} T_g^{-0.5}$ | | [3] |
| R49 | $e + C_2H_2^+ \rightarrow C_2H + H$ | $4.05 \cdot 10^{-5} T_g^{-0.5}$ | | [32]<[13] |
| R50 | $e + C_2H_2^+ \rightarrow C_2 + H_2$ | $1.62 \cdot 10^{-6} T_g^{-0.5}$ | | [32]<[13] |
| R51 | $e + C_2H_2^+ \rightarrow C_2 + 2H$ | $2.42 \cdot 10^{-5} T_g^{-0.5}$ | | [32]<[13] |
| R52 | $e + C_2H_2^+ \rightarrow CH_2 + C$ | $4.05 \cdot 10^{-5} T_g^{-0.5}$ | | [32]<[13] |
| R53 | $e + C_2H_2^+ \rightarrow 2CH$ | $1.05 \cdot 10^{-5} T_g^{-0.5}$ | | [32]<[13] |
| R54 | $e + C_2H_3^+ \rightarrow C_2H_2 + H$ | $3.91 \cdot 10^{-5} T_g^{-0.5}$ | | [32]<[13] |
| R55 | $e + C_2H_3^+ \rightarrow C_2H + H_2$ | $8.11 \cdot 10^{-6} T_g^{-0.5}$ | | [32]<[13] |
| R56 | $e + C_2H_3^+ \rightarrow C_2H + 2H$ | $7.97 \cdot 10^{-5} T_g^{-0.5}$ | | [32]<[13] |
| R57 | $e + C_2H_3^+ \rightarrow C_2 + H_2 + H$ | $4.05 \cdot 10^{-6} T_g^{-0.5}$ | | [32]<[13] |
| R58 | $e + C_2H_3^+ \rightarrow CH_3 + C$ | $8.11 \cdot 10^{-7} T_g^{-0.5}$ | | [32]<[13] |
| R59 | $e + C_2H_3^+ \rightarrow CH_2 + CH$ | $4.05 \cdot 10^{-6} T_g^{-0.5}$ | | [32]<[13] |
| R64 | $e + C_2H_4^+ \rightarrow C_2H_3 + H$ | $1.4 \cdot 10^{-6} T_e^{-0.5} \cdot (1 + 0.27 T_e^{0.55})^{-1}$ | | [31] |
| R65 | $e + C_2H_4^+ \rightarrow C_2H_2 + 2H$ | $5.8 \cdot 10^{-6} T_e^{-0.5} \cdot (1 + 0.27 T_e^{0.55})^{-1}$ | | [31] |
| R66 | $e + C_2H_4^+ \rightarrow C_2H_2 + H_2$ | $5.6 \cdot 10^{-7} T_e^{-0.5} \cdot (1 + 0.27 T_e^{0.55})^{-1}$ | | [31] |
| R67 | $e + C_2H_4^+ \rightarrow C_2H + H + H_2$ | $9.4 \cdot 10^{-7} T_e^{-0.5} \cdot (1 + 0.27 T_e^{0.55})^{-1}$ | | [31] |
| R68 | $e + C_2H_4^+ \rightarrow 2CH_2$ | $3.7 \cdot 10^{-7} T_e^{-0.5} \cdot (1 + 0.27 T_e^{0.55})^{-1}$ | | [31] |
| R69 | $e + C_2H_4^+ \rightarrow CH_3 + CH$ | $1.9 \cdot 10^{-7} T_e^{-0.5} \cdot (1 + 0.27 T_e^{0.55})^{-1}$ | | [31] |
| R70 | $2e + N_2^+ \rightarrow e + N_2$ | $1.0 \cdot 10^{-19} \cdot (300/T_e)^{4.5}$ | | [6] |
| R71 | $e + N_2 + N_2^+ \rightarrow 2N_2$ | $6.0 \cdot 10^{-27} \cdot (300/T_e)^{1.5}$ | | [6] |
| R72 | $e + O_2 + N_2^+ \rightarrow O_2 + N_2$ | $6.0 \cdot 10^{-27} \cdot (300/T_e)^{1.5}$ | | [6] |

Table A.10: Plasma kinetics for surrogate fuel: recombinations of ions.

# Bibliography


[1] Chemical-Kinetic Mechanisms for Combustion Applications. *University of California at San Diego. https://web.eng.ucsd.edu/mae/groups/combustion/mechanism.html.*

[2] Lawrence Livermore National Laboratory Combustion Mechanism. *https://combustion.llnl.gov/mechanisms.*

[3] N. L. Aleksandrov, S. V. Kindysheva, E. N. Kukaev, S. M. Starikovskaya, and A. Yu Starikovskii. Simulation of the ignition of a methane-air mixture by a high-voltage nanosecond discharge. *Plasma Physics Reports*, 35(10):867–882, 2009.

[4] L. L. Alves. The IST-LISBON database on LXCat. *Journal of Physics: Conference Series*, 565(1), 2014.

[5] N. B. Anikin, S. M. Starikovskaia, and A. Yu Starikovskii. Study of the oxidation of alkanes in their mixtures with oxygen and air under the action of a pulsed volume nanosecond discharge. *Plasma Physics Reports*, 30(12):1028–1042, 2004.

[6] Moon Soo Bak, Hyungrok Do, Mark Godfrey Mungal, and Mark A. Cappelli. Plasma-assisted stabilization of laminar premixed methane/air flames around the lean flammability limit. *Combustion and Flame*, 159(10):3128–3137, 2012.

[7] Moon Soo Bak, Seong kyun Im, M. Godfrey Mungal, and Mark A. Cappelli. Studies on the stability limit extension of premixed and jet diffusion flames of methane, ethane, and propane using nanosecond repetitive pulsed discharge plasmas. *Combustion and Flame*, 160(11):2396–2403, 2013.

[8] S. Barbosa, G. Pilla, D. A. Lacoste, P. Scouflaire, S. Ducruix, C. O. Laux, and D. Veynante. Influence of nanosecond repetitively pulsed discharges on the stability of a swirled propane/air burner representative of an aeronautical combustor. *Philosophical Transactions of the Royal Society A: Mathematical, Physical and Engineering Sciences*, 373(2048), 2015.

[9] Paul Bartholomew, Fabian Denner, Mohd Hazmil Abdol-azis, Andrew Marquis, and Berend G M Van Wachem. Unified formulation of the momentum-weighted interpolation for collocated variable arrangements. *Journal of Computational Physics*, 375:177–208, 2018.

[10] S. A. Bozhenkov, S. M. Starikovskaia, and A. Yu Starikovskii. Nanosecond gas discharge ignition of H2- and CH4- containing mixtures. *Combustion and Flame*, 133(1-2):133–146, 2003.

[11] Doug Breden and Laxminarayan Raja. Simulations of nanosecond pulse plasmas in supersonic flows for combustion applications. *AIAA Journal*, 50(3):647–658, 2012.

[12] Douglas Breden, Laxminarayan L. Raja, Cherian A. Idicheria, Paul M. Najt, and Shankar Mahadevan. A numerical study of high-pressure non-equilibrium streamers for combustion ignition application. *Journal of Applied Physics*, 114(8), 2013.

[13] J. Brian and A. Mitchell. The dissociative recombination of molecular ions. *Physics Reports*, 186(5):215–248, 1990.

[14] Michael P. Burke, Marcos Chaos, Yiguang Ju, Frederick L. Dryer, and Stephen J. Klippenstein. Comprehensive H 2/O 2 kinetic model for high-pressure combustion. *International Journal of Chemical Kinetics*, 44(7):444–474, 2012.

[15] D. C.C. Chen, J. Lawton, and F. J. Weinberg. Augmenting flames with electric discharges. *Symposium (International) on Combustion*, 10(1):743–754, 1965.

[16] Francesco Di Sabatino and Deanna A. Lacoste. Enhancement of the lean stability and blow-off limits of methane-air swirl flames at elevated pressures by nanosecond repetitively pulsed discharges. *Journal of Physics D: Applied Physics*, 53(35), 2020.

[17] Hyungrok Do, Mark A. Cappelli, and M. Godfrey Mungal. Plasma assisted cavity flame ignition in supersonic flows. *Combustion and Flame*, 157(9):1783–1794, 2010.

[18] Hyungrok Do, Seong Kyun Im, Mark A. Cappelli, and M. Godfrey Mungal. Plasma assisted flame ignition of supersonic flows over a flat wall. *Combustion and Flame*, 157(12):2298–2305, 2010.

[19] Ashim Dutta, Zhiyao Yin, and Igor V. Adamovich. Cavity ignition and flameholding of ethylene-air and hydrogen-air flows by a repetitively pulsed nanosecond discharge. *Combustion and Flame*, 158(8):1564–1576, 2011.

[20] Forrest R. Gilmore. Potential energy curves for N2, NO, O2 and corresponding ions. *Journal of Quantitative Spectroscopy and Radiative Transfer*, 5(2):369–389, 1965.

[21] Irvin Glassman and Richard A. Yetter. *Combustion*. 2009.

[22] David G. Goodwin, Harry K. Moffat, Ingmar Schoegl, Raymond L. Speth, and Bryan W. Weber. Cantera: An object-oriented software toolkit for chemical kinetics, thermodynamics, and transport processes (version 2.6.0). *https://www.cantera.org*, 2022.

[23] David G. Goodwin, Harry K. Moffat, Ingmar Schoegl, Raymond L. Speth, and Bryan W. Weber. Cantera: An object-oriented software toolkit for chemical kinetics, thermodynamics, and transport processes. Version 2.6.0. *https://www.cantera.org*, 2022.

[24] G. J.M. Hagelaar and L. C. Pitchford. Solving the Boltzmann equation to obtain electron transport coefficients and rate coefficients for fluid models. *Plasma Sources Science and Technology*, 14(4):722–733, 2005.

[25] A. J. Harrison and F. J. Weinberg. Flame stabilization by plasma jets. *Proceedings of the Royal Society of London. Series A, Mathematical and Physical Sciences*, 321(1544):95–103, 1971.

[26] C.E. Haselfoot and P.J. Kirkby. XLV. The electrical effects produced by the explosion of hydrogen and oxygen . *The London, Edinburgh, and Dublin Philosophical Magazine and Journal of Science*, 8(46):471–481, 1904.

[27] John C. Hilliard and George S. Springer. *Fuel economy in road vehicles powered by spark ignition engines*. First edition, 1984.

[28] A. A. Ionin, I. V. Kochetov, A. P. Napartovich, and N. N. Yuryshev. Physics and engineering of singlet delta oxygen production in low-temperature plasma. *Journal of Physics D: Applied Physics*, 40(2), 2007.

[29] Yukikazu Itikawa. Cross sections for electron collisions with nitrogen molecules. *Journal of Physical and Chemical Reference Data*, 35(1):31–53, 2006.

[30] Lawton J., K. G. Payne, and F. J. Weinberg. Flame-arc combination. *Nature*, 193:736–738, 1962.

[31] R. K. Janev and D. Reiter. Collision processes of C2,3Hy and C2,3Hy+ hydrocarbons with electrons and protons. *Physics of Plasmas*, 11(2):780–829, 2 2004.

[32] Joseph K. Lefkowitz. *Plasma Assisted Combustion: Fundamental Studies and Engine Applications*. PhD thesis, 2016.

[33] Yiguang Ju and Wenting Sun. Plasma assisted combustion: Dynamics and chemistry. *Progress in Energy and Combustion Science*, 48:21–83, 2015.

[34] Robert J Kee and Michael E Coltrin. *Chemically Reactiong Flow: Theory, Modeling and Simulation. Second Edition*. 2018.

[35] A. A. Konnov. Implementation of the NCN pathway of prompt-NO formation in the detailed reaction mechanism. *Combustion and Flame*, 156(11):2093–2105, 2009.

[36] I. N. Kosarev, N. L. Aleksandrov, S. V. Kindysheva, S. M. Starikovskaia, and A. Yu Starikovskii. Kinetics of ignition of saturated hydrocarbons by nonequilibrium plasma: CH4-containing mixtures. *Combustion and Flame*, 154(3):569–586, 2008.

[37] I. N. Kosarev, N. L. Aleksandrov, S. V. Kindysheva, S. M. Starikovskaia, and A. Yu Starikovskii. Kinetics of ignition of saturated hydrocarbons by nonequilibrium plasma: C2H6- to C5H12-containing mixtures. *Combustion and Flame*, 156(1):221–233, 2009.

[38] I. A. Kossyi, A. Yu Kostinsky, A. A. Matveyev, and V. P. Silakov. Kinetic scheme of the non-equilibrium discharge in nitrogen-oxygen mixtures. *Plasma Sources Science and Technology*, 1(3):207–220, 1992.

[39] Deanna A. Lacoste. Flames with plasmas. *Proceedings of the Combustion Institute*, 000:1–24, 2022.

[40] Joseph Lefkowitz, Yiguang Ju, Christopher Stevens, John Hoke, Timothy Ombrello, and Frederick Schauer. The effects of repetitively pulsed nanosecond discharges on ignition time in a pulsed detonation engine. *49th AIAA/ASME/SAE/ASEE Joint Propulsion Conference*, 1 PartF:1–19, 2013.

[41] Bernard Lewis and Guenther von Elbe. *Combustion, flames, and explosions of gases*. Harcourt Brace Jovanovich, third edition, 1987.

[42] Ting Li, Igor V. Adamovich, and Jeffrey A. Sutton. A burner platform for examining the effects of non-equilibrium plasmas on oxidation and combustion chemistry. *Combustion Science and Technology*, 185(6):990–998, 2013.

[43] Sara Lovascio, Jun Hayashi, Sergey Stepanyan, Gabi D. Stancu, and Christophe O. Laux. Cumulative effect of successive nanosecond repetitively pulsed discharges on the ignition of lean mixtures. *Proceedings of the Combustion Institute*, 37(4):5553–5560, 2019.

[44] J. Lovett, T. Brogan, D. Philippona, B. Kiel, and T. Thompson. Development Needs for Advanced Afterburner Designs. (July):1–12, 2004.

[45] Alejandro Luque. BOLtzmann equation solver Open-Source library, 2014.

[46] J. Maillard, T. van den Biggelaar, E. Pannier, and C. O. Laux. Time-resolved Optical Emission Spectroscopy measurements of electron density and temperature in CO2 Nanosecond Repetitively Pulsed discharges. *AIAA Science and Technology Forum and Exposition, AIAA SciTech Forum 2022*, (February), 2022.

[47] W. L. Morgan. *Electron Collision Data for Plasma Chemistry Modeling*, volume 43. Elsevier Masson SAS, 2000.

[48] Kgakgamatso Mphale and Mal Heron. Microwave measurement of electron density and collision frequency of a pine fire. *Journal of Physics D: Applied Physics*, 40(9):2818–2825, 2007.

[49] T. Ombrello, Sang Hee Won, Yiguang Ju, and S. Williams. Flame propagation enhancement by plasma excitation of oxygen. Part II: Effects of O2(a1$\Delta$g). *Combustion and Flame*, 157(10):1916–1928, 2010.

[50] S. Pancheshnyi, S. Biagi, M. C. Bordage, G. J.M. Hagelaar, W. L. Morgan, A. V. Phelps, and L. C. Pitchford. The LXCat project: Electron scattering cross sections and swarm parameters for low temperature plasma modeling. *Chemical Physics*, 398(1):148–153, 2012.

[51] S. Pancheshnyi, B. Eismann, G. J.M. Hagelaar, and L. C. Pitchford. Computer code ZDPlasKin. *http://www.zdplaskin.laplace.univ-tlse.fr*, 2008.

[52] Sergey V. Pancheshnyi, Deanna A. Lacoste, Anne Bourdon, and Christophe O. Laux. Ignition of propane-air mixtures by a repetitively pulsed nanosecond discharge. *IEEE Transactions on Plasma Science*, 34(6):2478–2487, 2006.

[53] Colin Pavan. *Nanosecond Pulsed Plasmas in Dynamic Combustion Environments*. PhD thesis, Massachusetts Institute of Technology, 2023.

[54] Colin A. Pavan and Carmen Guerra-Garcia. Modelling the Impact of a Repetitively Pulsed Nanosecond DBD Plasma on a Mesoscale Flame. *AIAA Science and Technology Forum and Exposition, AIAA SciTech Forum 2022*, pages 1–13, 2022.

[55] Gerald L Pellett, Sarah N Vaden, and Lloyd G Wilson. Gaseous Surrogate Hydrocarbons for a Hifire Scramjet That Mimic Opposed Jet Extinction Limits for Cracked Jp Fuels. *55 th JANNAF Propulsion Meeting*, (July):12–16, 2008.

[56] E. L. Petersen, D. F. Davidson, and R. K. Hanson. Kinetics modeling of shock-induced ignition in low-dilution CH4/O2 mixtures at high pressures and intermediate temperatures. *Combustion and Flame*, 117(1-2):272–290, 1999.

[57] Z. Lj Petrović, S. Dujko, D. Marić, G. Malović, Ž Nikitović, O. Šašić, J. Jovanović, V. Stojanović, and M. Radmilović-Radenović. Measurement and interpretation of swarm parameters and their application in plasma modelling. *Journal of Physics D: Applied Physics*, 42(19), 2009.

[58] A. V. Phelps and L. C. Pitchford. Anisotropic scattering of electrons by N2 and its effect on electron transport. *Physical Review A*, 31(5):2932–2949, 1985.

[59] Guillaume L. Pilla, Deanna A. Lacoste, Denis Veynante, and Christophe O. Laux. Stabilization of a swirled propane-air flame using a nanosecond repetitively pulsed plasma. *IEEE Transactions on Plasma Science*, 36(4 PART 1):940–941, 2008.

[60] Daniel I. Pineda, Benjamin Wolk, Tim Sennott, Jyh Yuan Chen, Robert W. Dibble, and Daniel Singleton. Nanosecond pulsed discharge ignition in a lean methane-air mixture. *Laser Ignition Conference, LIC 2015*, c(Lic):2–4, 2015.

[61] L.C. Pitchford, B.V. McKoy, A. Chutjian, and S. Trajmar. *Swarm Studies and Inelastic Electron-Molecule Collisions*. 1987.

[62] N. A. Popov. Fast gas heating in a nitrogen-oxygen discharge plasma: I. Kinetic mechanism. *Journal of Physics D: Applied Physics*, 44(28), 2011.

[63] E. Meeks J.A. Miller R.J. Kee, F.M. Rupley. CHEMKIN-III: A Fortran Chemical Kinetics Package for the Analysis of Gas-phase Chemical and Plasma Kinetics, 1996.

[64] C Robinson and D B Smith. The auto-ignition temperature of methane. *Journal of Hazardous Materials*, 8:199–203, 1984.

[65] Y. Sakai. Database in low temperature plasma modeling. *Applied Surface Science*, 192(1-4):327–338, 2002.

[66] Jeffrey Santner, Xueliang Yang, Qiang Wang, Yiguang Ju, and Xiaobo Shen. HP-mech: A high pressure kinetic mechanism for C2 flames with exhaust gas dilution. *53rd AIAA Aerospace Sciences Meeting*, (January):1–7, 2015.

[67] Ashish Sharma, Vivek Subramaniam, Evrim Solmaz, and Laxminarayan L. Raja. Fully coupled modeling of nanosecond pulsed plasma assisted combustion ignition. *Journal of Physics D: Applied Physics*, 52(9), 2019.

[68] Taisuke Shiraishi, Tomonori Urushihara, and Martin Gundersen. A trial of ignition innovation of gasoline engine by nanosecond pulsed low temperature plasma ignition. *Journal of Physics D: Applied Physics*, 42(13), 2009.

[69] John M. Simmie. Detailed chemical kinetic models for the combustion of hydrocarbon fuels. *Progress in Energy and Combustion Science*, 29(6):599–634, 2003.

[70] D. Singleton, S. J. Pendleton, and M. A. Gundersen. The role of non-thermal transient plasma for enhanced flame ignition in C2H4-air. *Journal of Physics D: Applied Physics*, 44(2), 2011.

[71] Gregory P Smith, David M Golden, Michael Frenklach, Nigel W Moriarty, Boris Eiteneer, Mikhail Goldenberg, C Thomas Bowman, Ronald K Hanson, Soonho Song, William C Jr. Gardiner, Vitali V Lissianski, and Zhiwei Qin. Gas Research Institute combustion mechanism - version 3.0. *http://www.me.berkeley.edu/gri_mech/*, 1999.

[72] S. M. Starikovskaia. Plasma assisted ignition and combustion. *Journal of Physics D: Applied Physics*, 39(16), 2006.

[73] S. M. Starikovskaia. Plasma-assisted ignition and combustion: Nanosecond discharges and development of kinetic mechanisms. *Journal of Physics D: Applied Physics*, 47(35), 2014.

[74] Andrey Starikovskiy and Nickolay Aleksandrov. Plasma-assisted ignition and combustion. *Progress in Energy and Combustion Science*, 39(1):61–110, 2013.

[75] K. Tachibana. Excitation of the 1s5, 1s4, 1s3, and 1s2 levels of argon by low-energy electrons. *Physical Review A*, 34(2):1007–1015, 1986.

[76] A. Tejero-Del-Caz, V. Guerra, D. Gonçalves, M. Lino Da Silva, L. Marques, N. Pinhão, C. D. Pintassilgo, and L. L. Alves. The LisbOn KInetics Boltzmann solver. *Plasma Sources Science and Technology*, 28(4), 2019.

[77] A. Tejero-Del-Caz, V. Guerra, N. Pinh o, C. D. Pintassilgo, and L. L. Alves. On the quasi-stationary approach to solve the electron Boltzmann equation in pulsed plasmas. *Plasma Sources Science and Technology*, 30(6), 2021.

[78] Fabien Tholin and Anne Bourdon. Influence of temperature on the glow regime of a discharge in air at atmospheric pressure between two point electrodes. *Journal of Physics D: Applied Physics*, 44(38), 2011.

[79] Albina A. Tropina, Mruthunjaya Uddi, and Yiguang Ju. On the effect of nonequilibrium plasma on the minimum ignition energy: Part 2. *IEEE Transactions on Plasma Science*, 39(12 PART 1):3283–3287, 2011.

[80] Masaharu Tsuji, Hiroyuki Kouno, Ken-ichi Matsamura, Tsuyoshi Funatsu, Yukio Nishimura, Hiroshi Obase, Hirofumi Kugishima, and Kouichi Yoshida. Dissociative charge-transfer reactions of Ar+ with simple aliphatic hydrocarbons at thermal energy. *The Journal of Chemical Physics*, 98(3):2011–2022, 1993.

[81] Mruthunjaya Uddi, Naibo Jiang, Evgeny Mintusov, Igor V. Adamovich, and Walter R. Lempert. Atomic oxygen measurements in air and air/fuel nanosecond pulse discharges by two photon laser induced fluorescence. *Proceedings of the Combustion Institute*, 32 I(1):929–936, 2009.

[82] Hai Wang, Xiaoqing You, Ameya V. Joshi, Scott G. Davis, Alexander Laskin, Fokion Egolfopoulos, and Chung K. Law. USC Mech Version II. High-Temperature Combustion Reaction Model of H2/CO/C1-C4 Compounds. *http://www.me.berkeley.edu/gri_mech/*, 2007.

[83] Yiqing Wang, Ashkan Movaghar, Ziyu Wang, Zefang Liu, Wenting Sun, Fokion N. Egolfopoulos, and Zheng Chen. Laminar flame speeds of methane/air mixtures at engine conditions: Performance of different kinetic models and power-law correlations. *Combustion and Flame*, 218:101–108, 2020.

[84] Chaoqi Xu and Alexander A. Konnov. Validation and analysis of detailed kinetic models for ethylene combustion. *Energy*, 43(1):19–29, 2012.

[85] Xueliang Yang, Xiaobo Shen, Jeffery Santer, Hao Zhao, and Yiguang Ju. High-pressure combustion mechanism. *http://engine.princeton.edu/mechanism/HP-Mech.html*, 2017.

[86] Zhiyao Yin, Aaron Montello, Campbell D. Carter, Walter R. Lempert, and Igor V. Adamovich. Measurements of temperature and hydroxyl radical generation/decay in lean fuel-air mixtures excited by a repetitively pulsed nanosecond discharge. *Combustion and Flame*, 160(9):1594–1608, 2013.

[87] Ying Zhou and Z. J. Wang. Absorbing boundary conditions for the Euler and Navier-Stokes equations with the spectral difference method. *Journal of Computational Physics*, 229(23):8733–8749, 2010.